Supercontinuum generation in photonic crystal fibres

Modelling and dispersion engineering for spectral shaping

Frosz, Michael Henoch

Publication date:
2007

Document Version
Publisher's PDF, also known as Version of record

Supercontinuum generation in photonic crystal fibres: Modelling and dispersion engineering for spectral shaping

Michael H. Frosz

August 31st 2006

COM•DTU
Department of Communications, Optics & Materials
Technical University of Denmark
Ørsteds Plads 345V
DK-2800 Kgs. Lyngby
Denmark

Contents

Preface

The present thesis describes the scientific research carried out as part of my Ph.D. project in the period September 1st 2003–August 31st 2006.

The work took place at COM•DTU (Department of Communications, Optics & Materials), Technical University of Denmark, and the Optics and Plasma Research Department (OPL), Risø National Laboratory. The project was financed by the Technical University of Denmark and supervised by

- Anders O. Bjarklev, Professor, dr.techn., COM•DTU, Technical University of Denmark, Kgs. Lyngby
- Jes Broeng, Head of Department, Ph.D., Crystal Fibre A/S, Birkerød
- Ole Bang, Associate Professor, Ph.D., COM•DTU, Technical University of Denmark, Kgs. Lyngby
- Peter E. Andersen, Senior Scientist, Ph.D., OPL, Risø National Laboratory, Roskilde

Acknowledgements

I would like to sincerely thank all of my supervisors for their support, help, suggestions, guidance, advice, and for making this project possible.

In alphabetical order (since the importance of a person's helping hand cannot be quantified) I would also like to thank: Andreas Tycho, now at Høiberg A/S, for helping Peter Falk and me coordinate our projects while Andreas was still at DTU; Finn Pedersen and Henning E. Larsen, OPL, for their invaluable technical work on the OCT system built in collaboration

between COM•DTU and OPL; Harold T. Yura, Aerospace Corporation, USA, for helpful comments on the thesis manuscript; Jesper Lægsgaard, COM•DTU, for being the guy everyone comes running to when they need help from a hardcore physicist; Kim P. Hansen, Crystal Fibre A/S, for valuable information and discussions; Kristian G. Hougaard, now at MEK, DTU, for his tireless help whenever I had a Linux-related question or problem (the problems were, of course, always due to the user, never Linux), both while and after he was at COM•DTU; Lars Thrane, OPL, for discussions about applications for OCT; Laura Pastor Sanz who came as a Masters student in 2003 from the Polytechnic University of Madrid, Spain, and built an excellent high-speed optical delay line for the OCT system; Martijn Beukema, Vrije Universiteit Brussel, Belgium, for his visit in 2006 and initiated collaboration; Martina Delgado-Pinar, University of Valencia, Spain, for her visit in 2005 and initiated collaboration on tapered fibres; Per D. Rasmussen, COM•DTU, for discussions on simulations and parallelization, and helpful comments on the thesis manuscript; Vilar Camara Neto for writing the `breakurl` package for LaTeX and quickly providing support when I had a problem with it; Steen G. Hanson, OPL, for discussions on statistical optics and cheerful remarks whenever I run into him; Thorkild Sørensen, now Patent- og Varemærkestyrelsen, for our fruitful collaboration on the nanoengineering paper while he was at DTU; everyone at COM•DTU and OPL for a friendly working environment; everybody else who I probably forgot, but undoubtedly had helpful inspiration from!

John M. Dudley, University of Franche-Comté, France, and Karen M. Hilligsøe, University of Aarhus, are much thanked for their helpful and patient answers to my questions via e-mail.

I must give a special thanks to my close colleague Peter Falk, COM•DTU, for the countless discussions and ideas we've had together, and for sharing the fun and frustrations of life as a Ph.D. student. Also a special thanks to Christina Ankjærgaard, my family, and friends for invaluable support and bringing balance to my work-life.

Reading this document

I know that many acronyms are used in this document, and would therefore like to call the reader's attention to the list of acronyms on page 103.

Hopefully this list will be an aid to the reader. Also, the PDF version of this document[1] contains clickable hyperlinks of acronyms, equations, and references as an extra aid to the reader.

Michael H. Frosz, August 31st 2006

Notes to printed thesis

The results of the thesis were presented for public examination and debate on November 3rd 2006 at the Technical University of Denmark. The evaluation committee consisted of Professor John M. Dudley (University of Franche-Comté, France), Professor Søren R. Keiding (University of Aarhus, Denmark) and Assoc. Professor Karsten Rottwitt (Technical University of Denmark).

Some minor corrections and additions have been made to the originally submitted thesis before printing. Also, citations to papers in press during writing of the original thesis have been updated. The original thesis is available by request.

Michael H. Frosz, November 30th 2006

[1] Available by request to `mf@com.dtu.dk`. At some point in the future, there will be a link to a Ph.D. thesis archive from `http://www.com.dtu.dk`.

Abstract

The extreme spectral broadening of pulses with an initially narrow spectrum propagating in a nonlinear medium is known as supercontinuum generation (SCG). The SC is spatially coherent and the spectral bandwidth can span several hundreds of nanometres. This has applications in, e.g., component characterization, spectroscopy, optical communications, and optical coherence tomography (OCT). This thesis presents a study of SCG in photonic crystal fibres (PCFs) using numerical modelling. The nonlinear physical mechanisms relevant for the thesis are reviewed. It is investigated how the SC spectrum can be shaped by dispersion engineering of the PCF. This is done in 3 different regimes: femtosecond, picosecond, and continuous-wave (CW) pumping. Femtosecond pumping is investigated in five different PCFs with two zero-dispersion wavelengths (ZDWs) and in tapered PCFs. It is found that the spectral broadening is dominated by self-phase modulation in the first millimetres of the fibre, followed by soliton red-shift. The soliton red-shift is limited by the higher ZDW and the generation of dispersive waves. The first observation of an apparent bright-bright soliton pair across the ZDW is also reported. For picosecond pumping it is demonstrated how the spectral width and flatness depends on nanometre scale design of the PCF structure. CW pumping is modelled using a phase noise model to investigate the influence of the pump spectral linewidth on the SC. The results indicate that the broadest and smoothest spectra are obtained using a narrow linewidth pump and a PCF with small anomalous dispersion at the pump wavelength. It is also demonstrated how the time window of the calculations affects the simulation results. Energy transfer during soliton collisions is found to play an important role, and was overlooked in recent work on CW pumped SC generation. Finally, the implications for designing

a SC source for OCT are briefly discussed.

Resumé (Danish abstract)

**Superkontinuumgenerering i fotoniske krystalfibre:
Modellering og spektral formning via styring af dispersionen**

Ekstrem spektral forbredning af smalspektrede pulser, som udbreder sig i et ulineært medium, kaldes for superkontinuumgenerering (SKG). Et SK er rumligt kohærent og den spektrale båndbredde kan spænde over flere hundrede nanometer. Dette er anvendeligt til f.eks. karakterisering af optiske komponenter, spektroskopi, optisk kommunikation og optisk kohærenstomografi (OKT). Denne afhandling omhandler en undersøgelse af SKG i fotoniske krystralfibre ved hjælp af numerisk modellering. De ulineære fysiske mekanismer med relevans for afhandlingen gennemgås. Det undersøges hvordan SK spektret kan formes via styring af krystalfiberens dispersion. Dette gøres for 3 områder: femtosekund, pikosekund og kontinuerlig pumpning. Femtosekund pumpning undersøges i fem forskellige fotoniske krystalfibre med to nul-dispersionsbølgelængder og i såkaldte taperede (indsnævrede) krystalfibre. Den spektrale forbredning viser sig at være domineret af selv-fasemodulation i de første millimeter af fiberen, efterfulgt af soliton rødskift. Soliton rødskiftet er begrænset af den højere nul-dispersionsbølgelængde og dannelsen af dispersive bølger. Den første observation af et tilsyneladende lys-lys soliton par på tværs af nul-dispersionsbølgelængden beskrives. Det demonstreres for pikosekund pumpning hvordan den spektrale bredde og fladhed afhænger af nanometerskala design af krystalfiber strukturen. Kontinuert pumpning modelleres med en fasestøjmodel til at undersøge indflydelsen af pumpens spektrale liniebredde på SK spektret. Resultaterne indikerer at de bredeste og glatteste spektre opnås med en pumpe med snæver liniebredde og en krystalfiber

med lille anomal dispersion ved pumpe bølgelængden. Det demonstreres også hvordan beregningernes tidsvindue påvirker simulerings resultaterne. Det findes at energioverførsel under soliton kollisioner spiller en vigtig rolle, hvilket har været overset i nylige undersøgelser af kontinuert pumpet SKG. Til slut diskuteres kort resultaternes betydning for designet af en SK-kilde til OKT.

List of publications

The following publications form the basis of the present thesis:

Journal publications

[1] M. H. Frosz, P. Falk, and O. Bang, "The role of the second zero-dispersion wavelength in generation of supercontinua and bright-bright soliton-pairs across the zero-dispersion wavelength," Opt. Express **13**(16), 6181–6192 (2005). http://www.opticsexpress.org/abstract.cfm?URI=OPEX-13-16-6181.

[2] P. Falk, M. H. Frosz, and O. Bang, "Supercontinuum generation in a photonic crystal fiber with two zero-dispersion wavelengths tapered to normal dispersion at all wavelengths," Opt. Express **13**(19), 7535–7540 (2005). http://www.opticsexpress.org/abstract.cfm?URI=OPEX-13-19-7535.

[3] M. H. Frosz, T. Sørensen, and O. Bang, "Nanoengineering of photonic crystal fibers for supercontinuum spectral shaping," J. Opt. Soc. Am. B **23**(8), 1692–1699 (2006). http://www.opticsinfobase.org/abstract.cfm?URI=josab-23-8-1692.

[4] M. H. Frosz, O. Bang, and A. Bjarklev, "Soliton collision and Raman gain regimes in continuous-wave pumped supercontinuum generation," Opt. Express **14**(20), 9391–9407 (2006). http://www.opticsinfobase.org/abstract.cfm?URI=oe-14-20-9391.

The abstracts of the above journal publications can be found on p. 105.

Conference contributions

[5] P. Falk, M. H. Frosz, O. Bang, P. E. Andersen, A. Bjarklev, and L. Thrane, "Supercontinuum generation in a photonic crystal fiber tapered to normal dispersion for all wavelengths," in *17th International Conference on Optical Fibre Sensors, OFS-17*, pp. 318–321 (Proceedings of SPIE, Vol. 5855, Bruges, Belgium, 2005). http://dx.doi.org/10.1117/12.623423.

[6] P. Falk, M. H. Frosz, and O. Bang, "The role of tapering and second zero dispersion wavelength for supercontinuum generation in Photonic Crystal Fibers," Annual meeting of the Danish Optical Society (DOPS), poster presentation, 17$^{\text{th}}$–18$^{\text{th}}$ November, Risø National Laboratory, Denmark (2005).

[7] M. H. Frosz, T. Sørensen, and O. Bang, "Nano-engineering of photonic crystal fibers for supercontinuum generation," in *Photonic Crystals and Fibers*, pp. 1–8 (Proceedings of SPIE, Vol. 5950, SPIE-COO, Warsaw, Poland, 2005). http://dx.doi.org/10.1117/12.621796.

[8] M. H. Frosz, O. Bang, A. Bjarklev, P. E. Andersen, and J. Broeng, "Supercontinuum generation in photonic crystal fibers: The role of the second zero dispersion wavelength," in *Conference on Lasers and Electro-Optics*, pp. 1255–1257 (CLEO, Vol. 2, Baltimore, MD, USA, 2005).

[9] M. H. Frosz, P. Falk, L. T. Pedersen, O. Bang, and A. Bjarklev, "Supercontinuum generation in untapered and tapered photonic crystal fibers with two zero dispersion wavelengths," in *Photonic Crystal Materials and Devices III*, pp. 190–197 (Proceedings of SPIE, Vol. 5733, Photonics West, San Jose, CA, USA, 2005). http://dx.doi.org/10.1117/12.601185.

In addition, the following work was published during the Ph.D. project (September 1$^{\text{st}}$ 2003–August 31$^{\text{st}}$ 2006), but is outside the scope of the thesis:

Journal publications

- D. Levitz, L. Thrane, M. H. Frosz, P. E. Andersen, C. B. Andersen, S. Andersson-Engels, J. Valanciunaite, J. Swartling, and P. R. Hansen, "Determination of optical scattering properties of highly-scattering media in optical coherence tomography images," Opt. Express **12**(2), 249–259 (2004). http://www.opticsinfobase.org/abstract.cfm?URI=oe-12-2-249.

- P. E. Andersen, L. Thrane, H. T. Yura, A. Tycho, T. M. Jørgensen, and M. H. Frosz, "Advanced modelling of optical coherence tomography systems," Phys. Med. Biol. **49**(7), 1307–1327 (2004). http://dx.doi.org/10.1088/0031-9155/49/7/017.

- L. Thrane, M. H. Frosz, T. M. Jørgensen, A. Tycho, H. T. Yura, and P. E. Andersen, "Extraction of optical scattering parameters and attenuation compensation in optical coherence tomography images of multilayered tissue structures," Opt. Lett. **29**(14), 1641–1643 (2004). http://www.opticsinfobase.org/abstract.cfm?URI=ol-29-14-1641.

- L. Thrane, D. Levitz, M. H. Frosz, A. Tycho, T. M. Jørgensen, C. B. Andersen, P. R. Hansen, S. Andersson-Engels, H. T. Yura, and P. E. Andersen, "Characterizing tissue optical properties using optical coherence tomography for diagnostics," Optics and Photonics News (special issue: "Optics in 2004") **15**(12), 21 (2004). http://www.osa-opn.org/abstract.cfm?URI=OPN-15-12-19.

Conference contributions

- P. Falk, M. H. Frosz, L. P. Sanz, L. Thrane and A. Tycho, "Compact, portable and modular OCT system," poster presented at BIOP symposium "Biomedical Optics '03", Oct. 28$^{\text{th}}$ (2003).

- M. H. Frosz, T. M. Jørgensen, A. Tycho, L. Thrane, H. T. Yura, and P. E. Andersen, "Monte Carlo modeling of optical coherence tomography systems," in *Coherence domain optical methods and optical coherence tomography in biomedicine VIII*, pp. 214–219 (Proceedings of SPIE, Vol. 5316, Photonics West, San Jose, CA, USA, 2004). http://dx.doi.org/10.1117/12.529279.

- L. Thrane, M. H. Frosz, A. Tycho, T. M. Jørgensen, H. T. Yura, and P. E. Andersen, "Demonstration of the true-reflection OCT imaging algorithm on a heterogeneous multilayered structure," in *Coherence domain optical methods and optical coherence tomography in biomedicine VIII*, pp. 220–225 (Proceedings of SPIE, Vol. 5316, Photonics West, San Jose, CA, USA, 2004). `http://dx.doi.org/10.1117/12.529195`.

- T. Sørensen, N. I. Nikolov, M. Frosz, O. Bang, A. Bjarklev, and J. J. Rasmussen, "Dispersion engineered cob-web photonic crystal fibers for efficient supercontinuum generation," poster at DTU Internal Nanosymposium, Aug. 19th, 2004.

- P. Falk, M. H. Frosz, L. Thrane, O. Bang, P. E. Andersen and A. Bjarklev, "High-resolution, real-time imaging using a fiber-based optical coherence tomography system," DTU Medical Visionday, June 1st, oral presentation, DTU, Kgs. Lyngby, Denmark (2005).

- L. Thrane, M. H. Frosz, D. Levitz, T. M. Jørgensen, C. B. Andersen, P. R. Hansen, J. Valanciunaite, J. Swartling, S. Andersson-Engels, A. Tycho, H. T. Yura, and P. E. Andersen, "Extraction of tissue optical properties from optical coherence tomography images for diagnostic purposes," in *Saratov Fall Meeting 2004: Optical Technologies in Biophysics and Medicine VI*, pp. 139–150 (Proceedings of SPIE, Vol. 5771, 2005). `http://dx.doi.org/10.1117/12.634767`.

- P. Falk, M. Delgado-Pinar, M. H. Frosz, L. Thrane, P. E. Andersen, A. O. Bjarklev and O. Bang, "The influence of input pump polarization on supercontinuum generation in photonic crystal fibers," Presented at Photonics West, January 21–26, oral presentation, #6108-18, January 23rd, San Jose Convention Center, San Jose, California, USA (2006).

Chapter 1

Introduction

1.1 Background

Light with an initially narrow optical spectrum can undergo an extreme spectral broadening known as supercontinuum generation (SCG), when the light is propagating in a nonlinear medium. The phenomenon has been known since the pioneering experiments by Alfano and Shapiro in 1970 [10, 11] (see Ref. [12] for an in-depth account of the history of SCG). Bulk borosilicate glass was used as the nonlinear medium and a picosecond laser as the light source. The nonlinear effects responsible for the spectral broadening require a high light intensity to be efficient. This could occur in the bulk glass due to spatial nonlinear effects resulting in self-focusing of the beam. Improvements in the fabrication technology of optical glass fibres in the 1970's [13], led to the use of optical fibres as the nonlinear medium. The advantage of this is that the beam is confined in the transverse plane of the optical fibre, so that a high beam intensity can be sustained over larger propagation distances. This reduced the requirement of high laser power for efficient broadband generation [14].

Standard optical fibres consist of a cylindrical glass core surrounded by a cladding, with the cladding having a slightly lower ($\sim 0.3\%$) index of refraction than the core [13], see Fig. 1.1 (top). In the simplified ray-picture of light propagation, the light can be said to be confined in the core due to total internal reflection at the interface between core and cladding [15]. Photonic crystal fibres (PCFs) offer a fundamentally different way of guid-

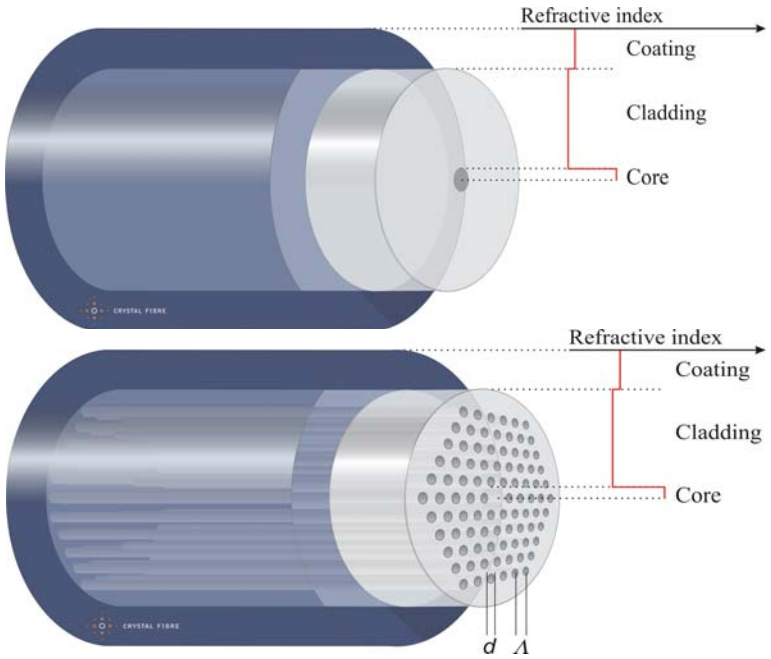

Figure 1.1: *Top:* Standard optical fibre. *Bottom:* Triangular structured PCF. The pitch Λ and air-hole diameter d are indicated. Courtesy of Kim P. Hansen, Crystal Fibre A/S.

ing the light, namely the photonic band gap effect [16, 17]. A PCF typically consists of silica glass and air-holes comprising a transverse microstructure along the fibre, see Fig. 1.1 (bottom). The photonic band gap effect makes it possible to, e.g., guide the light in a hollow air-core, surrounded by a cladding consisting of air-holes in silica. This can be used to study nonlinear effects in a gas contained in the hollow core [18]. However, the most common type of PCF used for SCG is the index-guiding PCF, which relies on an effective index difference between the solid silica core and the surrounding silica cladding with air-holes, for a modified total internal reflection guiding mechanism [17]. This allows guidance in smaller cores than can be achieved with standard fibres, so a higher intensity can be obtained, leading to more efficient nonlinear effects [19]. By varying the parameters of the microstructure, e.g., the size of the air-holes and the distance between them,

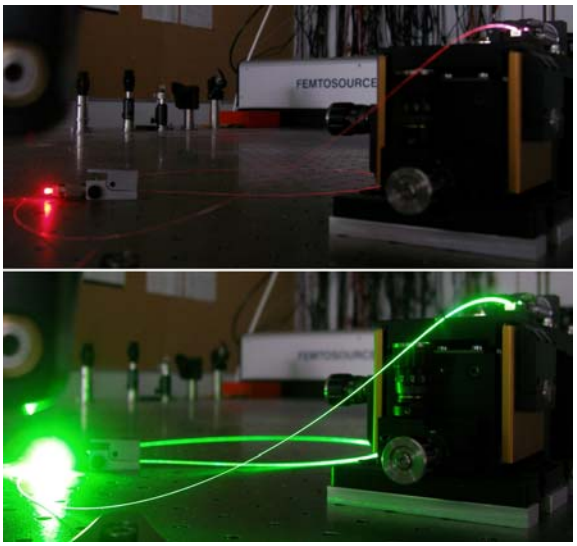

Figure 1.2: *Top:* Light emitted from a PCF pumped with relatively low power infrared light ($\sim$ 800 nm). *Bottom:* The same PCF now pumped with more power. It is seen that a significant amount of green light is generated. Experimental setup and pictures by Peter Falk.

one can also control the dispersion of the fibre, which is a key parameter affecting the supercontinuum (SC) spectrum [13, 20, 21]. PCFs have therefore been a widely used nonlinear medium for practical realizations of SCG in recent years.

1.2 Applications

SCG makes it possible to create light sources with an optical spectrum covering several hundreds of nanometres. Such broad spectra have many both realised and potential applications. The SC spectrum is not only broad, but is also spatially coherent, contrary to light from, e.g., a tungsten lamp, and consequently has higher brightness [19]. The high spectral brightness can be apprehended from Fig. 1.2. SC sources can therefore replace the various white-light sources used in laboratories for measuring, e.g., the wavelength dependent attenuation of optical components over a broad spectral range.

Applications have also been demonstrated in dispersion measurements [22], optical communications [23], spectroscopy [24], sensors [25], and optical frequency metrology [26].

In 2001, Hartl *et al.* demonstrated the feasibility of using SCG for optical coherence tomography (OCT) [27]. OCT is an imaging technique which can be used to obtain micrometre-scale resolution cross-sectional images in highly-scattering media, such as biological tissue [28]. The technique relies on low temporal coherence interferometry analogous to ultrasound echo imaging. Due to the interferometric basis of the technique, the depth resolution Δz of the cross-sectional image is related to the centre wavelength λ_c and the full width at half-maximum (FWHM) bandwidth $\Delta\lambda$ of the light source as [29]

$$\Delta z = \frac{2\ln 2}{\pi}\frac{\lambda_c^2}{\Delta\lambda} \approx 0.44\frac{\lambda_c^2}{\Delta\lambda}, \tag{1.1}$$

if the source spectrum has an approximately Gaussian shape. In general, the source spectrum should be relatively smooth to avoid false echoes in the images [30].

The optimal choice of λ_c depends on the biological medium under investigation. To achieve a good penetration depth the 800 nm wavelength region is optimal for OCT measurements of the eye, due to lower absorption, while the 1300 nm region is considered optimal for measurements of highly scattering tissue such as skin, due to lower scattering (see, e.g., Chapter 1 in Ref. [31]). To achieve higher resolution in OCT measurements of the eye, the 1000 nm wavelength region is better suited because water has zero dispersion at this wavelength, and dispersion acts to smear out the OCT image [32]. Note that, from Eq. (1.1), a $\Delta z = 5$ μm resolution with $\lambda_c = 800$ nm requires a spectral bandwidth of $\Delta\lambda \sim 56$ nm, while the same resolution with $\lambda_c = 1300$ nm requires $\Delta\lambda \sim 149$ nm bandwidth.

From the above, it is desirable to have an OCT light source with a spectrum that is extremely broad (hundreds of nanometres), relatively smooth and flat, and a centre wavelength adjusted to the particular OCT-application. Furthermore, to be used in a clinical environment the light source should also be compact. Femtosecond lasers are typically bulky and complex, but have offered the broadest spectra used for OCT when combined with SCG, see Fig. 1.3.

As seen from Fig. 1.3, SCG has already demonstrated its ability as a

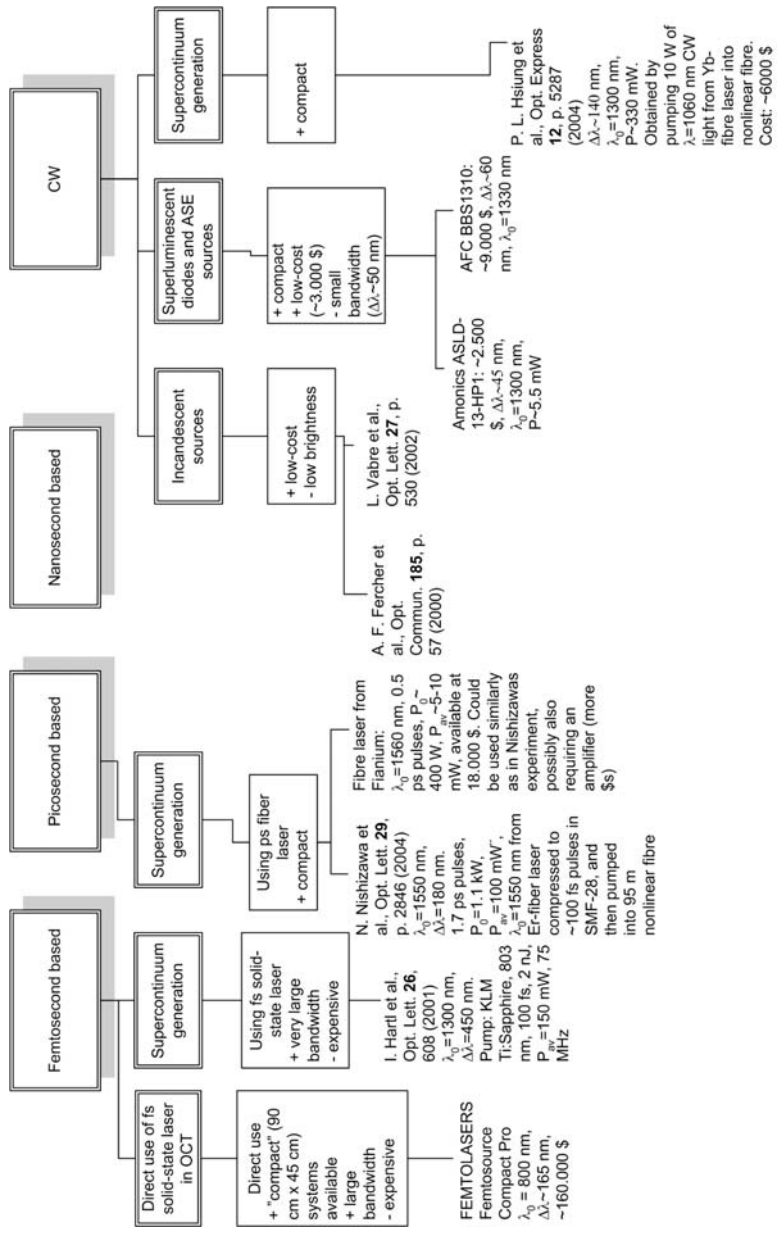

Figure 1.3: Examples of light sources used for OCT divided into pumping schemes (not exhaustive).

basis for OCT light sources. A general trend during recent years has been to develop sources that are cheaper and more compact than systems containing a femtosecond laser, while still obtaining broad spectral bandwidth. To support this development further, it is essential to understand the physical mechanisms underlying the spectral broadening. In particular, it is highly interesting to understand how parameters such as the fibre dispersion together with the nonlinear effects affect the spectrum, since PCFs provide a unique possibility for dispersion engineering. As the control of the SCG is improved through, e.g., dispersion engineering, the high output power requirement of the pumping laser is expected to be reduced, so that its size and price is also reduced further. This could extend the applicability of SCG to much broader areas, such as projectors for the consumer electronics market.

1.3 Scope of thesis

The goal of the Ph.D. project was to obtain a better understanding of how to shape the SC spectrum by varying the properties of the PCF. This includes the ability to obtain spectral power in particular wavelength regions, controlling the flatness of the spectrum, and obtaining a broad bandwidth. Also, since clinical application of the OCT technology requires the development of more compact and cheap sources, it has also been investigated how the pump pulse length affects the broadening mechanisms.

Numerical modelling of the SCG process has been used to improve the understanding of the various physical mechanisms at play. The modelling consisted in solving a form of nonlinear Schrödinger equation (NLSE) which describes the propagation of pulses in optical fibres. It was investigated how the spectrum can be controlled through dispersion engineering, for highly different pumping regimes: femtosecond, picosecond and continuous-wave (CW) pumping.

1.4 Organization of thesis

Chapter 2 reviews the theory of nonlinear fibre optics relevant for this thesis. The propagation equation and its numerical solution are presented. Various

spectral broadening mechanisms are described to provide a basis for their recognition in the following chapters. The properties and advantages of PCFs are described, as well as the calculation of dispersion and effective area. The chapter is concluded with some suggestions for improving the computation speed of the numerical method.

Chapter 3 presents an investigation of SCG in PCFs with two zero-dispersion wavelengths (ZDWs) pumped with femtosecond pulses. The distance between the ZDWs is varied by modifying the structural parameters of the PCFs. This allows a study of the role of the higher ZDW. It is found that the distance between the ZDWs determines whether solitons are formed, and how far they can red-shift into the infrared before amplifying dispersive waves. Femtosecond pumping in a tapered fibre is also investigated. Then the first observation of an apparent bright-bright soliton pair across the higher ZDW is described.

The subject of Chapter 4 is picosecond pumped SCG. It is clearly shown how changing the structural parameters of a PCF on a nanometre scale can significantly influence the width and flatness of the SC spectrum.

Chapter 5 considers SCG using a CW or quasi-CW pump. First, the method of modelling a partially coherent CW pump is presented. Then it is shown that multiple femtosecond solitons are formed from the CW input, and that much of the spectral broadening is due to a physical mechanism also described in Chapter 3, namely soliton red-shift. It is shown that the solitons do not red-shift until they have undergone collisions with each other, in which energy is exchanged between the solitons. It is also demonstrated how the numerical parameters can affect the simulation results, and how the spectral linewidth of the CW pump affects the resulting SC spectrum.

To conclude the thesis, Chapter 6 provides a summary and discussion of the main results obtained. A brief outlook at the future of SCG research is also given.

Chapter 2

Nonlinear optics in optical fibres

The propagation of an electromagnetic (EM) wave or pulse, depends entirely on the medium in which it propagates. In vacuum the pulse can propagate unchanged. When propagating in a medium the EM field interacts with the atoms of the medium. This generally means that the pulse experiences loss and dispersion, where the latter effect occurs because the different wavelength components of the pulse travel at different velocities due to the wavelength dependence of the refractive index. These effects are termed the linear response of the medium. If the intensity[1] of the pulse is high enough, it becomes possible to observe that the medium also responds in a *nonlinear* way. Most notably the refractive index becomes intensity dependent (the Kerr effect) and photons can interact with phonons (molecular vibrations) of the medium (the Raman effect). These effects are the basis for the many spectral broadening mechanisms we will investigate further in this chapter.

In Section 2.1 the equation for modelling pulse propagation is presented. Section 2.2 then reviews the various spectral broadening mechanisms included in the model, that are used to explain the resulting spectra observed

[1] Strictly speaking, the term 'irradiance' would be more appropriate to avoid confusion with the term 'radiant intensity' [15], but 'intensity' is used extensively in the literature (e.g. [13]).

in this work. The properties and modelling of the nonlinear medium of interest here, photonic crystal fibres, is covered in Section 2.3. Section 2.4 describes how to solve the pulse propagation equation using the split-step Fourier method. Finally, Section 2.5 provides some suggestions for improving the split-step Fourier method.

2.1 The generalised nonlinear Schrödinger equation

The electric field of a pulse linearly polarised along the x-axis and propagating in the fundamental mode of an optical fibre can be written as [13]

$$\mathbf{E}_{\mathrm{A}}(\mathbf{r},t) = \hat{x}F(x,y)A(z,t)\exp[i(\bar{\beta}_0 z - \omega_0 t)], \tag{2.1}$$

where $\mathbf{r} = (x,y,z)$, $\hat{x}$ is the polarisation unit vector, $F(x,y)$ describes the transverse field distribution, $A(z,t)$ is the pulse envelope, and $\bar{\beta}_0$ is the mode propagation constant $\beta(\omega)$ at the centre angular frequency ω_0 of the pulse. $\mathbf{E}_{\mathrm{A}}$ is scaled to the actual electric field $\mathbf{E}$ [V/m] according to $\mathbf{E}_{\mathrm{A}} = \sqrt{\frac{1}{2}\epsilon_0 c n}\mathbf{E}$, where ϵ_0 is the vacuum permittivity, c is the speed of light in vacuum, and n is the refractive index. This ensures that the instantaneous optical power can be calculated as $|A|^2$ (see Appendix A.2). The change in pulse envelope A as the pulse propagates along the fibre axis z is described by the generalised nonlinear Schrödinger equation (NLSE) [13, 33–35]

$$\begin{aligned}\frac{\partial \tilde{A}}{\partial z} =& i\sum_{m\geq 2}\frac{\bar{\beta}_m}{m!}\left[\omega-\omega_0\right]^m\tilde{A} - \frac{\alpha(\omega)}{2}\tilde{A} \\ &+ i\gamma(\omega)\left[1+\frac{\omega-\omega_0}{\omega_0}\right]\mathcal{F}\left\{A(z,T)\int_{-\infty}^{\infty}R(T')\left|A(z,T-T')\right|^2\mathrm{d}T'\right\},\end{aligned} \tag{2.2}$$

where $\mathcal{F}$ denotes the Fourier transform and $\tilde{A}(z,\omega)$ is the Fourier transform of $A(z,t)$,

$$\mathcal{F}\left\{A(z,t)\right\} = \tilde{A}(z,\omega) = \int_{-\infty}^{\infty}A(z,t)\exp\left[i\left(\omega-\omega_0\right)t\right]\mathrm{d}t, \tag{2.3}$$

and the pulse envelope $A(z,T)$ is considered in a retarded time frame $T = t - \bar{\beta}_1 z$ moving with the group velocity $1/\bar{\beta}_1$ at the carrier frequency. The

dispersion coefficients $\bar{\beta}_2$, $\bar{\beta}_3$, ..., are defined from the Taylor expansion of the mode propagation constant $\beta(\omega)$ [13]:

$$\beta(\omega) = \bar{\beta}_0 + \bar{\beta}_1[\omega - \omega_0] + \frac{1}{2}\bar{\beta}_2[\omega - \omega_0]^2 + \frac{1}{6}\bar{\beta}_3[\omega - \omega_0]^3 + \ldots, \tag{2.4}$$

where

$$\bar{\beta}_m = \beta_m(\omega_0) = \left(\frac{\mathrm{d}^m\beta}{\mathrm{d}\omega^m}\right)_{\omega=\omega_0}. \tag{2.5}$$

$\alpha(\omega)$ is the power attenuation coefficient. $\gamma(\omega) = n_2\omega_0/[cA_{\mathrm{eff}}(\omega)]$ is the nonlinear parameter, where $n_2 = 2.6 \times 10^{-20}$ m^2/W is the nonlinear-index coefficient for silica[2], and A_{eff} is the effective core area [13]. It is usually defined as [13]

$$A_{\mathrm{eff}}(\omega) = \frac{\left[\iint_{-\infty}^{\infty} |F(x,y,\omega)|^2 \,\mathrm{d}x\mathrm{d}y\right]^2}{\iint_{-\infty}^{\infty} |F(x,y,\omega)|^4 \,\mathrm{d}x\mathrm{d}y}, \tag{2.6}$$

but a more general definition was found by Lægsgaard *et al.*[36]; as explained in Section 2.3 the more general definition is best suited for the present work. $R(t)$ is the Raman response function [13, 33]

$$R(t) = (1 - f_{\mathrm{R}})\delta(t) + f_{\mathrm{R}}h_{\mathrm{R}}(t) \tag{2.7}$$

$$= (1 - f_{\mathrm{R}})\delta(t) + f_{\mathrm{R}}\frac{\tau_1^2 + \tau_2^2}{\tau_1\tau_2^2}\exp(-t/\tau_2)\sin(t/\tau_1)\Theta(t) \tag{2.8}$$

where $f_{\mathrm{R}} = 0.18$ is the fractional contribution of the delayed Raman response, $\tau_1 = 12.2$ fs, and $\tau_2 = 32$ fs. $\Theta(t)$ is the Heaviside step function and $\delta(t)$ is the Dirac delta function. There exists both a parallel and an orthogonally polarised delayed Raman response [37], but the orthogonal component is generally negligible [38, 39] and therefore usually not considered, which is also the approach taken here.

The factor $[1+(\omega-\omega_0)/\omega_0]$ in Eq. (2.2) is responsible for self-steepening and is due to the intensity dependence of the group velocity [13].

The propagation Eq. (2.2) is often written in the time domain by neglecting the frequency dependence of γ, $\gamma = \gamma(\omega_0)$, and α, $\alpha = \alpha(\omega_0)$,

[2]The value of n_2 is slightly wavelength dependent and also depends on the pulse length used when measuring it [13].

and then Fourier transforming Eq. (2.2) using the Fourier transformation replacement property $\partial/\partial t \leftrightarrow -i[\omega - \omega_0]$ [13, 33]:

$$\begin{aligned}\frac{\partial A}{\partial z} =& i\sum_{m\geq 2}\frac{i^m\bar{\beta}_m}{m!}\frac{\partial^m A}{\partial T^m} - \frac{\alpha}{2}A \\ &+ i\gamma\left[1+\frac{i}{\omega_0}\frac{\partial}{\partial T}\right]\left[A(z,T)\int_{-\infty}^{\infty}R(T')\left|A(z,T-T')\right|^2\mathrm{d}T'\right].\end{aligned} \tag{2.9}$$

It should be emphasised that the generalised NLSE is *not* derived under the condition of a slowly varying envelope [33], although this is a common misconception (e.g. [40]). It is only assumed that the nonlinearity is small, that the backward travelling wave can be neglected, and that the bandwidth of $\tilde{A}(z,\omega)$ is less than $\approx \omega_0/3$ [33].

It can be shown that Eq. (2.2) conserves a quantity proportional to the classical photon number of an optical wave [33, 34]:

$$\frac{\partial}{\partial z}\left[\int A_{\mathrm{eff}}(\omega)\frac{\left|\tilde{A}(z,\omega)\right|^2}{\omega}\mathrm{d}\omega\right] = \frac{\partial P}{\partial z} = 0. \tag{2.10}$$

This is used to check the numerical accuracy when solving the generalised NLSE, which is the subject of Section 2.4.

2.2 Physical mechanisms

2.2.1 Self-phase modulation

As mentioned in the introduction of this chapter the refractive index n of a nonlinear medium is intensity dependent. This means that the phase velocity $v_{\mathrm{p}} = c/n$ also becomes intensity dependent. This leads to self-phase modulation (SPM) of a propagating pulse. To study the effect of SPM alone one neglects all dispersion terms, loss, the self-steepening term $(i/\omega_0)\partial/\partial T$, the Raman effect ($f_{\mathrm{R}} = 0$), and the frequency dependence of $\gamma(\omega)$ by using Eq. (2.9) to obtain [13]

$$\frac{\partial A}{\partial z} = i\gamma A\left|A\right|^2. \tag{2.11}$$

The general solution is [13]

$$A(z,T) = A(0,T)\exp[i\gamma\left|A(0,T)\right|^2 z] = A(0,T)\exp[i\phi(z,T)] \qquad (2.12)$$

from which it is seen that the temporal pulse shape $|A|^2$ is unchanged during propagation. The time-dependent phase shift $\phi(z,T)$ gives the pulse a frequency chirp $\delta\omega(T) = -\partial\phi/\partial T$, which is negative near the leading edge of the pulse and positive near the trailing edge of the pulse [13]. This corresponds to a red shift and a blue shift, respectively.

To illustrate the change in pulse spectrum due to SPM alone, Eq. (2.12) has been solved for a Gaussian input pulse [defined in Eq. (A.1)]. The resulting power spectrum [defined in Eq. (A.18)] $S(\nu) \propto \left|\tilde{A}(z,\omega)\right|^2$ is shown in Fig. 2.1 (left) for different propagation distances z. Note that the spectra are symmetric in frequency, but appear asymmetric when plotted properly on a wavelength scale, $S(\lambda) \propto \left|\tilde{A}(z,\omega = 2\pi c/\lambda)\right|^2/\lambda^2$ [Eq. (A.26)], in Fig. 2.1 (right).

2.2.2 Solitons

In the previous subsection it was mentioned that SPM alone red-shifts the leading edge of the pulse, while blue-shifting the trailing edge of the pulse. In the additional presence of normal dispersion the red-shifted part of the pulse will propagate faster than the blue-shifted part [13]. This means that the pulse broadens more quickly in time than if only dispersion was present. On the other hand, anomalous dispersion leads to a delay of red-shifted pulse components and faster propagation of the blue-shifted part of the pulse. SPM thus acts to delay the broadening of a pulse propagating in the anomalous dispersion regime.

It turns out that it is possible for SPM and group-velocity dispersion (GVD) to exactly balance each other, so that a pulse can propagate without changing its shape. Neglecting all terms but those responsible for SPM and GVD, Eq. (2.9) is rewritten as the unperturbed NLSE:

$$\frac{\partial A}{\partial z} = -\frac{i\bar{\beta}_2}{2}\frac{\partial^2 A}{\partial T^2} + i\gamma A\left|A\right|^2. \qquad (2.13)$$

There is a solution to this equation corresponding to a pulse that does not change its shape upon propagation. It is called the fundamental soliton and

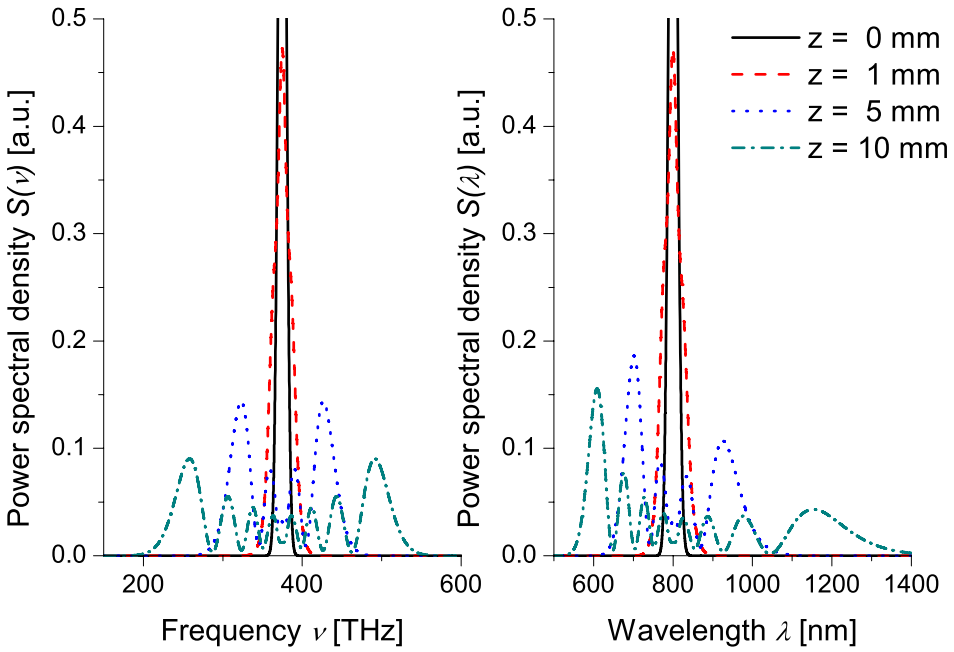

Figure 2.1: Pulse spectra due to SPM induced broadening alone for a Gaussian input pulse with the parameters $T_{\mathrm{FWHM}} = 40$ fs, peak power $P_0 = 16.4$ kW, $\lambda_0 = 800$ nm, and $\gamma = 0.15$ $(\mathrm{Wm})^{-1}$. *Left:* Plotted on frequency scale. *Right:* Plotted on wavelength scale [Eq. (A.26)].

can be found directly by assuming a shape-preserving solution of the form $A(z,T) = V(T)\exp[i\phi(z,T)]$ and inserting it in Eq. (2.13) [13]. The result is

$$A(z,T) = \sqrt{P_0}\mathrm{sech}\left(\frac{T}{T_0}\right)\exp\left[\frac{i\left|\bar{\beta}_2\right|}{2T_0^2}z\right] \tag{2.14}$$

with the condition $N = 1$, where [13]

$$N^2 = \frac{\gamma P_0 T_0^2}{\left|\bar{\beta}_2\right|}. \tag{2.15}$$

N is the soliton order, P_0 is the pulse peak power, T_0 is a measure of the pulse temporal width [see Eq. (A.8)], and sech is the hyperbolic-secant

function. It is seen that the fundamental soliton given by Eq. (2.14) changes neither its shape nor spectrum during propagation.

For integer values of N larger than 1 a higher-order soliton is formed which does not preserve its shape during propagation. Instead, an input pulse with initial shape $A(0,T) = \sqrt{P_0}\mathrm{sech}(T/T_0)$ will change its shape along the fibre, but periodically recover its original shape [13]. The higher-order soliton solutions can be found analytically using the inverse scattering method [41].

2.2.3 Four-wave mixing / Modulation instability

We now consider the propagation of a continuous-wave (CW) or quasi-CW beam. For this purpose losses and the self-steepening term in Eq. (2.9) are neglected:

$$\frac{\partial A}{\partial z} = i\sum_{m\geq 2}\frac{i^m\bar{\beta}_m}{m!}\frac{\partial^m A}{\partial T^m} + i\gamma\left[A(z,T)\int_{-\infty}^{\infty}R(T')\left|A(z,T-T')\right|^2\mathrm{d}T'\right]. \tag{2.16}$$

In comparison with the analysis in Ref. [13] the present analysis, which is similar to the work of Shuang-Chun *et al.* [42], includes all higher-order dispersion terms and the delayed Raman response. The inclusion of the delayed Raman response will be useful for the study presented in Chapter 4. Consider a CW solution with angular frequency $\omega = \omega_0$ and a small perturbation $a(z,T)$ [13],

$$A(z,T) = [\sqrt{P_0} + a(z,T)]\exp(i\gamma P_0 z). \tag{2.17}$$

The exponential function provides the phase shift induced by SPM alone on a CW beam. Inserting Eq. (2.17) in Eq. (2.16) and linearizing in a gives

$$\begin{aligned}\frac{\partial a}{\partial z} =& i\sum_{m\geq 2}\frac{i^m\bar{\beta}_m}{m!}\frac{\partial^m a}{\partial T^m} + i\gamma P_0\left[1-f_\mathrm{R}\right]\left[a+a^*\right]\\ &+ i2\gamma f_\mathrm{R}\left[P_0+\sqrt{P_0}a\right]\int_{-\infty}^{\infty}h_\mathrm{R}(T')\mathrm{Re}[a(z,T-T')]\mathrm{d}T',\end{aligned} \tag{2.18}$$

where * denotes complex conjugate. Separating a into a real and an imaginary part, $a = u+iv$ [42], leads to a system of ordinary differential equations:

$$\frac{\partial \tilde{u}}{\partial z} = -\sum_{m=1} (i\Omega)^{2m+1} \frac{\bar{\beta}_{2m+1}}{(2m+1)!}\tilde{u} - \sum_{m=1} \Omega^{2m} \frac{\bar{\beta}_{2m}}{(2m)!}\tilde{v} \tag{2.19}$$

$$\frac{\partial \tilde{v}}{\partial z} = \left\{ \sum_{m=1} \Omega^{2m} \frac{\bar{\beta}_{2m}}{(2m)!} + 2\gamma P_0[1 - f_{\mathrm{R}} + f_{\mathrm{R}}\tilde{h}_{\mathrm{R}}] \right\} \tilde{u} + i \sum_{m=1} \Omega^{2m+1} \frac{\bar{\beta}_{2m+1}}{(2m+1)!}\tilde{v}, \tag{2.20}$$

where the transformation into the Fourier domain (e.g. $u \rightarrow \tilde{u}$) was done by substituting $\partial/\partial T$ with $-i[\omega - \omega_0] = -i\Omega$. The system of linear differential Eqs. (2.19-2.20) can in principle be solved by finding the eigenvalues of the system matrix. A more direct approach is to assume a solution of the form

$$a(z,T) = a_1 \exp\{i(Kz - \Omega T)\} + a_2 \exp\{-i(Kz - \Omega T)\} \tag{2.21}$$

and insert this in both Eqs. (2.19-2.20) and their inverse Fourier transforms. This leads to the dispersion relation [3]

$$K = \sum_{m=1}^{\infty} \frac{\bar{\beta}_{2m+1}}{(2m+1)!}\Omega^{2m+1} \pm \sqrt{\left[\sum_{m=1}^{\infty} \frac{\bar{\beta}_{2m}}{(2m)!}\Omega^{2m} + 2\gamma P_0(1 - f_{\mathrm{R}} + f_{\mathrm{R}}\tilde{h}_{\mathrm{R}})\right] \sum_{m=1}^{\infty} \frac{\bar{\beta}_{2m}}{(2m)!}\Omega^{2m}} \tag{2.22}$$

where $\tilde{h}_{\mathrm{R}}$ is the Fourier transform of $h_{\mathrm{R}}(t)$ appearing in Eq. (2.7), given by

$$\tilde{h}_{\mathrm{R}}(\Omega) = \frac{\tau_1^2 + \tau_2^2}{\tau_2^2 - \tau_1^2(i + \tau_2\Omega)^2}, \tag{2.23}$$

shown in Fig. 2.2. We now consider the situation where the perturbation frequency Ω is far away from the peak of the Raman gain at 13.2 THz: $\Omega \gg \Omega_{\mathrm{R}} = 2\pi \times 13.2$ THz. In this case, $\tilde{h}_{\mathrm{R}}(\Omega) \approx 0$, as can be seen from Fig. 2.2, and the parametric gain $g = \mathrm{Im}(K)$ of the perturbation is

$$g(\Omega) = \sqrt{-\left[\sum_{m=1}^{\infty} \frac{\bar{\beta}_{2m}}{(2m)!}\Omega^{2m} + 2\gamma P_0(1 - f_{\mathrm{R}})\right] \sum_{m=1}^{\infty} \frac{\bar{\beta}_{2m}}{(2m)!}\Omega^{2m}}, \qquad \Omega \gg \Omega_{\mathrm{R}}. \tag{2.24}$$

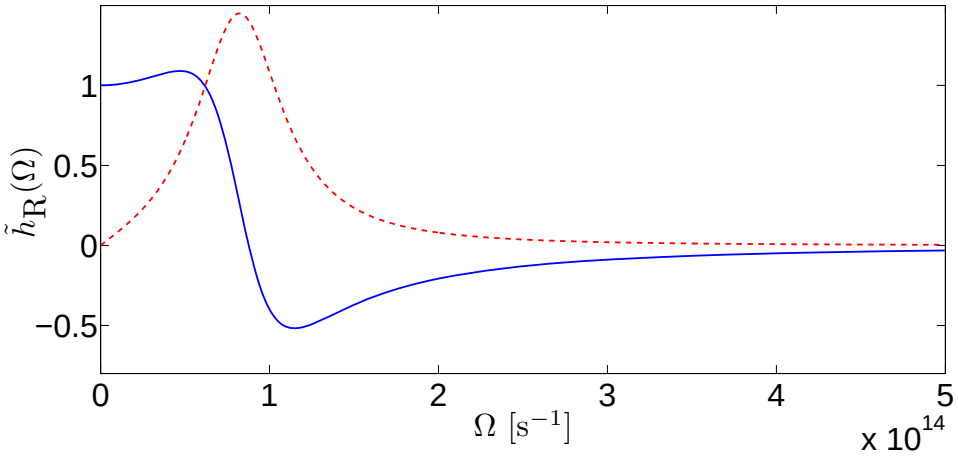

Figure 2.2: The real (blue, solid) and imaginary (red, dashed) part of $\tilde{h}_R(\Omega)$, as given by Eq. (2.23). The peak of the imaginary part occurs at $\Omega = \Omega_R = 2\pi \times 13.2$ THz.

From this it is found that the maximum gain occurs for frequency shifts Ω_0 satisfying

$$\sum_{m=1}^{\infty} \frac{\bar{\beta}_{2m}}{(2m)!}\Omega_0^{2m} = -\gamma P_0(1-f_R)\,, \qquad \Omega \gg \Omega_R. \tag{2.25}$$

The gain can also be written as

$$g(\Omega) = \sqrt{[\gamma P_0(1-f_R)]^2 - (\kappa/2)^2}\,, \qquad \Omega \gg \Omega_R, \tag{2.26}$$

where κ is the phase mismatch given by

$$\kappa = 2\gamma P_0(1-f_R) + 2\sum_{m=1}^{\infty} \frac{\bar{\beta}_{2m}}{(2m)!}\Omega^{2m}\,, \qquad \Omega \gg \Omega_R. \tag{2.27}$$

The form of the perturbation given in Eq. (2.21) corresponds to a periodic modulation $T_{MI} = 2\pi/\Omega$ of the intensity $|A|^2$ of the initial CW field. When the gain $g(\Omega) > 0$ the CW field therefore gradually acquires a periodic modulation known as modulation instability (MI). In the frequency domain

this corresponds to the growth of two sidebands: one downshifted in frequency from the CW carrier frequency, termed the Stokes wave, and one upshifted from the CW carrier frequency, termed the anti-Stokes wave. The angular frequencies of the Stokes and anti-Stokes waves are $\omega_S = \omega_0 - \Omega_0$, and $\omega_{aS} = \omega_0 + \Omega_0$, respectively. Viewed in the frequency domain the process is known as partially degenerate four-wave mixing (FWM) [13], but is clearly a manifestation of the same effect as MI [43].

The influence of FWM on the Raman effect is well-known [44, 45], but the above Eqs. (2.26-2.27) show the influence of the Raman effect on FWM. To the best of the author's knowledge, Frosz *et al.* were the first to directly show that the $(1 - f_R)$ factor appears when $\Omega \gg \Omega_R$ [3]. The consequences of this factor are elaborated further in Section 4.3.

From Eq. (2.26) it is seen that there is gain for FWM if $|\kappa| < 2\gamma P_0(1-f_R)$. This means that partially degenerate FWM will transfer energy from the pump to all the wavelengths for which this condition is fulfilled.

Setting $f_R = 0$ and neglecting all higher-order dispersion terms transforms Eqs. (2.26–2.27) into the corresponding standard textbook (e.g. Ref. [13]) expressions for MI and partially degenerate FWM. A detailed investigation of the relation between FWM and higher-order dispersion has been made by Biancalana *et al.* [40].

Finally, it should be pointed out that the MI/FWM phenomenon occurs for an initially CW or quasi-CW field, as was assumed in the above analysis. For short input pulses, efficient FWM not only requires phase matching ($\kappa \approx 0$), but also that the group velocities of the pump, Stokes, and anti-Stokes waves are matched [13]. Recently, Yulin *et al.* found the generation of new frequencies from FWM of a soliton and a CW field [46].

2.2.4 The Raman effect

The previous physical mechanisms relied on the nonlinear behavior of the material through the Kerr effect, although the influence of the Raman effect on FWM was included in the MI/FWM analysis. The Raman effect originates from the scattering of a photon by molecular vibrations (phonons) in the propagation medium [13]. This leads to the two spectral broadening mechanisms treated in the following.

Raman gain

For a CW or quasi-CW pump the Raman effect transfers energy from the pump to a Raman Stokes wave. The energy difference between the pump photon and the Raman Stokes photon is transferred to a phonon [13]. In silica, the shape of the gain spectrum can be approximated by $\mathrm{Im}[h_\mathrm{R}(\Omega)]$ shown in Fig. 2.2. Note the distinct gain peak at a frequency shift of $\Omega_\mathrm{R} = 2\pi \times 13.2$ THz, which is typically clearly visible when Raman gain is dominant (Chapter 5). The energy transfer from the pump to the Raman Stokes wave requires both waves to be present simultaneously, but the Raman Stokes wave can also buildup from spontaneous scattering [13].

Soliton self-frequency shift

A soliton with a temporal width shorter than ~ 0.1 ps has a spectral width wide enough that energy can be transferred from the high-frequency part of the spectrum to the low-frequency part of the spectrum via the Raman effect [47, 48]. This is called the soliton self-frequency shift (SSFS) and causes the centre frequency ν_0 of the soliton to red-shift during propagation. The rate of red-shift $\mathrm{d}\nu_0/\mathrm{d}z$ can be expressed analytically in two limits. For a soliton duration T_0 much longer than $2\pi/\Omega_\mathrm{R} \approx 76$ fs [13, 48, 49],

$$\frac{\mathrm{d}\nu_0}{\mathrm{d}z} = -\frac{8\,|\beta_2|\,T_\mathrm{R}}{2\pi 15 T_0^4}, \qquad T_0 \gg 76 \text{ fs}, \tag{2.28}$$

where $T_\mathrm{R} \approx 3$ fs is related to the slope of the Raman gain spectrum [13].

For a soliton duration shorter than 76 fs the red-shift rate is given by [49]

$$\frac{\mathrm{d}\nu_0}{\mathrm{d}z} = -\frac{0.09\,|\beta_2|\,\Omega_\mathrm{R}^2}{2\pi T_0}, \qquad T_0 \lessapprox 76 \text{ fs}. \tag{2.29}$$

The red-shift rate $\mathrm{d}\nu_0/\mathrm{d}z$ has been plotted in Fig. 5.7, (p. 81), for the two regimes where Eqs. (2.28–2.29) are valid. The figure is used there to estimate the required soliton width T_0 for a given red-shift.

2.2.5 Amplification of dispersive waves

Since the nonlinear effects require high power to be significant, a CW field with low power can propagate with negligible influence from nonlinearities.

Such a field can therefore be termed a *linear* or *dispersive wave*.

A soliton can transfer energy to a dispersive wave when (1) the soliton and the dispersive wave have equal wavenumbers, and (2) a significant part of the soliton spectral power is at the dispersive wave wavelength [50]. A wavenumber matching expression can be derived as follows [1]. First, the wavenumber (eigenvalue) k_{sol} of a fundamental soliton with temporal width T_{sol} and carrier frequency ω_{sol} is estimated. We assume that the soliton spectrum is narrow enough for k_{sol} to only be slightly perturbed by higher-order dispersion, and neglect this perturbation. One can then find the soliton wavenumber from Eq. (2.14) to be $k_{\mathrm{sol}} = |\beta_2(\omega_{\mathrm{sol}})| / [2T_{\mathrm{sol}}^2]$ [13].

Since the dispersive wave can be generated far from ω_{sol}, we use the NLSE with all the higher-order dispersion terms to estimate the wavenumber k_{lin} of the dispersive wave. However, since the dispersive wave initially has negligible power, the nonlinearity can be neglected by setting $\gamma = 0$:

$$\frac{\partial A}{\partial z} = i \sum_{m \geq 2} \frac{i^m \beta_m(\omega_{\mathrm{sol}})}{m!} \frac{\partial^m A}{\partial T^m}. \tag{2.30}$$

By inserting the expression for a dispersive wave $A_{\mathrm{lin}} = \sqrt{P_{\mathrm{lin}}} \exp\{i[k_{\mathrm{lin}} z - (\omega_{\mathrm{DW}} - \omega_{\mathrm{sol}})t]\}$ into Eq. (2.30), we obtain for $k_{\mathrm{sol}} = k_{\mathrm{lin}}$ [1]

$$\frac{|\beta_2(\omega_{\mathrm{sol}})|}{2T_{\mathrm{sol}}^2} = \sum_{m \geq 2} \frac{\beta_m(\omega_{\mathrm{sol}})}{m!} [\omega_{\mathrm{DW}} - \omega_{\mathrm{sol}}]^m, \tag{2.31}$$

where ω_{DW} is the dispersive wave angular frequency. Since only second-order dispersion is considered for the soliton wavenumber, this equation is, strictly speaking, not valid when the soliton is in the immediate vicinity of the zero-dispersion wavelength (ZDW). However, as will be shown in Section 3.2, the predictions given by this equation show good agreement with the numerical simulations.

In the literature the following names are also used for dispersive waves: linear waves, resonant radiation, and Cherenkov radiation/resonance. It should also be noted that amplification of dispersive waves is a specific case of the general phase matching conditions for FWM of a soliton and a linear wave investigated by Yulin *et al.* [46, 51].

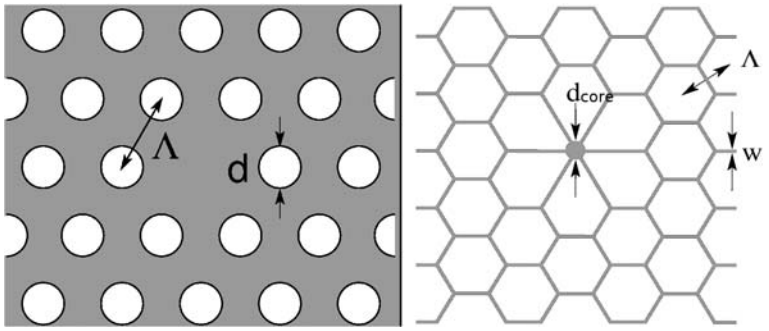

Figure 2.3: *Left:* Sketch of triangular structure PCF with pitch Λ and air hole diameter d. *Right:* Sketch of cobweb PCF with pitch Λ, core diameter d_{core}, and wall thickness w. In both cases the grey areas indicate silica and the white areas indicate air.

2.3 Photonic crystal fibres

As mentioned in the introduction of this chapter efficient nonlinear effects require a high intensity of the optical beam. If the nonlinear medium is, e.g., a bulk crystal, the beam will generally undergo diffraction, thus limiting the region where a high intensity can be obtained. This can be solved by using an optical fibre as the nonlinear medium. An optical fibre confines the light beam to the fibre core during propagation [52]. This allows a long nonlinear interaction length, thus making nonlinear effects efficient.

Standard optical fibres are based on a silica core and cladding (see Fig. 1.1, top), where a refractive index difference between them is made by doping either the core, cladding, or both [52]. The refractive index difference then confines the light by total internal reflection.

A photonic crystal fibre (PCF) is a special type of optical fibre [17]. Instead of doping a material such as silica to obtain a refractive index difference, PCFs can consist of undoped silica containing air holes, or, e.g., a silica core in air only supported by thin silica walls. Examples of such structures are shown in Fig. 2.3 (see also Fig. 1.1, bottom).

2.3.1 Advantages

The index difference between air and silica is much larger than can be achieved through doping of silica [17]. PCFs can therefore provide stronger confinement of light in the core, making it possible to achieve guidance in cores as small as ~ 2 µm diameter [53]. The PCFs can thus be designed with a smaller effective area than in standard fibres, making them highly nonlinear. For a recent review of the properties of nonlinear PCFs, see Ref. [19]. It is also possible not to rely on the index difference for guidance, but to confine light in the core by the photonic band gap effect [16].

As will be shown in the following chapters, it is to a large degree possible to engineer the dispersion of a PCF by proper design of the structural parameters. It is, e.g., possible to design a PCF with two ZDWs in the optical spectrum, where standard fibres have only one ZDW (at $\sim$ 1300 nm for a nonzero-dispersion-shifted fibre), unless the standard fibre is tapered [54] (which is only possible over a limited fibre length) or is made with multiple cladding layers [13]. Since the relative contribution of various nonlinear mechanisms depends on the fibre dispersion profile, PCF dispersion engineering can be used to shape the spectrum of the output pulse [1–9, 21, 55, 56].

2.3.2 Modelling of properties

Considering Eq. (2.2)/(2.9), it is seen that three properties of a PCF must be known to calculate the pulse propagation: the loss α, the dispersion coefficients $\bar{\beta}_2, \bar{\beta}_3, \ldots$, and the nonlinear parameter $\gamma(\omega)$.

The loss can be measured and is often available in PCF datasheets [57]. It was found by Frosz *et al.* that loss has negligible influence on the supercontinuum (SC) spectrum for a 1.2 m long fibre with 300 dB/km attenuation [3], so loss can usually be neglected.

The dispersion parameters can be found using the dispersion profile of the PCF. The dispersion profile can be experimentally measured, but is often measured over a small wavelength range compared to the width of the SC spectrum [57]. As shown below, the dispersion needs to be known over the entire wavelength range of interest. Calculations of the dispersion profile have therefore been used throughout this work. Both fully-vectorial plane-wave expansions [1, 2, 4–6, 8, 9] (based on the freely available MIT

Photonic Bands package [58]) and a semivectorial finite-difference method [3, 7] (described in Refs. [59, 60]) were employed in the dispersion calculations.

By fitting the calculated β_2-dispersion profile [$\beta_2(\omega) = -2\pi c D/\omega^2$, where D is the dispersion parameter [13]] to a polynomial of the form

$$\begin{aligned}\beta_2(\omega) &= \bar{\beta}_2 + \bar{\beta}_3[\omega-\omega_0] + \frac{1}{2}\bar{\beta}_4[\omega-\omega_0]^2 + \frac{1}{6}\bar{\beta}_5[\omega-\omega_0]^3 + \ldots \\ &\approx b_2 + b_3[\omega-\omega_0] + \ldots + \frac{1}{(M-2)!}b_M[\omega-\omega_0]^{M-2} \end{aligned} \tag{2.32}$$

the parameters $b_2, \ldots, b_M$ can be extracted. This is because it is very difficult to accurately calculate the higher-order derivatives necessary in Eq. (2.5) from numerical data. Note that since each b_m-coefficient is obtained from a least-squares polynomial fit, they do not necessarily correspond to the $\bar{\beta}_m$-coefficients as defined in Eq. (2.5). This distinction is often neglected in the literature, where polynomial fits to dispersion curves are widely used (see, e.g., Refs. [20, 61]). The $\bar{\beta}_m$ coefficients in the propagation Eq. (2.2)/(2.9) and Eq. (2.27) can, however, be replaced with the b_m coefficients if the number of fitting coefficients M is large enough, as shown in the following.

The generalised NLSE [Eq. (2.2)] can be written in the Fourier domain as [13]

$$\frac{\partial \tilde{A}}{\partial z} = \left[\hat{D}(\omega) + \hat{N}(z,\omega)\right]\tilde{A} \tag{2.33}$$

where $\hat{D}(\omega)$ is the dispersion operator given by

$$\hat{D}(\omega) = i\sum_{m=1}^{\infty}\frac{\bar{\beta}_m}{m!}[\omega-\omega_0]^m, \tag{2.34}$$

and $\hat{N}$ is the nonlinear operator. [In Eqs. (2.2) and (2.9) the summation runs from $m = 2$ because the $m = 1$ term vanishes when the pulse is considered in a frame of reference moving with the group velocity of the carrier frequency ω_0]. For M sufficiently large, we then have

$$\hat{D}(\omega) = i\sum_{m=1}^{\infty}\frac{\bar{\beta}_m}{m!}[\omega-\omega_0]^m \approx i\sum_{m=1}^{M}\frac{b_m}{m!}[\omega-\omega_0]^m, \tag{2.35}$$

which means that we can use the b_m-coefficients in Eq. (2.2)/(2.9) instead of the $\bar{\beta}_m$-coefficients. M is considered sufficiently large, when the polynomial fit agrees reasonably with the calculated dispersion profile over the entire wavelength range of interest.

Regarding the phase mismatch Eq. (2.27), note that the $\bar{\beta}_m$-coefficients used in the analysis in Section 2.2.3 can be replaced by the b_m-coefficients. The resulting Eq. (2.27) can therefore also have the $\bar{\beta}_m$-coefficients replaced by b_m-coefficients.

To avoid confusion, I will in the following write $\bar{\beta}_m$, even though, strictly speaking, I refer to the least-squares fitted b_m-coefficients.

The nonlinear parameter $\gamma(\omega)$ can easily be calculated once the effective area $A_{\text{eff}}(\omega)$ is known. The expression in Eq. (2.6) for the effective area was derived for a standard fibre [13]. Lægsgaard *et al.* recently found a more general definition of the effective area which is necessary when some of the field energy is located in the air holes of a PCF [36]:

$$A_{\text{eff}} = \left(\frac{n_1}{n_{\text{g},0}}\right)^2 \frac{\left[\int \mathbf{E}^* \cdot \mathbf{D}_r \mathrm{d}A\right]^2}{\int_{\text{SiO}_2} |\mathbf{E}^* \cdot \mathbf{D}_r|^2 \,\mathrm{d}A}, \tag{2.36}$$

where n_1 is the linear refractive index of silica, $n_{\text{g},0} = c/v_{\text{g}}(\omega_0) = c\bar{\beta}_1$ is the effective group index of the guided mode, and $\mathbf{D}_r = \epsilon_r \mathbf{E}$ ($\epsilon_r = n_1^2$). The integration in the numerator is taken over the xy plane, while the integration in the denominator is only taken over the silica regions of the transverse PCF structure.

If all of the field energy is located in the silica regions of the PCF and if $n_{\text{g},0} \approx n_1$, then Eq. (2.36) reduces to [36]

$$A_{\text{eff}} \approx \frac{\left[\int |\mathbf{E}|^2 \,\mathrm{d}A\right]^2}{\int |\mathbf{E}|^4 \,\mathrm{d}A}, \tag{2.37}$$

which is equivalent to the standard definition Eq. (2.6). The general definition Eq. (2.36) is used in the present work. When including the frequency dependence [1, 2, 4–6, 8, 9], $A_{\text{eff}}(\omega)$ was calculated from field distributions found using the fully-vectorial plane-wave expansions [58]. When disregarding the frequency dependence [3, 7], A_{eff} was approximated with the fibre core area.

2.4 The split-step Fourier method

The generalised NLSE [Eq. (2.2)/(2.9)] only has analytic solutions in some cases where mechanisms such as self-steepening, Raman delayed response, and higher-order dispersion can be neglected. An example of an analytic solution is the soliton pulse, given in Eq. (2.14). Since the higher-order nonlinear and dispersion terms are essential for understanding the spectral broadening observed in many experiments, a numerical solution of the propagation equation is required. Since the work of Hasegawa and Tappert in 1973 [62], the *split-step Fourier method* is by far the most widely used [13], and also adopted in the present work. A different approach is to use a finite-difference method, but these are typically more computationally intensive [13] and will not be covered here.

2.4.1 Theory and implementation

As already shown in Eq. (2.33) the generalised NLSE [Eq. (2.2)/(2.9)] can be written in the form

$$\frac{\partial \tilde{A}}{\partial z} = \left[\hat{D}(\omega) + \hat{N}(z,\omega)\right]\tilde{A}, \tag{2.38}$$

where the dispersion operator $\hat{D}(\omega)$ is given by Eq. (2.34), disregarding the loss α and $m = 1$ term, and the nonlinear operator $\hat{N}(z,\omega)$ is given by

$$\hat{N}(z,\omega)\tilde{A} = i\gamma(\omega)\left[1 + \frac{\omega-\omega_0}{\omega_0}\right]\mathcal{F}\left\{A(z,T)\int_{-\infty}^{\infty} R(T')\left|A(z,T-T')\right|^2 \mathrm{d}T'\right\}. \tag{2.39}$$

Using the Fourier convolution theorem $\int A(\tau)B(t-\tau)\mathrm{d}\tau \leftrightarrow \tilde{A}(\omega)\tilde{B}(\omega)$, the nonlinear operator can be calculated using

$$\hat{N}(z,\omega)\tilde{A} = i\gamma(\omega)\left[1 + \frac{\omega-\omega_0}{\omega_0}\right]\mathcal{F}\left\{A(z,T)\mathcal{F}^{-1}\left\{\tilde{R}(\omega)\mathcal{F}\left\{|A(z,T)|^2\right\}\right\}\right\}, \tag{2.40}$$

where $\mathcal{F}^{-1}$ denotes inverse Fourier transform, and $\tilde{R}(\omega)$ is the Fourier transform of $R(t)$, as given by Eqs. (2.7) and (2.23).

The principle of the split-step Fourier method consists of solving Eq. (2.38) for steps h small enough that the dispersive (linear) step and

the nonlinear step can be taken separately [13]. The dispersive step

$$\frac{\partial \tilde{A}_{\mathrm{L}}}{\partial z} = \hat{D}(\omega)\tilde{A} \tag{2.41}$$

has the exact solution

$$\tilde{A}_{\mathrm{L}}(z+h,\omega) = \exp\left[\hat{D}(\omega)h\right]\tilde{A}(z,\omega), \tag{2.42}$$

whereas the nonlinear step

$$\frac{\partial \tilde{A}_{\mathrm{N}}}{\partial z} = \hat{N}(z,\omega)\tilde{A} \tag{2.43}$$

must in general be solved by numerical integration:

$$\tilde{A}_{\mathrm{N}}(z+h,\omega) = \int_{z}^{z+h} \hat{N}(z',\omega)\tilde{A}(z',\omega)\mathrm{d}z'. \tag{2.44}$$

The simplest split-step scheme consists of first propagating the initial pulse with Fourier transform $\tilde{A}(z,\omega)$ a small step h only influenced by the nonlinear effects, followed by the same step size only influenced by dispersion (or vice-versa):

$$\tilde{A}(z+h,\omega) = \exp\left[\hat{D}(\omega)h\right]\int_{z}^{z+h} \hat{N}(z',\omega)\tilde{A}\left(z',\omega\right)\mathrm{d}z'. \tag{2.45}$$

The pulse is repeatedly propagated in small steps h until it reaches the end of the fibre. This scheme is accurate to second order in h, i.e. it is a first order method.

It can be shown that the so-called symmetrized scheme [13, 63],

$$\tilde{A}(z+h,\omega) = \exp\left[\hat{D}(\omega)\frac{h}{2}\right]\int_{z}^{z+h} \hat{N}\left(z',\omega\right)\tilde{A}_{\mathrm{L}/2}\left(z',\omega\right)\mathrm{d}z', \tag{2.46}$$

where $\tilde{A}_{\mathrm{L}/2}(z,\omega) = \exp\left[\hat{D}(\omega)h/2\right]\tilde{A}(z,\omega)$ (thus taking first half a linear step, then a full nonlinear step, and then the last half linear step), is a second order method in h. This is the scheme used in the present work. Note that the number of steps S needed is inversely proportional to the

step size h: $S \propto 1/h$. Therefore the *global* error is of one order lower than the *local* error [64]. For the symmetrized scheme the global leading error term is therefore of second order in h. The numerical integration of $\hat{N}(z,\omega)\tilde{A}$ is done using a fourth-order Runge-Kutta method, which requires four evaluations of $\hat{N}$ [65]. Since there are three Fourier transforms in each evaluation of $\hat{N}$ this brings the number of Fourier transforms for each step h up to 13, including one to obtain A in the time domain after the dispersive step in the Fourier domain.

The Fourier transform operation is performed using a fast Fourier transform (FFT) algorithm [65]. This is the most computationally demanding part of the split-step Fourier method. The primary tasks in decreasing the propagation simulation time is therefore: reducing the number of FFTs (Subsection 2.4.2) and/or using a fast implementation of the FFT algorithm (Subsection 2.4.3).

Note that if self-steepening and the delayed Raman response can both be neglected, the nonlinear operator becomes much simpler:

$$\hat{N}(z,\omega)\tilde{A} = i\gamma(\omega)\mathcal{F}\left\{A(z,T)\,|A(z,T)|^2\right\}. \tag{2.47}$$

In this case each evaluation of $\hat{N}\tilde{A}$ requires only one FFT and one inverse FFT to obtain A in the time domain. Furthermore, there is an analytical solution to the nonlinear step in the time domain, shown in Eq. (2.12), so the numerical integration [Eq. (2.44)] can be avoided. Thus two FFTs are required for a step h, and the calculations become roughly 6.5 times faster than the scheme involving a fourth-order Runge-Kutta numerical integration.

2.4.2 Adaptive step size method

A standard approach to the split-step Fourier method is to use a constant step size h from fibre input to fibre output. The validity of the numerical results is typically ensured by requiring that the relative change in photon number [Eq. (2.10)] at the fibre output is small, say, less than 5%. In the limit of vanishing nonlinearity, $\gamma \to 0$, the step size h can be increased because the error in splitting the dispersive and the nonlinear step decreases. This is also the case when dispersion, self-steepening, and Raman effects

are negligible, since then numerical integration of $\hat{N}$ is unnecessary. On the other hand, a small step size is required when both dispersion and nonlinear effects are non-negligible. A pulse with high peak power will therefore require a small step size to retain a small change in photon number. But, the pulse can evolve during propagation so that, e.g., the peak power decreases due to dispersion. An example of this is shown in Chapter 3. It is also possible to start with a low power quasi-CW pulse, which then forms high peak power solitons from MI. Examples of this are shown in Chapter 5. In both cases, it would be more efficient to gradually adapt the step size during propagation, thereby keeping the total number of FFTs to a minimum.

In the work presented here an adaptive step size method was used for the above reasons. The implementation was based on the algorithm outlined by Sinkin *et al.* [64]. The choice of step size is based on an estimate of the relative local step error. The true local error cannot be found because the true solution is unknown. Therefore an estimate of the local error is made by comparing a coarse solution and a fine solution. The coarse solution $\tilde{A}_{\mathrm{c}}(z+2h,\omega)$ is made by propagating the pulse $\tilde{A}(z,\omega)$ from z to $z+2h$ in one step of length $2h$; the fine solution $\tilde{A}_{\mathrm{f}}(z+2h,\omega)$ is made by propagating $\tilde{A}(z,\omega)$ from z to $z+2h$ in two steps of length h. The local error estimate is then [64]

$$\delta = \frac{\|\tilde{A}_{\mathrm{f}} - \tilde{A}_{\mathrm{c}}\|}{\|\tilde{A}_{\mathrm{f}}\|}, \tag{2.48}$$

where $\|\tilde{A}(z,\omega)\| = (\int |\tilde{A}(z,\omega)|^2 \mathrm{d}\omega)^{1/2}$. The algorithm calculates the error estimate δ for each step. If δ is much larger than some predefined local goal error, δ_{G}, the calculation is repeated with half the step size without taking a step forward. If δ is only slightly larger than δ_{G} the step forward is taken, but the next step size is made slightly smaller. When δ is much smaller than δ_{G} the step forward is also taken, and the next step is made larger to increase the total computation speed [64].

One disadvantage of this approach is that one calculates three propagation steps ($1 \times 2h$ and $2 \times h$) to get to $z+2h$, which might as well be done by calculating only two propagation steps of size h. This means that 50% more FFTs are required. However, it can easily be shown that a linear

combination of the coarse and the fine solution [64],

$$\tilde{A}_4(z+2h,\omega) = \frac{4}{3}\tilde{A}_{\mathrm{f}}(z+2h,\omega) - \frac{1}{3}\tilde{A}_{\mathrm{c}}(z+2h,\omega), \tag{2.49}$$

has a leading error term of fourth-order in h, which is one order higher than the standard symmetrized scheme. Higher order does not always mean higher accuracy [64, 65], so the cost of 1.5 times more Fourier transforms is not necessarily compensated. But, as will be demonstrated in Chapter 3, it is possible for the step size to increase by a factor of 100 from fibre input to output, thus greatly decreasing the total number of FFTs required.

A suggestion for an improvement of the adaptive step size method is given in Section 2.5.

2.4.3 Parallelization

The previous subsection dealt with making the split-step Fourier method efficient in terms of using a minimum number of FFTs. Another improvement of the method is to decrease the computation time of each FFT.

The FFT algorithm used in this work is from Ref. [65], which is known not to be the most efficient. The so-called fastest Fourier transform in the West (FFTW) library should be up to ~ 8 times faster [66, 67], but the author was only recently made aware of this, so FFTW has not yet been implemented in the split-step code. However, the most promising potential of using the FFTW library is the possibility of parallelizing the computation task by splitting each FFT into C calculations, which can then be distributed on C computer processors. Ideally, the FFT computation speed would then be increased by a factor of C, but some computation time is wasted on the splitting and in the communication between processors. To test how much speed can be gained from parallelization in practice, the FFTW utility `fftw_mpi_test` has been used on two different computer systems: `mary.risoe.dk` and `bohr.gbar.dtu.dk`. The `mary` cluster consists of 240 individual PCs with 3.2 GHz CPUs [68]. The memory is distributed, meaning that each PC has its own memory. The `bohr` server consists of 48 CPUs running at 1200 MHz and shared memory [69], meaning that each CPU has fast access to the memory. The results of the parallelization test are shown in table 2.1.

Number of processors C	Parallel speedup `mary`	Parallel speedup `bohr`
4	0.3–0.38	2.0–2.6
8	0.5–0.58	3.3–4.2
16	0.9–1.17	4.0–5.9
32	0.62–0.63	0.2–0.95

Table 2.1: Achieved speedups from parallelization for an FFT with 2^{17} points. A speedup of 1 means that the speed is the same as without parallelization, and a speedup of 2 means that the parallel FFT is twice as fast.

It is seen that for both computer systems the optimal number of processors is 16, because using more processors increases the communications costs more than the increase in computational benefits. The communications costs for the distributed memory system on `mary` are also so severe that there is no benefit in using the parallel FFT on this system. There is, however, also no advantage in using the `bohr` system with shared memory due to the difference in individual CPU speed: the uniprocessor time for one FFT with 2^{17} points on `mary` is ~ 20 ms, while the time for one parallel FFT on `bohr` using 16 CPUs is $\sim$ 20–26 ms. This test therefore indicates that the split-step Fourier method would not be faster if a parallel FFT is used, except if a computer system is available with both shared memory and CPUs with clock frequency larger than 1200 MHz.

It should be mentioned that the test on the `bohr` server was made with an FFTW version using the so-called message passing interface (MPI) communications protocol, which is made for distributed memory systems, even though `bohr` has shared memory. Later tests using an FFTW version using *OpenMP* software, which is suited for shared memory systems, showed that the time for one FFT with 2^{17} points could be reduced to $\sim$ 16 ms [70]. Compared to `mary` the computation time for one FFT is thus reduced 20%. It should be kept in mind, however, that the 20% time reduction comes at a cost of using 16 CPUs for one simulation. In some cases (e.g. the investigations in Chapter 5), it is desired to run several simulations differing only by the input pulse parameters. One could, e.g., use 16 of `mary`s CPUs to make 16 simultaneous simulations (using non-parallelized FFTs) in the time t, while using 16 of `bohr`s CPUs to make 16 simulations in series (us-

ing parallel FFTs), would take the time $16 \times (1 - 0.2)t \approx 13t$. Whether parallelization is an advantage therefore not only depends on the available computer hardware, but also on whether only one or several simulations are required.

2.5 Suggestions for improving the split-step Fourier method

2.5.1 Improvement of the adaptive method

The adaptive step size method requires the selection of a local goal error, δ_{G}. The algorithm then continuously modifies the step size to ensure that the local error δ is close to the goal error: $\delta \approx \delta_{\mathrm{G}}$. A naive attempt to properly choose δ_{G} could be a trial-and-error estimate for short propagation lengths, until the rate of change in photon number, $\partial P/\partial z$, seems appropriate. An example would be to propagate over, say, 10 cm and find the δ_{G} that results in a photon number change less than 0.005%. The naive guess would then be that this is suitable if the change in photon number after 100 m of propagation must be less that 5%. However, this would require that the adaptive step size method ensures that the photon number changes linearly along the fibre, i.e. $\partial P/\partial z =$ constant. As seen in Fig. 2.4 (solid plots), it does not.

For the simulation parameters in Fig. 2.4 MI results in the formation of solitons which red-shift along the fibre (this is studied in depth in Chapter 5). The formation of solitons with high peak power and their red-shift requires a reduction in step size to lower the change in photon number along the fibre. As shown in Fig. 2.4 (solid plots) the adaptive step size method by Sinkin *et al.* [64] does reduce the step size, but not enough to keep $\partial P/\partial z$ constant. Note that the increase in $\partial P/\partial z$ would be even larger if a constant step size method was used.

A first attempt by the author to improve the adaptive method was to let the step size selection depend on the local error relative to the step size, δ/h, instead of depending only on δ. The algorithm would then use a goal error parameter δ_{Gh} to continuously adapt the step size so that $\delta/(h/L) \approx \delta_{\mathrm{Gh}}$ (the relative step size h/L is used to make δ_{Gh} dimensionless). This improved adaptive method was used by Frosz *et al.* in the work presented

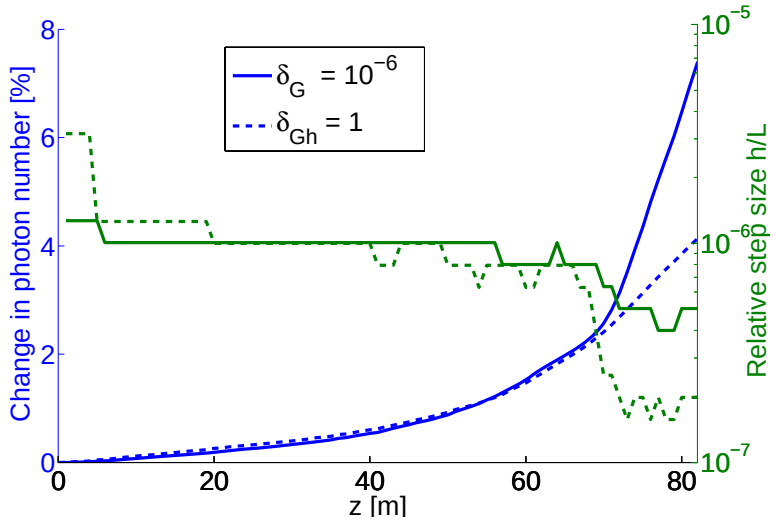

Figure 2.4: Relative change in photon number (blue) and relative step size h/L (green), when using either the step size selection criteria $\delta \approx \delta_{\mathrm{G}} = 10^{-6}$ (solid) or $\delta/(h/L) \approx \delta_{\mathrm{Gh}} = 1$ (dashed). Parameters: $L = 100$ m, $\Lambda = 1.72$ µm, $d/\Lambda = 0.65$, quasi-CW input with $\lambda_0 = 1064$ nm, $P_0 = 10$ W, $2T_{\mathrm{sG}} = 30$ ps and $\Delta\nu_{\mathrm{FWHM}} = 30$ GHz (CW parameters are explained in Chapter 5). The spectra obtained using the two methods are compared in Fig. 5.3.

in Chapter 5 [4]. The results are shown in Fig. 2.4 (dashed plots). δ_{Gh} was chosen so that the change in photon number for short propagation lengths was similar to that with the basic adaptive method. The improved adaptive method does indeed decrease the sudden rise in $\partial P/\partial z$ after $z \approx 70$ m, which the basic adaptive method suffers from.

However, the improved adaptive method still does not ensure that $\partial P/\partial z$ is constant along the fibre. This means that with each new simulation one cannot be sure that δ_{Gh} is chosen sufficiently small that the photon number does not change more than a desired limit. Choosing δ_{Gh} too small, on the other hand, would give a more accurate result, but could take more computation time than is actually needed for the desired accuracy. An additional improvement, not yet implemented, could be to use $\partial P/\partial z$ as a step size selection criterion, instead of the local goal error δ_{G}. It is only slightly more computationally demanding to calculate the photon

number P [Eq.(2.10)] than the local error estimate δ [Eq. (2.48)]. Furthermore, the local goal error calculation requires the calculation of both two steps with step size h and one step with step size $2h$; this is unnecessary if $\partial P/\partial z$ is used as a step size selection criterion.

2.5.2 Simplifying the nonlinear step

As mentioned in Subsection 2.4.1, a fourth-order Runge-Kutta has been used to solve the nonlinear step. This numerical integration method requires four evaluations of $\hat{N}$, each of which requires three FFTs, and is therefore responsible for a large part of the computational effort. In the present work it has not actually been verified that the fourth-order Runge-Kutta is always required. It is possible that the step size h is often so small that a second-order Runge-Kutta can be used, which requires only two evaluations of $\hat{N}$ [65]. Future work could include an investigation of when this approximation is valid, and/or the implementation of an automatic selection of the numerical integration method based on an estimate of the integration error.

Chapter 3

Femtosecond pumping

Femtosecond lasers can provide pulses shorter than 10 fs and a peak power in the range of MWs (see, e.g., Ref. [71] for a recent review). The short pulse duration in itself provides the pulses with a broad spectrum: an ideal Gaussian shaped pulse of 10 fs duration [power full width at half-maximum (FWHM)] and 800 nm centre wavelength has a FWHM power spectral bandwidth of $\sim$ 90 nm [see Eq. (A.5)]. Coupling the pulses into a photonic crystal fibre (PCF) can broaden the spectrum even further using supercontinuum generation (SCG) [72]. The high peak power facilitates the study of nonlinear mechanisms in fibres as short as a few millimetres [1, 73]. Apart from broadening the spectrum, SCG can be used to transfer energy from the pump wavelength to wavelengths that are better suited for a specific application. A recent demonstration of this was made by Aguirre *et al.*, who pumped at 1064 nm and used nonlinear broadening mechanisms to obtain a spectrum with two peaks at 800 nm and 1300 nm, respectively [74]. As mentioned in Chapter 1, the 800 nm wavelength region is optimal for optical coherence tomography (OCT) measurements of the eye, while the 1300 nm region is considered optimal for measurements of highly scattering tissue such as skin.

The first 4 sections of this chapter consider femtosecond pumping of PCFs with two zero-dispersion wavelengths (ZDWs). It is well known that the gain bandwidth for four-wave mixing (FWM) is widest in the vicinity of the ZDW due to phase matching conditions [13, 20], and that solitons in the vicinity of the ZDW can amplify dispersive waves in the normal dispersion

region (NDR) [50, 51, 56]. Therefore, PCFs with two (or more) ZDWs could prove advantageous for efficient supercontinuum generation and spectral shaping.

This chapter first presents an investigation of the physical broadening mechanisms in the first few millimetres of the fibre (Section 3.1). Section 3.2 then investigates how the supercontinuum (SC) spectrum can be controlled by shifting the higher ZDW. Section 3.3 presents the first finding of a pulse structure that could be termed a bright-bright soliton pair. Finally, spectral control by tapering the fibre is investigated in Section 3.4.

3.1 Self-phase modulation with or without four-wave mixing

Supercontinuum generation in PCFs with two closely lying ZDWs was first presented by Hilligsøe *et al.* [73]. They used 40 fs pulses and obtained a double peaked spectrum at $\sim$ 600 and 1200 nm. The resulting spectrum was explained as a result of self-phase modulation (SPM) and FWM. This explanation was then adopted by Tse *et al.* who used 380 fs pulses [75]. Both Refs. [73] and [75] present phase matching curves (graphical solutions to the phase match condition $\kappa = 0$ showing the location of the Stokes and anti-Stokes wavelengths as a function of pump wavelength) to support their claim that FWM plays a role in the spectral broadening. Hilligsøe *et al.* use the phase matching condition [13, 73]

$$\kappa = \beta(\omega_{\mathrm{S}}) + \beta(\omega_{\mathrm{aS}}) - 2\beta(\omega_0) + \Delta k_{\mathrm{NL}} \tag{3.1}$$

where $\Delta k_{\mathrm{NL}} = 2\gamma P_0(1 - f_{\mathrm{R}})$ is the nonlinear phase contribution. By use of Eq. (2.4) this condition can easily be shown to be equivalent to Eq. (2.27). Tse *et al.* do not specify their phase matching condition, but refer to Ref. [76] regarding FWM, where Eq. (3.1) was also used.

The use of Eq. (3.1) and the corresponding phase matching curves is validly used in Ref. [76] because it concerns continuous-wave (CW) pumping. As mentioned in Subsection 2.2.3, the analysis leading to Eq. (3.1) assumes that the pump is either CW or quasi-CW (see Subsection 2.2.3 or Ref. [13]). It is therefore, strictly speaking, invalid to use Eq. (3.1) when considering pulses of 40 or 380 fs duration. As also mentioned in Subsection 2.2.3,

efficient FWM for pulses that cannot be considered CW or quasi-CW requires not only phase matching but also group velocity matching [13]. The phase matching curves presented in Refs. [73, 75] can therefore not be used to support the claim that FWM plays a role in the spectral broadening.

It could be claimed that group velocity mismatch can be neglected over short fibre lengths, but this does not necessarily make the use of Eq. (3.1) valid, and FWM is not required to explain the observed spectral formation. First, the spectra presented in Fig. 2.1 were calculated for parameters similar to those used by Hilligsøe *et al.* in Ref. [73]. Even though only SPM is included in the calculations leading to Fig. 2.1, the spectrum for 10 mm of propagation shows that most of the spectral energy is located at ~ 600 and 1200 nm, as was measured experimentally by Hilligsøe *et al.* in Ref. [73]. Second, it was shown by Frosz *et al.* that even though changing the dispersion parameters can significantly shift the FWM Stokes and anti-Stokes wavelengths, the peaks in the corresponding calculated spectra shift very little [1]. It is shown in Fig. 3.1 (right) that the wavelengths with minimum absolute phase mismatch $|\kappa|$ are at ~ 700 and 950 nm when all higher-order dispersion terms are included. Neglecting the higher-order dispersion terms shifts these wavelengths to ~ 510 and 1900 nm, respectively. One would therefore expect that spectral peaks arising from FWM would make a similar shift in corresponding simulations. As seen in Fig. 3.1 (left), this is not the case. The double peaks at ~ 600 and 1000 nm for the full simulation only move slightly away from the pump when higher-order dispersion is neglected. Considering again Fig. 2.1, it is seen that SPM is sufficient to explain the transfer of spectral power to ~ 700 and 900 nm for a slightly shorter fibre ($z = 5$ mm). It must therefore be concluded that FWM does not play a significant role for the case of femtosecond pumping in millimetre length fibres, considered in this section.

Finally, it should be mentioned that the influence of FWM was tested in Ref. [73] by shifting the dispersion of the fibre to normal dispersion for all wavelengths, $\beta_2(\omega) \rightarrow \beta_2(\omega) + \beta'$, thus removing the possibility of phase matched FWM. A significantly weaker spectral broadening was then observed, and from this it was concluded that FWM plays an important role. However, in the normal dispersion regime SPM and group-velocity dispersion (GVD) will act together to broaden the pulse temporally significantly faster than in the anomalous dispersion regime [13]. Shifting the dispersion to

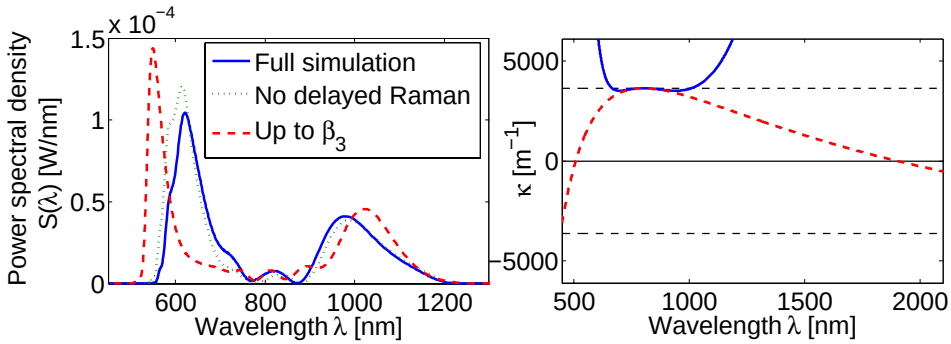

Figure 3.1: *Left:* Simulated power spectra after 6 mm of propagation, using all higher-order dispersion (up to $\bar{\beta}_{15}$) and nonlinear effects (blue, solid); higher-order dispersion included but no delayed Raman response, $f_{\mathrm{R}} = 0$ (green, dotted); Raman effect included but only including dispersion terms $\bar{\beta}_2$ and $\bar{\beta}_3$ (red, dashed). *Right:* Phase mismatch κ when including dispersion terms up to $\bar{\beta}_{14}$ (blue, solid) and when only $\bar{\beta}_2$ is included (red, dashed). (Note that the uneven dispersion coefficients $\bar{\beta}_3, \bar{\beta}_5, \ldots, \bar{\beta}_{15}$ do not contribute to the phase mismatch.) The horizontal solid black line indicates phase match ($\kappa = 0$) and the horizontal dashed lines indicate the region for FWM gain [$|\kappa| < 2\gamma P_0(1 - f_{\mathrm{R}})$]. Parameters: $\Lambda = 1.0$ µm, $d/\Lambda = 0.57$ fibre (dispersion profile shown in Fig. 3.2, left), $P_0 = 15$ kW, $\gamma(\lambda = 804\text{ nm}) = 0.148\ (\mathrm{Wm})^{-1}$, and $T_{\mathrm{FWHM}} = 13$ fs [1].

normal dispersion for all wavelengths will therefore weaken the SPM induced spectral broadening, and this could explain the observations made in [73].

3.2 The role of the higher zero-dispersion wavelength

This section considers propagation in longer fibres than in the previous section.

As shown in Fig. 3.2 (left) it has been found that by modifying the pitch Λ and hole size d of the triangular hole structure the lower ZDW remains constant at ∼780 nm, while the higher ZDW varies between 950 nm and 1650 nm [1, 8, 9]. This allows an investigation of the role of the higher ZDW, which is the subject of this section. The dispersion profiles of the

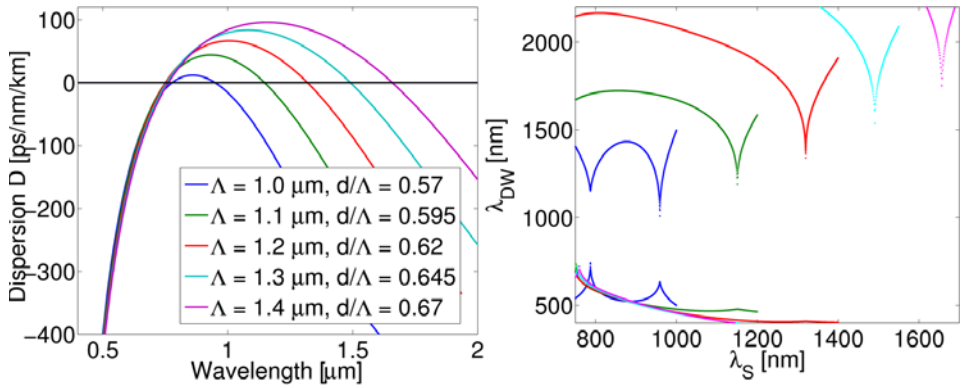

Figure 3.2: *Left:* Calculated dispersion profiles for 5 triangular PCFs with pitch Λ and relative air-hole size d/Λ given in the inset. *Right:* Wavelength λ_{DW} of dispersive waves vs. the soliton centre wavelength λ_{S}; the soliton temporal width is given by Eq. (3.3). The colour labelling is the same in both figures.

fibre with $\Lambda = 1.0$ μm and the fibre with $\Lambda = 1.4$ μm are similar to the dispersion profile of the fibre examined by Hilligsøe *et al.* [73] and Genty *et al.* [56], respectively. $A_{\mathrm{eff}}(\lambda = 804\ \mathrm{nm})$ is 1.38 $\mu\mathrm{m}^2$ for the fibre with $\Lambda = 1.0$ μm and increases with the pitch Λ. For the $\Lambda = 1.4$ μm fibre, $A_{\mathrm{eff}}(\lambda = 804\ \mathrm{nm})$ is 1.97 $\mu\mathrm{m}^2$.

Input parameters

To focus on the influence of the higher ZDW, the same input pulse parameters have been used for all the simulations in this section: the pump wavelength is $\lambda_0 = 804$ nm, the pulse is Gaussian shaped with a power FWHM of $T_{\mathrm{FWHM}} = 13$ fs, and the peak power is $P_0 = 15$ kW. When calculating the power spectral density $S(\lambda)$, a repetition rate f_{rep} of 80 MHz is assumed; the power spectral densities presented here are normalized so that $\int S(\lambda)\mathrm{d}\lambda = P_{\mathrm{av}}$ [see Eq. (A.26)], where P_{av} is the average pulse power of the input pulse [Eq. (A.6)]. These parameters are realizable with commercially available femtosecond lasers. Hilligsøe *et al.* [73] used a fibre length up to 5 cm. Genty *et al.* [56] used a fibre length up to 1.5 m, but found that the continuum generation was complete after 50 cm of propagation. In this

work a propagation length up to 60 cm, 52 cm, and 60 cm, was simulated for the fibres with $\Lambda \leq 1.2$ μm, $\Lambda = 1.3$ μm, and $\Lambda = 1.4$ μm, respectively [1].

2^{15} points were used in the simulations, unless otherwise stated, with a temporal resolution $\Delta t = 1.4$ fs. The local goal error used in the adaptive step-size method was set to $\delta_{\mathrm{G}} = 10^{-8}$ for the fibres with a pitch $\Lambda \leq 1.2$ μm, and $\delta_{\mathrm{G}} = 10^{-9}$ for the fibres with a pitch $\Lambda \geq 1.3$ μm. These local goal errors were found by trial-and-error to give a sufficiently low change of photon number along the fibre length for the total change in photon number to be acceptable (Subsection 2.5.1). For the $\Lambda = 1.0$ μm PCF, this resulted in a step size of ~ 50 nm in the beginning of the fibre which increased gradually along the fibre until it was ∼6 μm at the end of the fibre. As is shown in the following, much of the power launched into the $\Lambda = 1.0$ μm PCF is rapidly moved to the normal dispersion region, such that only a small amount of power is left for solitons in the anomalous dispersion regime. This causes the pulse to spread temporally, resulting in a lower peak power and lower nonlinearities, which allows the adaptive step-size algorithm to automatically increase the step size, and thereby also the computation speed. On the other hand, in the $\Lambda = 1.2$ μm PCF the soliton retains a large peak power and the step size is initially ∼60 nm in the beginning of the fibre and increases to only ∼0.6 μm at the end of the fibre. The relative change in photon number was less than 0.2% for all simulations in this section. To better visualize the pulse dynamics, the pulse will often be considered simultaneously in the time and spectral domain using spectrograms calculated as [73, 77]

$$S(z,t,\omega) = \left| \int_{-\infty}^{\infty} e^{-i[\omega-\omega_0]t'} e^{-[t'-t]^2/\alpha_{\mathrm{sp}}^2} A(z,t') \mathrm{d}t' \right|^2 . \tag{3.2}$$

The spectrogram displays the relative temporal positions of the frequency components of the pulse, and is similar to a cross-correlation frequency-resolved optical gating (X-FROG) measurement [78]. The spectrograms use a window size $\alpha_{\mathrm{sp}} = 16$ fs and are normalized to $S(0,0,\omega_0)$, unless otherwise noted.

Physical mechanisms

When the pump peak power P_0 and width T_0 are sufficiently high for a higher-order soliton to form [Eq. (2.15)], perturbations to the unperturbed nonlinear Schrödinger equation (NLSE) [Eq. (2.13)] can cause the soliton to breakup into N fundamental solitons with different peak powers and temporal widths [13]. The shortest fundamental soliton has the highest peak power, and its width is given by [79, 80]

$$T_{\mathrm{sol}} = \frac{T_0}{2N-1} = \frac{T_0}{2\sqrt{(\gamma P_0 T_0^2/\left|\beta_2(\omega_{\mathrm{sol}})\right|)} - 1}. \tag{3.3}$$

The fundamental solitons can amplify dispersive waves, as described in Subsection 2.2.5, and undergo a red-shift, as described in Subsection 2.2.4. The amplification of dispersive waves is investigated by inserting Eq. (3.3) into Eq. (2.31) which is then solved for each fibre dispersion profile. It is assumed that the fundamental soliton temporal width T_{sol} is unchanged as the soliton is down-shifted in frequency due to soliton self-frequency shift (SSFS); T_{sol} given by Eq. (3.3) is therefore calculated using the pump peak power P_0, the input pulse temporal width T_0, and the second-order dispersion $\bar{\beta}_2$ [$\beta_2(\omega_{\mathrm{sol}}) = \bar{\beta}_2$ at $\omega_{\mathrm{sol}} = \omega_0$]. The result is shown in Fig. 3.2 (right), which shows the wavelengths λ_{DW} at which dispersive waves can be amplified, as a function of the soliton wavelength λ_{s}. From this figure it is expected that a soliton initially launched at $\lambda_0 = 804$ nm will amplify dispersive waves at ~ 600 nm in all the 5 fibres investigated in this section. Dispersive waves in the infrared are not expected to be amplified in the beginning of the fibre, because there is initially not enough spectral power from the soliton in the infrared [56].

Equation (3.3) gives the width of the shortest fundamental soliton, which was then used for Fig. 3.2 (right). It was calculated that the temporally longer fundamental solitons are phase-matched to amplify dispersive waves slightly closer to the soliton wavelength than the shortest soliton [1]. More importantly, the frequency shift per unit propagation length caused by SSFS is smaller, because it scales inversely with T_{sol} or T_{sol}^4, depending on the magnitude of T_{sol} [Eqs. (2.28) and (2.29)]. This makes the shortest fundamental soliton move quicker towards the higher ZDW and be the first to amplify dispersive waves. It is therefore more important for the generation of infrared dispersive waves than the longer solitons.

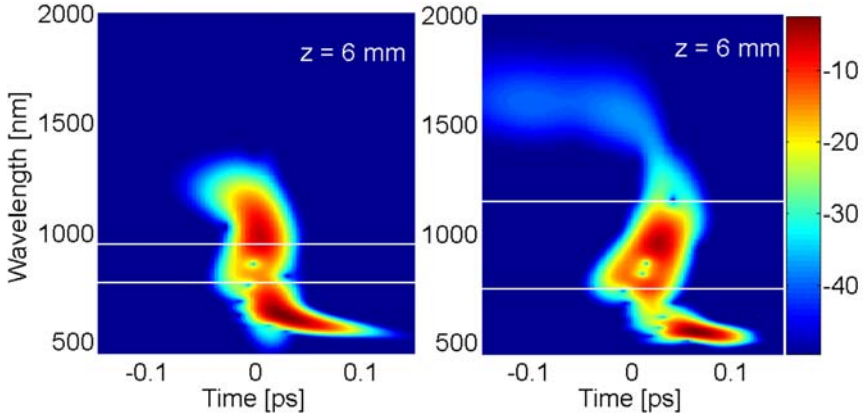

Figure 3.3: Calculated spectrograms up to $z = 6$ mm in the $\Lambda = 1.0$ µm (*left*) and the $\Lambda = 1.1$ µm (*right*) fibre. The white horizontal line indicates the ZDWs. 2^{10} computation points were used. Both animations can be downloaded online from Ref. [1].

Due to small differences in $A_{\text{eff}}(\omega_0)$ and $\bar{\beta}_2$, N varies from 3.8 to 3.3 for the $\Lambda = 1.1 - 1.4$ µm fibres. Compared to these fibres, $\bar{\beta}_2$ for the $\Lambda = 1.0$ µm fibre is ~ 4 times smaller numerically, giving $N = 8.2$.

In the $\Lambda = 1.0$ µm fibre, the anomalous dispersion region (ADR) is so narrow that the SPM rapidly moves most of the pulse energy into the NDR (Fig. 3.3, left) [1]. In the $\Lambda = 1.1$ µm fibre, the red-shifted peak remains in the ADR and can thus form a soliton. It is seen from Fig. 3.3 (right) that the soliton starts to amplify dispersive waves at 1600 nm at $z \sim 3$ mm. The dispersive wave wavelength of ∼1600 nm is correctly predicted from Fig. 3.2 (right). Note that the dispersive waves immediately spread temporally, as expected.

The power spectra after 6 mm and 6 cm of propagation in each of the 5 examined fibres are compared in Fig. 3.4. The dispersive wave generated at ∼1600 nm in the $\Lambda = 1.1$ µm fibre has too low power to be seen on the linear scale used in the figure. The comparison shows that in all of the 5 fibres there are two distinct peaks, a red-shifted and a blue-shifted, which arise from SPM, as described in Section 3.1. Except for the $\Lambda = 1.0$ µm fibre, in all cases the red-shifted peak is still in the ADR after 6 mm and is able to form solitons.

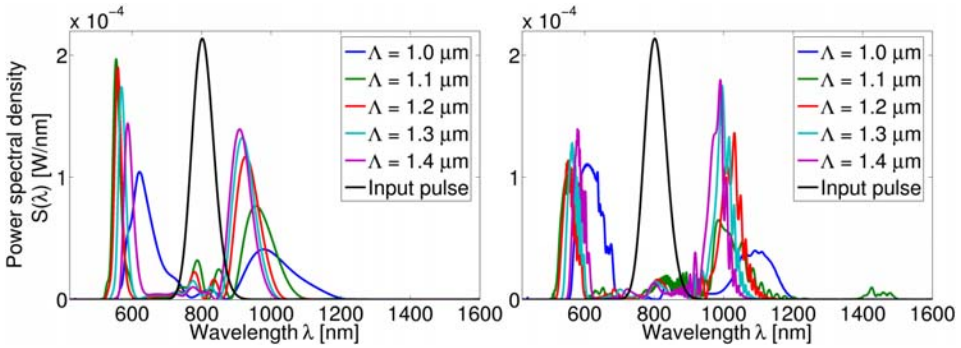

Figure 3.4: Power spectra after 6 mm (*left*) and 6 cm (*right*) of propagation. The input spectrum is indicated as a thin black line.

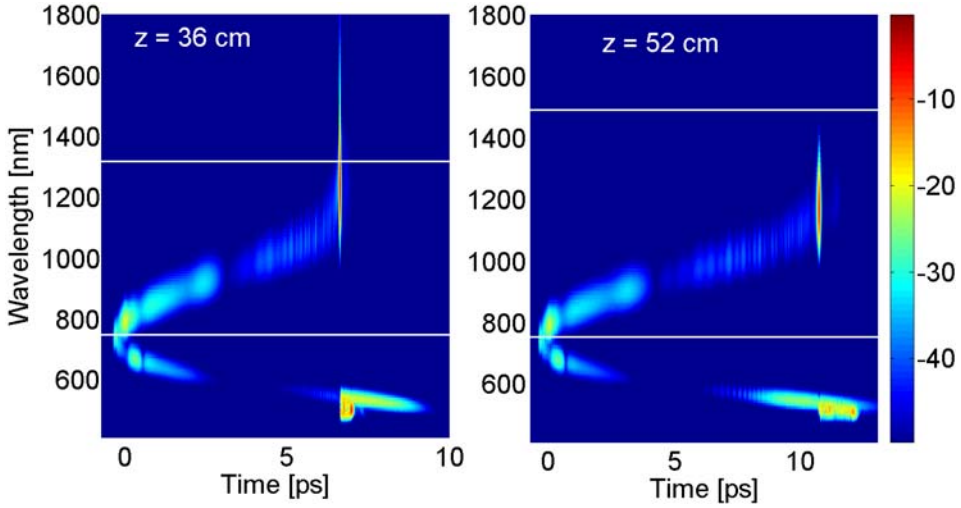

Figure 3.5: *Left:* Spectrogram for the 1.2 μm PCF up to $z = 60$ cm. *Right:* Spectrogram for the 1.3 μm PCF up to $z = 52$ cm. The white horizontal lines indicate the ZDWs. Both animations can be downloaded online from Ref. [1].

The solitons are gradually red-shifted by SSFS towards the higher ZDW. When a soliton has red-shifted to the vicinity of the higher ZDW it starts to amplify dispersive waves in the NDR [56]. As mentioned above, this occurs already after approximately 3 mm of propagation in the $\Lambda = 1.1$ μm fibre. For fibres with a larger pitch Λ, the soliton can propagate several centimeters before amplifying dispersive waves in the infrared. This happens at approximately $z = 35$ cm for the $\Lambda = 1.2$ μm fibre (Fig. 3.5, left). The spectral ripples in the dispersive waves at ∼600 nm can be explained by cross-phase modulation (XPM) between the soliton and the dispersive waves [81].

For the $\Lambda = 1.3$ μm fibre, the soliton has shifted to ∼1200 nm at $z = 52$ cm. Since this is still far from the higher ZDW, the soliton has not yet lost power to dispersive waves in the infrared (Fig. 3.5, right). Similarly, in the $\Lambda = 1.4$ μm fibre the soliton has shifted to ∼1170 nm at $z = 60$ cm without losing power to infrared dispersive waves. The main role of the higher ZDW for the cases investigated here can therefore be summarized as follows. For a fibre with closely lying ZDWs, pumping in the ADR causes SPM to move most of the power out of the ADR, and further broadening into the infrared is halted. For fibres with a larger separation between the ZDWs a soliton is formed, which gradually red-shifts along the fibre due to SSFS. The larger the higher ZDW is, the further into the infrared the soliton can red-shift without losing power to dispersive waves above the higher ZDW.

3.2.1 Wavelength-tunable soliton

An application of these fibres could, e.g., be the generation of femtosecond pulses in the infrared from an initial pulse at $\lambda = 804$ nm. It is further demonstrated in Fig. 3.6 that the SSFS can be used to produce femtosecond pulses with an almost Gaussian spectral shape. By choosing a suitable fibre length, the central wavelength of the Gaussian spectrum can be freely selected in the range ∼1020–1200 nm. The FWHM of each Gaussian spectrum is on the order of 30 nm. The use of the SSFS to generate wavelength-tunable soliton pulses has previously been demonstrated in tapered PCFs [82]. For comparison, in Ref. [82] a SSFS of 20% of the optical frequency ($\lambda = 1.3 \rightarrow 1.65$ μm) was experimentally demonstrated in a 15 cm long tapered fibre, where the present results correspond to a

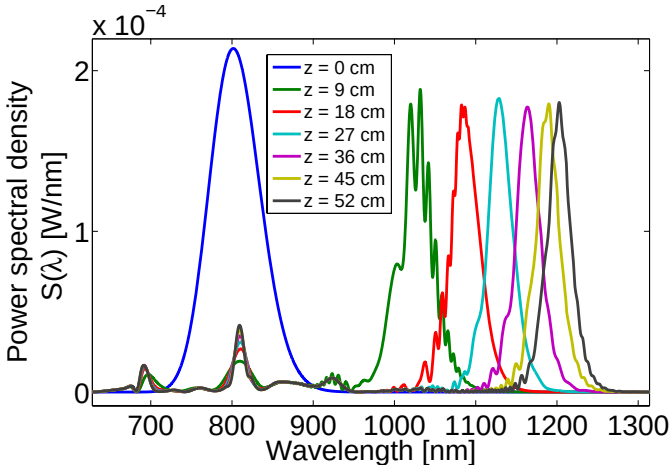

Figure 3.6: The red-infrared part of the pulse spectrum output from the $\Lambda = 1.3$ µm PCF at various fibre lengths.

SSFS of more than 30% in 52 cm of untapered fibre. SSFS in an untapered PCF has also been demonstrated experimentally by Reid *et al.* [83]. Quite similar to the simulated results in this work, Reid *et al.* pumped at 810 nm and obtained a maximum red-shift to 1260 nm. The wavelength tunability of the soliton was exploited recently by Andresen *et al.* for coherent anti-Raman Stokes (CARS) microspectroscopy [84]. In such experimental setups it is unpractical to tune the soliton wavelength by changing the fibre length. Instead, one can vary the fibre input power. Since the input peak power P_0 determines the width T_{sol} of the fundamental solitons [Eq. 3.3], and the red-shift rate depends inversely on T_{sol} or T_{sol}^4 (Subsection 2.2.4), the obtained red-shift can be tuned by varying P_0 for a fixed fibre length.

It is expected that for longer fibre lengths the solitons in the $\Lambda = 1.3$–1.4 µm PCFs will also continue to red-shift until they are in the vicinity of the higher ZDW, followed by an amplification of dispersive waves in the infrared. It should be noted, however, that fibre losses in the infrared region (OH-absorption and confinement loss) may ultimately limit the spectral extension into the infrared [56, 73].

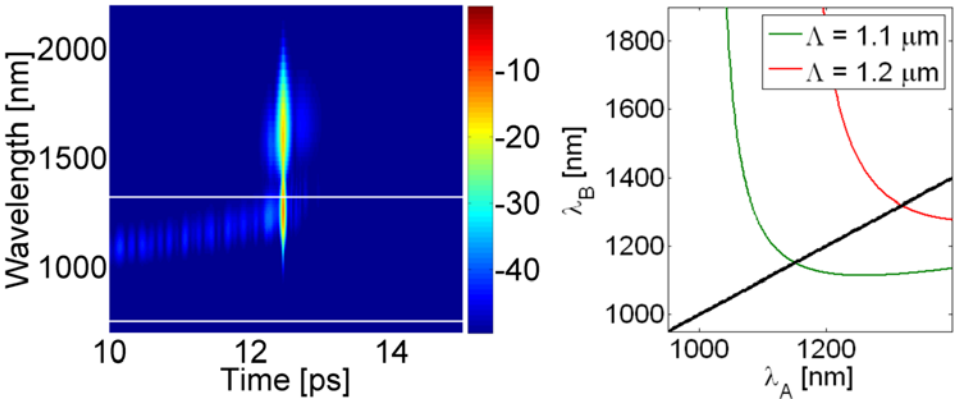

Figure 3.7: *Left:* A close-up of the spectrogram for the $\Lambda = 1.2$ μm PCF at $z = 60$ cm. It is seen that the pulse generated in the NDR has not changed its width significantly over several centimeters of propagation. The white horizontal lines indicate the ZDWs. *Right:* Wavelength λ_B at which there is group-velocity match to λ_A, according to Eq. (3.5). The black line indicates $\lambda_A = \lambda_B$.

3.3 Bright-bright soliton pair

It is noteworthy from Fig. 3.5 (left) that the pulse generated in the infrared NDR of the $\Lambda = 1.2$ μm fibre, does not immediately disperse (as was the case for the $\Lambda = 1.1$ μm fibre, see Fig. 3.3, right) but has retained its temporal width after several centimeters of propagation, as seen in Fig. 3.7 (left). The pulse is generated at ~ 1600 nm where $\beta_2 = 2 \times 10^{-25}$ s^2/m, and has an estimated temporal width (FWHM) of less than 50 fs. The dispersion length is thus [13] $L_D = T_0^2/|\beta_2| \approx 1$ cm. Since the temporal width of the radiation in the NDR is almost constant during 20 cm of propagation, it is clear that some nonlinear effects counter-act the dispersion. This is similar to the effect of SPM in the ADR, which allows solitons to exist (Subsection 2.2.2).

It was suggested by Frosz *et al.* that the pulse generated in the NDR forms a soliton-pair with the soliton in the ADR [1]. Soliton-pairs across the ZDW are known in the form of bright-dark and bright-gray soliton pairs made possible by XPM between the solitons [13]. However, in the case at hand a bright-bright soliton pair across the ZDW is apparently formed, which was

not described before the work of Frosz *et al.* [1], to the best of the author's knowledge. The co-propagation of a sech-pulse in the NDR with a sech-pulse in the ADR was investigated in Ref. [85], but only the propagation of the pulse in the ADR was considered, and the influence of the ADR-pulse on the NDR-pulse was neglected. A bright-bright soliton pair can be formed within the *same* dispersion region [86], but XPM alone cannot allow a bright-bright soliton pair across the ZDW. It is therefore expected that the Raman effect also plays a role in this new observation.

It is known that a region of modulation instability (MI) can exist near the ZDW in the NDR, and that this MI can possibly allow bright solitons to form in the NDR [87]. One requirement for the MI region to exist at the angular frequency ω is $\beta_2(\omega) + \beta_4(\omega)\Omega^2/12 < 0$ [88], where Ω is defined as in Eq.(2.27). Near the higher ZDW of the $\Lambda = 1.2$ μm fibre we have $\beta_4(\omega) > 0$, so there does not exist an MI region in the NDR ($\beta_2 > 0$), and this can therefore not explain the apparent soliton formation in the NDR.

Since one part of the soliton pair is formed in the NDR with higher wavelength than the ADR, the red-shift of the soliton in the ADR is halted due to spectral recoil from the higher ZDW [89, 90]. The "soliton" in the NDR therefore does not have to continuously shift its wavelength to match the group-velocity of the soliton in the ADR; if the NDR-pulse had a lower wavelength than the ADR-pulse the two pulses would separate spectrally, due to SSFS of the ADR-pulse and spectral recoil from the lower ZDW. Instead, the result is a spectrally stable soliton pair. The condition of group-velocity matching for the soliton-pair is examined analytically in the following subsection.

3.3.1 Group-velocity matching

In this subsection an equation describing the condition for group-velocity matching is derived. This is a necessary condition if radiation initially formed from amplification of dispersive waves in the NDR, leads to the formation of a soliton-pair consisting of a soliton in the ADR (at $\lambda = \lambda_A$) co-propagating with a "soliton" in the NDR (at $\lambda = \lambda_B$).

A necessary condition for the two pulses to be co-propagating is that the group-velocity v_g is matched, i.e. $1/v_g = \beta_1(\omega_A) = \beta_1(\omega_B)$. From the

definition of $\beta(\omega)$ [Eq. (2.4)] one has,

$$\beta_1(\omega) = \beta_1(\omega_A) + \beta_2(\omega_A)[\omega - \omega_\mathrm{A}] + \frac{\beta_3(\omega_A)}{2}[\omega - \omega_\mathrm{A}]^2, \tag{3.4}$$

where $\beta_m(\omega)$ is given by Eq. (2.5) and we only include up to $\beta_3(\omega_A)$. The condition $\beta_1(\omega_\mathrm{A}) = \beta_1(\omega_\mathrm{B})$ then gives

$$\Delta\omega = -\frac{2\beta_2(\omega_A)}{\beta_3(\omega_A)}, \tag{3.5}$$

where $\Delta\omega = \omega_B - \omega_A$. From Eq. (3.5) λ_B is plotted as a function of λ_A for the dispersion profiles belonging to the fibres with $\Lambda = 1.1$ μm and $\Lambda = 1.2$ μm in Fig. 3.7 (right). From Figs. 3.3 (right) and 3.4 (right), we know that the SSFS is cancelled for the soliton in the $\Lambda = 1.1$ μm fibre when the soliton wavelength reaches ~ 1000 nm. It is seen in Fig. 3.7 (right), that for $\lambda_A = 1000$ nm there is no group-velocity match in the vicinity of λ_A. Since the amplification of dispersive waves transfers energy to ~ 1600 nm, a soliton-pair cannot be formed. On the other hand, for the $\Lambda = 1.2$ μm fibre, it is known from Figs. 3.5 (left) and 3.7 (left) that the soliton is red-shifted to ~ 1250 nm before cancellation of SSFS. According to Fig. 3.7 (right) at $\lambda_A = 1250$ nm there is group-velocity match to $\lambda_B \sim 1500$ nm. The ADR-pulse can therefore match its group-velocity to the NDR-pulse formed by the transfer of energy to ~ 1600 nm. As observed in Figs. 3.5 (left) and 3.7 (left), this leads to the formation of what appears to be a bright-bright soliton pair across the higher ZDW.

The structure of the apparent soliton-pair is shown in greater detail in Fig. 3.8 using spectrograms with logarithmic and linear scales. Recently, work has been initiated to analytically investigate and understand the apparent soliton-pair [91].

3.4 Tapered photonic crystal fibres

As mentioned in Subsection 2.3.1 an advantage of using PCFs for supercontinuum generation is the small core size that can be obtained, thus resulting in a high nonlinear parameter. A small core size can also be obtained in standard fibres, if the fibre is *tapered* by heating and stretching it. The standard fibre can then be used for SCG by pumping with femtosecond pulses

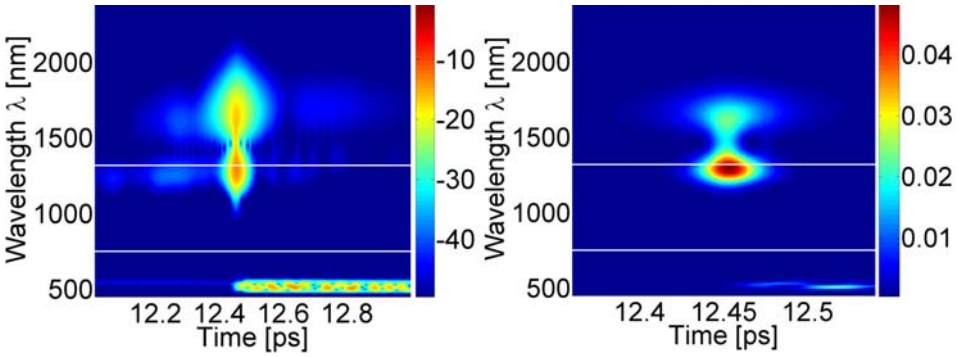

Figure 3.8: Spectrograms on a logarithmic (left) and linear (right) scale at $z = 60$ cm for the $\Lambda = 1.2$ µm fibre. As seen from the colour bar, the colour scale for the linear scale spectrogram is *not* normalized to $S(0, 0, \omega_0) = 1$, as the other spectrograms, because this does not result in a spectrogram with notable details. The white horizontal lines indicate the ZDWs.

[54]. Tapering is mostly relevant for femtosecond pumping because fibres can typically be tapered up to a length of only $\sim$ 10–15 cm [92] and, as will be seen in the following chapters, pumping with picosecond or longer pulses requires longer fibre lengths for efficient spectral broadening.

A PCF can be tapered to achieve an even smaller core than in an untapered PCF, thereby reducing the required fibre length for efficient nonlinear effects [82]. The tapering procedure can also be used to engineer the dispersion properties of a PCF so that the phase-matching conditions are modified to, e.g., generate dispersive waves in the blue part of the spectrum [93]. A recent review of tapered PCF fabrication, characterization, applications, and properties can be found in Ref. [94].

Falk *et al.* were the first to investigate the possibilities for shaping the SC spectrum by varying the tapering parameters of a tapered triangular structured PCF over a wide parameter space [2, 5]. This work is described in the following.

3.4.1 Modelling of tapered fibres

The fibre with parameters $\Lambda = 1.0$ µm and $d/\Lambda = 0.57$ investigated in Sections 3.1–3.2 is also the basis of the study in this section. It is assumed

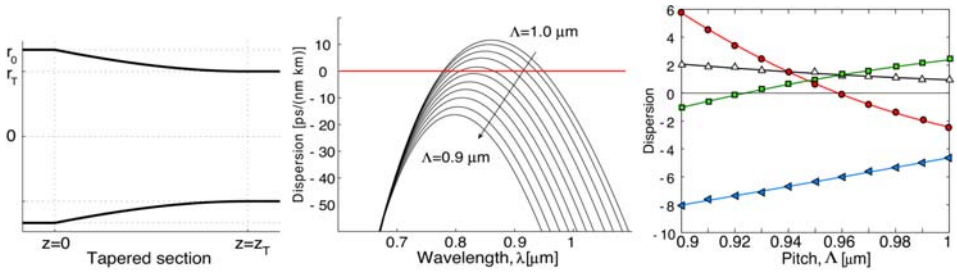

Figure 3.9: *Left:* A sketch of the tapered PCF along the fibre length z. r_0 is the radius of the untapered PCF and r_T is the radius of the PCF at the taper waist. z_T is the distance from the start of the tapering to the waist. *Middle:* Dispersion profiles for PCFs with pitch Λ varying from 1.0 μm to 0.9 μm and constant relative hole size $d/\Lambda = 0.57$. *Right:* Dispersion coefficients β_2, ..., β_5 for the 10 dispersion profiles in the middle figure, plotted with fitted second-order polynomials as a function of Λ. β_2 [10^{-27} s^2/m] (red, ○), β_3 [10^{-41} s^3/m] (green, □), β_4 [10^{-55} s^4/m] (black, △), and β_5 [10^{-70} s^5/m] (blue, ◁).

that the relative hole size d/Λ is constant along the tapering [2]. This assumption seems reasonable if the PCF is tapered "fast-and-cold" [94, 95]. It is also assumed that the variation of the pitch $\Lambda(z)$ along the taper is described by [2]

$$\Lambda(z) = \Lambda_\mathrm{T}\left[1 + \frac{\Lambda_0^2 - \Lambda_\mathrm{T}^2}{\Lambda_\mathrm{T}^2}\frac{(z - z_\mathrm{T})^2}{z_\mathrm{T}^2}\right]^{1/2}, \qquad z \geq 0, \tag{3.6}$$

where the border between untapered fibre and tapering region is at $z = 0$, $\Lambda_0 = \Lambda(0)$ is the pitch of the untapered fibre, $\Lambda_\mathrm{T} = \Lambda(z_\mathrm{T})$ is the pitch at the tapering waist, and z_T is the length from the start of the tapering to the tapering waist. The diameter of the tapered PCF is proportional to $\Lambda(z)$; the tapering shape resulting from Eq. (3.6) is shown in Fig. 3.9 (left). This taper shape should be realizable, since the shape of the tapering can be controlled during the tapering [96].

The propagation in the tapering is modelled using Eq. (2.2), where the $\bar{\beta}_m$-coefficients now have a z-dependence: $\bar{\beta}_m(z)$. In the split-step code, this is implemented by dividing the tapering region $0 \leq z \leq z_\mathrm{T}$ into 100 sub-regions, $z_1, z_2, \ldots, z_{100}$. Every time the pulse moves into a new sub-region

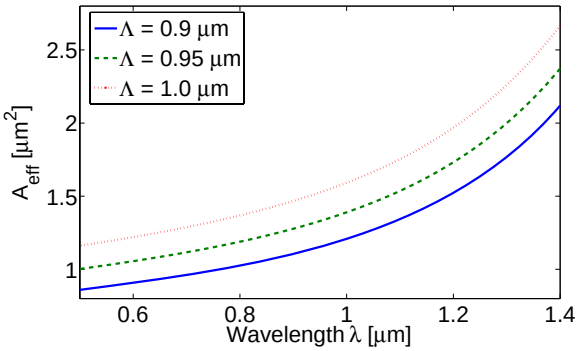

Figure 3.10: The effective area A_{eff} as a function of wavelength for a pitch size Λ ranging from 1.0 to 0.9 µm. The relative hole size $d/\Lambda = 0.57$ for all fibres.

z_s, the $\bar{\beta}_m$ coefficients are updated to $\bar{\beta}_m(z_s)$. In Ref. [2] the minimum tapered pitch Λ_{T} was 0.9 µm, corresponding to a 10% tapering. Instead of calculating dispersion profiles for all the 100 subregions, 11 dispersion profiles were calculated for $\Lambda = 1.0$ µm, 0.99 µm, 0.98 µm, ..., 0.9 µm, shown in Fig. 3.9 (middle). The dispersion coefficients $\bar{\beta}_{2\text{–}15}$ were then extracted from a polynomial fit for each of the 11 dispersion profiles. It was found that the variation of the dispersion coefficients with the pitch Λ could be well-approximated by a second-order polynomial, as shown in Fig. 3.9 (right). Thus, second-order polynomials for $\bar{\beta}_2(\Lambda), \bar{\beta}_3(\Lambda), \ldots, \bar{\beta}_{15}(\Lambda)$ were obtained and could be used to calculate the $\bar{\beta}_m$-coefficients in each of the 100 subregions.

$A_{\text{eff}}(\lambda)$ is shown for three different values of Λ in Fig. 3.10. At $\lambda = 800$ nm, $A_{\text{eff}} \approx 1.37$ µm^2 for the $\Lambda = 1.0$ µm fibre, and $A_{\text{eff}} \approx 1.03$ µm^2 when tapered to $\Lambda = 0.9$ µm. The variation of $A_{\text{eff}}(\lambda)$ along the tapering is thus less than 25% and was neglected in Ref. [2], but can be included [97].

3.4.2 Spectral shaping by tapering

The present work has focused on pumping the tapered fibre directly at the border between untapered and tapered fibre, corresponding to $z = 0$ in Eq. (3.6). As mentioned in the previous subsection, the untapered fibre parameters correspond to one of the fibres investigated in both Sections 3.1–

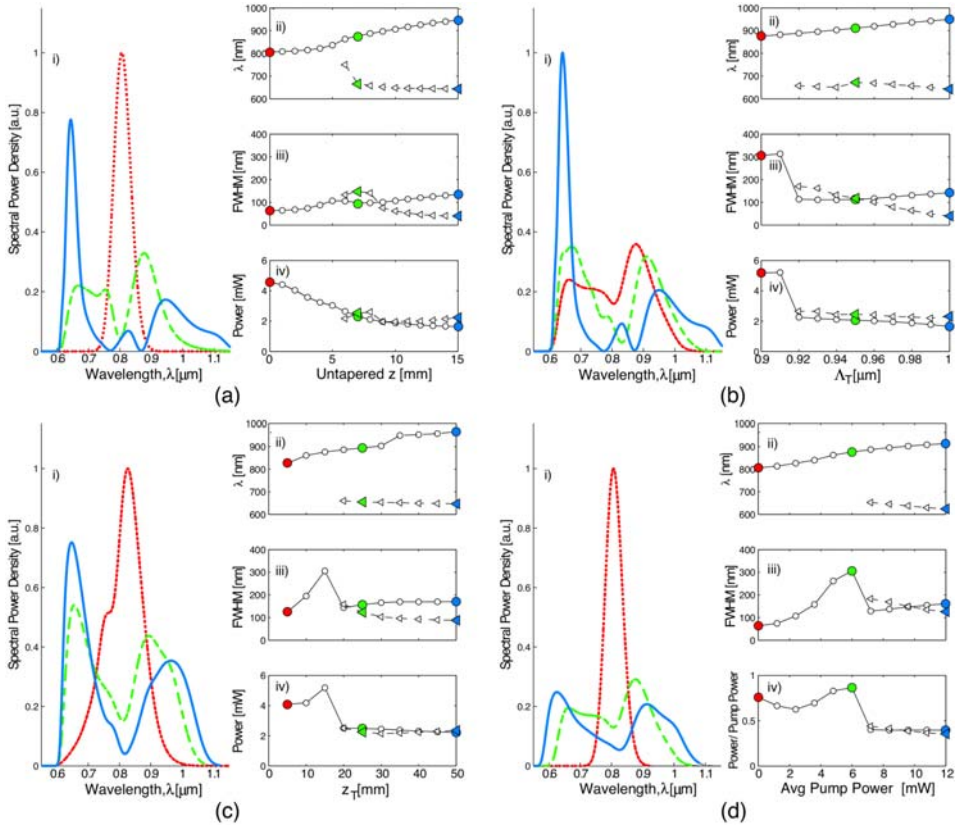

Figure 3.11: (**a**, i) Power spectra for an untapered PCF ($\Lambda = 1.0$ μm) at $z = 0$ mm (dotted, red), $z = 8$ mm (dashed, green), and $z = 15$ mm (solid, blue). (**b**, i) Power spectra at $z = z_T = 15$ mm for $\Lambda_T = 0.9$ μm (dotted, red), $\Lambda_T = 0.95$ μm (dashed, green), and $\Lambda_T = 1.0$ μm (solid, blue). (**c**, i) Power spectra for $\Lambda_T = 0.9$ μm at taper waist $z = z_T$, for $z_T = 15$ mm (dotted, red), $z_T = 25$ mm (dashed, green), and $z_T = 50$ mm (solid, blue). (**d**, i) Power spectra at taper waist $z = z_T$, $\Lambda_T = 0.9$ μm, and average power $P_{av} = 6$ μW (dotted, red), 6 mW (dashed, green), and 12 mW (solid, blue). (**a-d**, ii) Centre wavelengths λ, (**a-d**, iii) power spectral FWHM, and (**a-d**, iv) average power within the FWHM of the red-shifted (○) and blue-shifted (◁) peaks, versus the parameters z (i), Λ_T (ii), z_T (iii), and P_{av} (iv). Pump parameters: $\lambda_0 = 808$ nm, $T_{FWHM} = 15$ fs, $f_{rep} = 75$ MHz, and $P_0 = 5$ kW [except for Subfig. (**d**) where the power is varied]. $d/\Lambda = 0.57$ along all taperings.

3.2. The input pulses used are also very similar: Gaussian shape, $\lambda_0 = 808$ nm, $T_{\mathrm{FWHM}} = 15$ fs, $f_{\mathrm{rep}} = 75$ MHz, and $P_0 = 5$ kW. The average input power is thus 6 mW, except when the peak power is changed to vary the average input power. The spectral evolution along the untapered fibre is similar to that presented in Sections 3.1–3.2, which was dominated by SPM over the first millimeters of propagation, and is shown in Fig. 3.11 (**a**, i). Figure 3.11 (**a**, ii) shows the central wavelengths of the red-shifted and the blue-shifted peaks along the fibre length z. Figure 3.11 (**a**, iii) shows the corresponding power spectral FWHM of the peaks, and Fig. 3.11 (**a**, iv) shows the average power within the FWHM of the peaks [2].

As seen from Fig. 3.9 (middle) tapering the fibre decreases the dispersion D along the taper, until it becomes normally dispersive for all optical wavelengths when $\Lambda \lessapprox 0.96$ μm. In the normal dispersion regime SPM and GVD act together to temporally broaden the pulse faster than in the anomalous dispersion regime, as noted in Section 3.1, which halts the SPM induced spectral broadening. Tapering the fibre can therefore be used to shape the resulting spectrum.

For SCG in an untapered fibre one can alter the resulting spectrum by changing the fibre length, pump pulse parameters, and the PCF structural parameters, e.g. the pitch Λ and the relative hole size d/Λ for a triangularly structured PCF. Tapering the PCF provides additional adjustable parameters, namely the tapering length, expressed here by z_{T}, and the degree of tapering, expressed here by Λ_{T}. Fig. 3.11 (**b**) shows how the spectrum can be modified by varying Λ_{T} for a fixed value of z_{T}. Fig. 3.11 (**c**) shows the same for different values of z_{T} for a fixed value of Λ_{T}. Finally, Fig. 3.11 (**d**) shows the effect of varying the input power for a fixed tapering structure.

It is seen that tapering the PCF can flatten the resulting spectrum significantly. For example, for $z_{\mathrm{T}} = 15$ mm, $\Lambda_{\mathrm{T}} = 0.9$ μm, and $P_{\mathrm{av}} = 6$ mW [Fig. 3.11 (**b**–**d**, iii)], the FWHM of the spectrum is ~ 300 nm. For comparison, the largest FWHM in the untapered PCF is ~ 150 nm at $z = 7$ mm [Fig. 3.11 (**a**, iii)]. This is mostly because the spectral dip at $\lambda \approx 800$ nm for the untapered fibre [Fig. 3.11 (**a**, i), dashed, green] is avoided when tapering the PCF [e.g. Fig. 3.11 (**d**, i), dashed, green].

Apart from flattening the spectrum, tapering can also be used to obtain some control over the two peaks seen in Fig. 3.11; their centre wavelengths, FWHM, and power depends on the tapering parameters. A spectrum with

two peaks is useful for differential absorption OCT [98] or can be used to make OCT images in two wavelength ranges simultaneously [74].

The work by Falk *et al.* thus demonstrated that tapering provides additional adjustable parameters to control the SCG [2].

Chapter 4

Picosecond pumping

It is well-known that supercontinuum generation (SCG) using femtosecond pulses is typically (see, e.g., Chapter 3 or Refs. [1, 20, 56]) mainly caused by self-phase modulation (SPM), fission of higher-order solitons followed by soliton self-frequency shift (SSFS), and amplification of dispersive waves. Since femtosecond pump lasers are typically complex systems, it is of great interest to study efficient SCG using longer pulses, such as picoseconds or even nanoseconds, which can be produced by simpler lasers [20, 61]. For picosecond pulse pumping, SPM is typically less dominant since the SPM spectral broadening is inversely proportional to the temporal width of the input pulse [13]. Instead, it is known that the spectral broadening is mainly caused by four-wave mixing (FWM) and stimulated Raman scattering [21, 61, 99, 100]. As will be shown in Section 4.2, FWM is also the dominant supercontinuum (SC) mechanism in the cases investigated in this chapter.

Nikolov *et al.* showed that a SC pumped by low-average power picosecond pulses could be generated more efficiently using proper dispersion design [21]. It was found that the spectrum becomes more flat if the dispersion profile ensures that the Stokes and anti-Stokes bands generated by partially degenerate FWM are sufficiently close to the pump, so that they can broaden themselves and merge with the pump into a flat continuum before losses and temporal splitting decreases the peak power to a level where nonlinear effects are no longer efficient. Furthermore, calculations showed that a broad FWM gain bandwidth makes the SCG more robust against random variations of the photonic crystal fibre (PCF) structure along the fibre length [21]. These

calculations were based on experimental measurements of the dispersion profile variation over a 150 m fibre span [101]. This means that fabrication tolerances can be expected to be less stringent for fibres designed so that the FWM gain bandwidth is broad.

It is demonstrated here how the dispersion profile of a cobweb PCF can be engineered by modifying the fibre structural parameters and to what extent this influences the SC spectrum. The investigation by Nikolov *et al.* [21] only considered dispersion profiles for a few particular PCF designs. In subsequent work by Frosz *et al.* a detailed numerical study was made of how the dispersion parameters vary as a function of the cobweb PCF core size and wall thickness [3, 7]. This included an analysis showing how and why the maximum FWM bandwidth is obtained. It was investigated how control of the core size and wall thickness can be used to modify the position of the Stokes and anti-Stokes bands, the FWM gain bandwidth, and how these FWM properties are affected by the Raman effect. It is thereby possible to shape the SC spectrum and it was examined whether there is an optimum core size and wall thickness. Shifting the Stokes/anti-Stokes bands away from the pump increases the spectral width, but can introduce dips in the spectrum. It was therefore also investigated how far away from the pump the Stokes/anti-Stokes bands can be moved before introducing dips in the spectrum.

The theory of FWM was presented in Subsection 2.2.3. It was shown how the wavelengths of the amplified spectral components are determined by the phase matching condition Eq. (2.27), which is determined by the dispersion coefficients. It is therefore clear that the dispersion profile of a fibre is of utmost importance for the resulting SC spectrum.

4.1 Four-wave mixing parameters

Several dispersion curves were calculated for varying core size d_{core} and wall thickness w in the cobweb PCF structure [3, 7], using a semi-vectorial finite-difference method [59, 60]. The calculation time for each fibre structure was approximately 12–24 hours on a PC with a 2.9 GHz processor and 4.5 Gbytes RAM. Examples of three different dispersion profiles are given in Fig. 4.1, for fixed pitch $\Lambda = 8.53$ μm and wall thickness $w = 130$ nm.

As described in Subsection 2.3.2, the dispersion coefficients are obtained

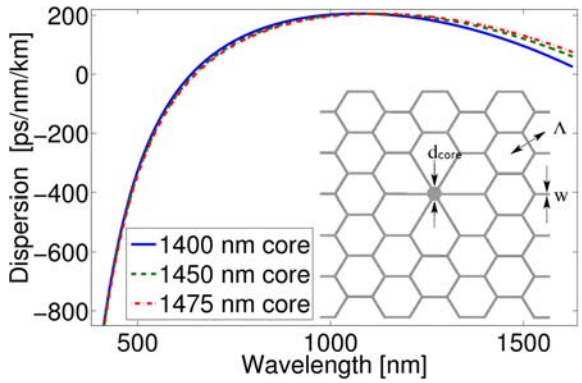

Figure 4.1: Examples of three dispersion curves, calculated for a cobweb structure (see inset) with wall thickness $w = 130$ nm, pitch $\Lambda = 8.53$ µm, and core size d_{core} ranging from 1400 to 1475 nm.

by fitting the calculated dispersion profiles to polynomials. Dispersion coefficients up to and including $\bar{\beta}_{14}$ were used.

The obtained dispersion coefficients were used to calculated the phase mismatch κ [Eq. 2.27] and the gain g [Eq. 2.26] for three different core sizes, as shown in Fig. 4.2. For the three selected fibre designs one has $\bar{\beta}_2 < 0$, $\bar{\beta}_2 \approx 0$, and $\bar{\beta}_2 > 0$, for the $d_{\text{core}} = 1400$ nm, 1450 nm, and 1475 nm fibres, respectively. For the $d_{\text{core}} = 1400$ nm fibre, the Stokes gain bandwidth is $\lambda_{\text{d}} - \lambda_{\text{p}}$, and the anti-Stokes gain bandwidth is $\lambda_{\text{p}} - \lambda_{\text{c}}$ (see Fig. 4.2). The Stokes gain region is thus directly connected to the anti-Stokes gain region at λ_{p}. When $\bar{\beta}_2$ is increased to almost zero, as for the $d_{\text{core}} = 1450$ nm core fibre, the Stokes and anti-Stokes peaks (the wavelengths for which the gain g is maximum, at $\kappa = 0$) shift away from the pump and their gain bandwidths increase. However, as soon as $\bar{\beta}_2$ becomes positive, as for the $d_{\text{core}} = 1475$ nm core fibre, the Stokes and anti-Stokes bands separate and their gain bandwidths decrease. In Fig. 4.2 the anti-Stokes gain bandwidth in this case is $\lambda_{\text{a}} - \lambda_{\text{b}}$ and there is no energy transfer to wavelengths between λ_{a} and λ_{p} from partially degenerate FWM. Similarly, the Stokes band will be separated from the pump by a region without gain. From Fig. 4.2 we therefore expect that PCFs where $\bar{\beta}_2$ is positive will lead to Stokes and anti-Stokes spectral bands far from the pump, but possibly with a discontinuity between the pump and the Stokes/anti-Stokes spectral bands. As shown in

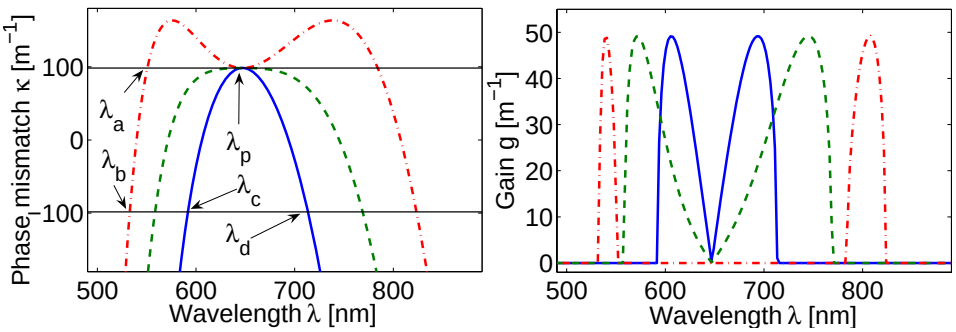

Figure 4.2: *Left:* Phase mismatch κ for cobweb PCFs with $\Lambda = 8.53$ µm, $w = 130$ nm, and $d_{\text{core}} = 1400$ nm (solid, blue), $d_{\text{core}} = 1450$ nm (dashed, green), and $d_{\text{core}} = 1475$ nm (dashed-dotted, red); the pump wavelength is 647 nm, $\gamma = 0.15$ $(\text{Wm})^{-1}$ (the slight variation of γ with core size is neglected in this figure), and $P_0 = 400$ W. The upper and lower horizontal lines at $\kappa = \pm 2\gamma P_0(1 - f_{\text{R}}) = \pm 98.4$ m^{-1} indicate the borders of the gain region. For $d = 1400$ nm, $\bar{\beta}_2 < 0$; for $d = 1450$ nm, $\bar{\beta}_2 \approx 0$; and for $d = 1475$ nm, $\bar{\beta}_2 > 0$. *Right:* Corresponding parametric gain given by Eq. (2.26).

Section 4.2 this can occur if the fibre is too short. On the other hand, for fibres with a small but negative $\bar{\beta}_2$, there is FWM gain for a broad continuous range of wavelengths from the pump to the immediately adjacent Stokes and anti-Stokes gain regions. This should therefore result in a smoother spectrum.

It is usually recommended to pump in the anomalous dispersion regime, close to the zero-dispersion wavelength (ZDW) (corresponding to a small, negative $\bar{\beta}_2$), to obtain phase matching for FWM [13]. In the cases presented here, it is noted that since $\bar{\beta}_4 < 0$ (shown below), phase-matching can also occur when pumping in the normal dispersion regime. However, an advantage of anomalous pumping is still expected, because it is known from Fig. 4.2 that this should result in a smoother spectrum.

As shown in Fig. 4.3, it was found that $\bar{\beta}_2$ can be significantly modified by varying the core size d_{core} and/or the wall thickness w. It was also found that the fourth-order dispersion parameter $\bar{\beta}_4$ is almost constant at around -4×10^{-5} ps^4/km when varying d_{core} and w within the parameter space investigated here. As seen from Eq. (2.27), a nonzero $\bar{\beta}_4$ is therefore expected to limit the FWM gain bandwidth when $\bar{\beta}_2 = 0$.

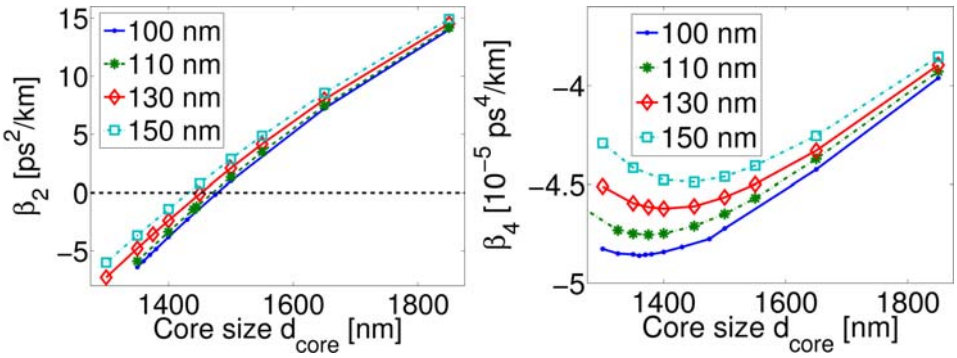

Figure 4.3: Dispersion parameters $\bar{\beta}_2$ (*left*) and $\bar{\beta}_4$ (*right*) calculated for a wide range of two of the cobweb-fibre structural parameters: core size d_{core} (horizontal axis) and wall thickness w (given in the inset).

The important thing to note from Fig. 4.3 is that although one cannot obtain a dispersion profile with zero curvature ($\bar{\beta}_4 \approx 0$, note that the slope of the dispersion profile, $\bar{\beta}_3$, is unimportant for the phase-matching condition) within the parameter range investigated here, it is still possible to tune $\bar{\beta}_2$ in the range -5 to 15 ps^2/km through selection of core size and/or wall thickness. This means that the phase mismatch plot can be significantly changed, as indicated in Fig. 4.2, and thereby the wavelength range at which new frequencies are generated can be controlled. The Stokes and anti-Stokes gain bandwidths are plotted for various fibre designs in Fig. 4.4, and defined in Fig. 4.2 as the regions where $|\kappa| < 2\gamma P_0(1 - f_{\text{R}})$. The anti-Stokes gain bandwidth in Fig. 4.2, e.g., is $\lambda_{\text{a}} - \lambda_{\text{b}}$ for the $d = 1475$ nm fibre, and $\lambda_{\text{p}} - \lambda_{\text{c}}$ for the $d = 1400$ nm fibre.

It is seen from Fig. 4.4 how the Stokes and anti-Stokes gain bandwidths increase as the core size is increased, until dropping rapidly after the core size where $\bar{\beta}_2 = 0$ (indicated by the vertical lines). This is understood graphically from Fig. 4.2, by noting the behavior of the phase mismatch plot when $\bar{\beta}_2$ goes from below to above zero.

The Stokes and anti-Stokes wavelengths for several fibre designs are plotted in Fig. 4.5. The Stokes and anti-Stokes wavelengths are the wavelengths at which $\kappa = 0$ and there is therefore maximum gain at these wavelengths, see Eq. (2.26). It is seen that the more the core size and/or the wall thick-

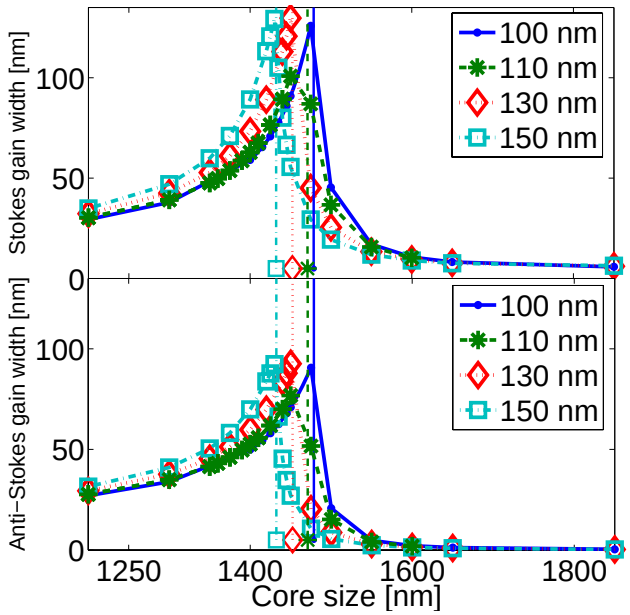

Figure 4.4: Stokes (*top*) and anti-Stokes (*bottom*) gain bandwidths as a function of core size d_{core} (horizontal axis) and wall thickness w (given in the inset). The vertical lines indicate the core size at which $\bar{\beta}_2 = 0$ for the various wall thicknesses.

ness is increased, the further away the Stokes and anti-Stokes lines shift from the pump. However, it is known from Fig. 4.4 that the gain bandwidth becomes narrow when the core size and wall thickness is large enough for $\bar{\beta}_2$ to become positive. As seen in Section 4.2, a small gain bandwidth leads to spectral dips in the SC. There is therefore a tradeoff between the flatness and the width of the SC spectrum [3, 7]. Furthermore, the SCG is less robust to PCF structural variations (e.g. core size and wall thickness) along the fibre length if the gain bandwidth is small [21].

4.2 Calculated spectra

To investigate how the FWM properties discussed in Section 4.1 affect the resulting SC spectrum, pulse propagation in various fibre designs was sim-

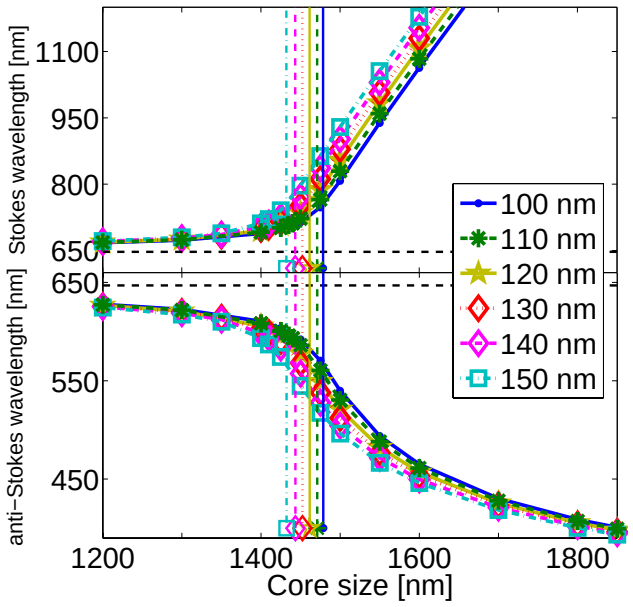

Figure 4.5: The Stokes (*top*) and anti-Stokes (*bottom*) wavelengths for various values of the core size d_{core} (horizontal axis) and the wall thickness w (given in the inset). The vertical lines indicate the core size at which $\bar{\beta}_2 = 0$ for the various wall thicknesses. The dashed horizontal lines indicates the pump wavelength.

ulated using Eq. (2.2). The frequency dependence of A_{eff} is small and therefore neglected; it was approximated with the core area, $A_{\text{eff}} \approx A_{\text{core}} = \pi[d_{\text{core}}/2]^2$. The attenuation coefficient α was also assumed to be wavelength independent and set to 300 dB/km, which is realistic for a cobweb fibre with the core sizes modelled here [57]. The simulations were done using 2^{17} points and a temporal resolution of $\Delta t = 1.8$ fs, giving a time window of $T_{\text{max}} = 236$ ps. The local goal error used in the adaptive step size method was set to $\delta_{\text{G}} = 10^{-7}$. This resulted in a step size of typically 1–4 μm. The calculations were first performed without loss. The relative change in the total photon number P was less than 2.5%. The calculations were then repeated, but included the 300 dB/km wavelength independent loss. The simulation time for propagation in 1.2 m of fibre varied between 11 days ($d_{\text{core}} = 1425$ nm, $w = 130$ nm) and 31 days ($d_{\text{core}} = 1475$ nm,

$w = 130$ nm) on a 2.2 GHz standard PC. The simulation time depends on the structural parameters because modulation instability (MI)/FWM leads to temporal fluctuations in the time domain of the pulse (Subsection 2.2.3). The further away the Stokes and anti-Stokes bands are located from the pump, the faster the temporal fluctuations [13]. The faster the pulse fluctuates in the time domain, the shorter the step size has to be so as to keep the numerical error of each step below the local goal error. This is done automatically by the adaptive step-size method.

The pump pulse parameters are: centre wavelength $\lambda_0 = 647$ nm, power full width at half-maximum (FWHM) $T_{\mathrm{FWHM}} = 30$ ps, and peak power $P_0 = 400$ W. As in Chapter 3 the power spectral densities $S(\lambda)$ presented here are normalized so that $\int S(\lambda)\mathrm{d}\lambda = P_{\mathrm{av}}$, where the average power is calculated from a repetition rate $f_{\mathrm{rep}} = 590$ kHz [see Eq. (A.6)]. Similar pump parameters were used in the theoretical investigation by Nikolov *et al.* [21] and in the experiments by Coen *et al.* [61], so these are physically realistic parameters.

The spectra presented in this section have been smoothed over 128 points, resulting in a frequency resolution of $\Delta\nu = 128/T_{\max} \approx 0.5$ THz, corresponding to approximately 0.8 nm in the vicinity of the pump wavelength 647 nm.

Figure 4.6 shows the evolution of the calculated spectra along the fibre length for two different core sizes. It is clearly seen how a larger core size results in Stokes and anti-Stokes bands further away from the pump. Furthermore, the location of the Stokes and anti-Stokes bands is seen to agree excellently with Fig. 4.5 and the gain bands indicated in Fig. 4.6. It is also noted that for a core size of $d_{\mathrm{core}} = 1425$ nm, the Stokes and anti-Stokes bands are already merged with the pump at $z = 0.9$ m, and a smooth broad continuum is formed. For a core size of $d_{\mathrm{core}} = 1475$ nm, the merging is first observed at $z = 1.2$ m. Even at this fibre length, the merging has not been as efficient as for the smaller core, and therefore spectral dips occur between the pump and the Stokes and anti-Stokes bands. It is possible that further propagation in a longer fibre would lead to further merging and a decrease of the spectral dips, but this was not investigated since the simulations are quite time-consuming. Furthermore, the bandwidth of the spectrum continuously increases along the fibre, and the propagation Eq. (2.2) can only be assumed valid for forward-travelling waves with a bandwidth less than

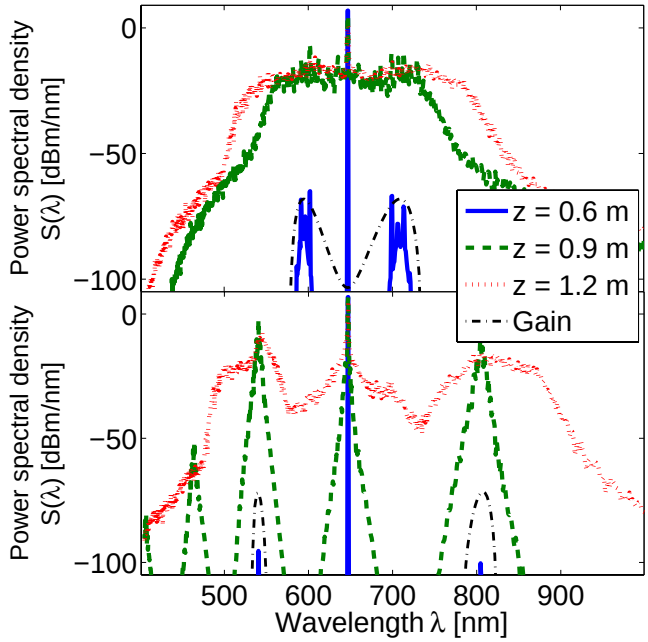

Figure 4.6: Calculated spectra for $d_{\text{core}} = 1425$ nm (top) and 1475 nm (bottom) at fibre lengths $z = 0.6$ m (solid, blue), $z = 0.9$ m (dashed, green), and $z = 1.2$ m (dotted, red). Wall thickness $w = 130$ nm. The parametric gain g is included (dashed-dotted, black) in arbitrary units to show how well the locations of the Stokes and anti-Stokes bands are predicted.

$\approx 1/3$ of $\nu_0 = c/\lambda_0$ [33]. A frequency bandwidth of $\Delta\nu = \nu_0/3$ corresponds to a wavelength bandwidth of $\Delta\lambda \approx c\Delta\nu/\nu_0^2 = \lambda_0/3 = 647$ nm$/3 \approx 216$ nm. There should therefore not be significant spectral power outside the wavelength range ≈ 539–755 nm. The simulations have already reached this limit after 1.2 m of propagation.

Figure 4.7 (left) compares the calculated spectra after 1.2 m of propagation in 3 different fibre designs, all with a wall thickness of $w = 130$ nm. From Fig. 4.3 it is known that $\bar{\beta}_2$ changes sign at a core size of approximately 1450 nm. As is also seen from Fig. 4.4, it is therefore expected that spectral dips appear between the pump and the Stokes and anti-Stokes bands in the SC when the core size exceeds 1450 nm (for a fibre with $w = 130$ nm). This is also what is observed in Fig. 4.7 (left): Increasing the core size

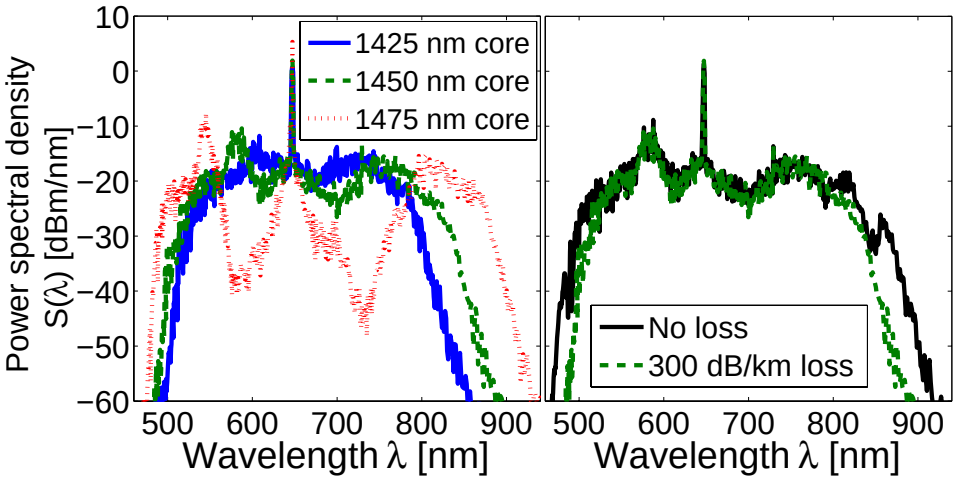

Figure 4.7: *Left:* Calculated output spectra from three different fibres. *Right:* Calculated output spectra for the $d_{\text{core}} = 1450$ nm fibre with and without a wavelength-independent loss of 300 dB/km. The wall thickness $w = 130$ nm and the propagation length $z = 1.2$ m in both figures.

from 1450 to 1475 nm widens the spectrum, but introduces a spectral dip between the pump and the Stokes and anti-Stokes lines. This demonstrates the important role of accurate fibre design to optimize the dispersion profile to obtain a flat SC.

Finally, in Fig. 4.7 (right) two simulations with and without the wavelength-independent loss of 300 dB/km are compared. For a fibre length of 1.2 m, the linear loss is only 0.36 dB. Nevertheless, the nonlinear effects could be highly sensitive to even a small loss, which is therefore investigated. It is seen in Fig. 4.7 (right) that including the loss does not significantly affect the central part of the SC spectrum, and only slightly reduces the width of the spectrum. In the cases investigated here, it is therefore seen that the relatively high losses of the nonlinear PCF do not have a significant effect on the SCG.

4.3 Physical mechanisms

As mentioned above, there is an excellent agreement between the location of the Stokes and anti-Stokes bands calculated in Fig. 4.5 and the location of the Stokes and anti-Stokes peaks in the simulated spectra in Fig. 4.6. The peaks merge due to SPM and cross-phase modulation (XPM) [102], and the degree of merging with the pump is determined by the distance between the pump wavelength and the Stokes and anti-Stokes bands. The resulting spectra can thus be explained physically solely on the basis of FWM, SPM, and XPM.

The influence of the Raman effect is clearly seen from the equations in Subsection 2.2.3. From Eq. (2.26), which can be assumed valid because $\Omega_{\max} > 3\times\Omega_{\mathrm{R}}$ for $d_{\mathrm{core}} > 1415$ nm ($w = 130$ nm), the maximum parametric gain obtained for $\kappa = 0$ is

$$g_{\max} = \gamma P_0(1 - f_{\mathrm{R}})\,, \qquad \Omega_{\max} \gg \Omega_{\mathrm{R}}, \tag{4.1}$$

which means that the Raman effect is responsible for reducing the FWM gain by a factor of $(1 - f_{\mathrm{R}})$. This was confirmed by making simulations where f_{R} was set to zero, which led to a more rapid growth of the Stokes and anti-Stokes peaks than with $f_{\mathrm{R}} = 0.18$ [3].

The Raman effect is also responsible for shifting the location of the Stokes and anti-Stokes peaks. From Eq. (2.25), it is found for the case where all higher-order dispersion terms are negligible [3]:

$$\Omega_{\max}^2 = \frac{-2\gamma P_0(1 - f_{\mathrm{R}})}{\bar{\beta}_2}\,, \qquad \Omega \gg \Omega_{\mathrm{R}}. \tag{4.2}$$

In this case, $\Omega_{\max}$ is reduced by a factor of $\sqrt{(1 - f_{\mathrm{R}})}$, corresponding to a shift of $\approx 10\%$. For the case where $\bar{\beta}_2$ is negligible (close to the ZDW) and dispersion terms higher than $\bar{\beta}_4$ are neglected, one obtains [3]

$$\Omega_{\max}^4 = \frac{-24\gamma P_0(1 - f_{\mathrm{R}})}{\bar{\beta}_4}\,, \qquad \Omega \gg \Omega_{\mathrm{R}}, \tag{4.3}$$

which means that in this case the Raman effect only results in a peak shift of $1 - (1 - f_{\mathrm{R}})^{1/4} \approx 5\%$.

At the beginning of the fibre, the Raman effect is therefore responsible for reducing the growth rate of the FWM peaks, and slightly shifting the

location of the peaks. For longer fibres it is expected that the pulse will eventually break up into femtosecond solitons due to MI, as demonstrated for quasi-continuous-wave (CW) pulses in Chapter 5. The Raman effect then causes the solitons to red-shift (soliton self-frequency shift) [13].

4.4 Summary and discussion of chapter 4

It was shown how the design of a cobweb PCF affects SCG using picosecond pulses with low average power. It was found that there is an inherent tradeoff between the width of the spectrum (determined by the location of the Stokes and anti-Stokes bands) and the flatness of the spectrum. The spectrum is relatively flat when there is a continuous gain region between the pump and the Stokes and anti-Stokes lines. This occurs for fibres where $\bar{\beta}_2 < 0$ (pumping in the anomalous dispersion region), and can be achieved by appropriate fibre design. Calculations of pulse propagation in the fibres demonstrated how an increase in core size of only 25 nm significantly affects the resulting spectrum, by widening the spectrum but at the same time degrading the flatness of the spectrum.

For comparison, random variations of the core size along the fibre length arising during fabrication are typically less than 1% over hundreds of metres of fibre [103]. Measurements show that the outer diameter of a 125 μm fibre varies less than ±0.5 μm over such long fibre lengths. Assuming that the core size scales with the outer diameter, this corresponds to a variation in core size of less than ±5.6 nm for a 1400 nm core size. For shorter fibre lengths, such as the ones modelled here, the variation in core size can be expected to be significantly less [103]. An increase in core size of 25 nm can therefore not be expected to occur due to random variations along the fibre length, and the SCG should therefore be robust against such fibre irregularities.

The generalisation in Chapter 2 of the standard FWM theory [13] was used to show that the Raman effect is responsible for reducing the FWM gain, and for slightly shifting the Stokes and anti-Stokes peaks closer to the pump, in the case where the peaks are much further away from the pump than the Raman shift of 13.2 THz in silica.

It was also shown that the relatively high loss of the cobweb PCF does not significantly affect the SCG.

Chapter 5

Continuous-wave pumping

As described in Chapter 3, supercontinuum (SC) sources are often pumped using femtosecond lasers (see, e.g., [20, 51, 54, 56, 72, 78]), offering pulses with several kilowatts of peak power [71]. Femtosecond lasers are typically complex and bulky; therefore more compact picosecond [61] and even nanosecond [20] pump sources have also been used. Physical mechanisms responsible for spectral broadening when pumping with femtosecond and picosecond pulses were investigated in Chapters 3 and 4, respectively.

Advances in fibre laser technology in recent years have also led to continuous-wave (CW) fibre lasers with sufficiently high power ($\sim$ 0.1–15 W) to be used for supercontinuum generation (SCG) [104–106]. It has been demonstrated that a CW-pumped SC source provides sufficiently high output power and broad bandwidth to be used for ultrahigh resolution optical coherence tomography (OCT) [107]. Experimental characterization of the noise of the CW pumped SC showed that the relative intensity noise (RIN) can be 30-50 dB lower than that achieved using a femtosecond pump [108]. Other experiments with a CW-pumped SC found RIN values comparable to those with a femtosecond pump [109].

CW pumping for SCG has been investigated both by pumping in the anomalous dispersion region (ADR) [105, 106, 108, 110–112] and the normal dispersion region (NDR) [113, 114]. This chapter focuses on pumping in the ADR, as this is known to result in the broadest spectra (see references above). The spectral broadening achieved using CW pumping in the ADR has previously been explained as being seeded by modulation instability

(MI), which causes break up of the CW into solitons. The solitons are then red-shifted due to the soliton self-frequency shift (SSFS) [108, 110–112]. During the red-shift the solitons may also transfer energy to blue-shifted dispersive waves. Thus, after MI-induced break up into solitons, the spectral broadening is essentially caused by the same mechanisms as when using femtosecond pumping [56].

Frosz *et al.* recently found that the role of an important physical mechanism had been overlooked in some of the latest work on CW pumped SCG [4]. It turns out that solitons generated directly from MI are too temporally broad to undergo any significant red-shift. As shown originally by M. N. Islam *et al.* the MI-generated solitons undergo collisions, in which they can transfer energy between each other [115]. It is then possible for one of the solitons to acquire sufficient peak power to undergo a large red-shift.

In Section 5.1 an overview of previous numerical modeling of CW-pumped SCG is provided, and the choice of how to model the CW input is justified. A description of the implemented phase noise model and propagation simulation is also given. Section 5.2 describes the primary mechanisms involved in the spectral broadening during propagation along the fibre. It is shown that soliton collisions can play a crucial role in CW-pumped SCG. Section 5.3 investigates the influence of the time window width, the quasi-CW pulse temporal width, the pump spectral linewidth, and the fibre dispersion profile. First, Subsection 5.3.1 shows how the influence of soliton collisions is practically absent, if the time window of the calculations is too narrow. The role of the quasi-CW pulse length is studied in Subsection 5.3.2. In Subsection 5.3.3 results are presented showing that the output spectrum can differ significantly depending on the spectral linewidth of the CW pump laser. It is shown in Subsection 5.3.4 that SCG in a fibre with smaller dispersion at the pump wavelength is less sensitive to the spectral linewidth of the pump laser. Section 5.4 compares the simulation results to experimental measurements found in the literature. The chapter is concluded with a summary and discussion in Section 5.5.

5.1 Modelling of a partially coherent continuous-wave input

One important aspect of modelling the nonlinear propagation of a CW beam in an optical fibre is how to model the CW input. In the following, an account is first given of previous numerical modelling of the CW input (Subsection 5.1.1). The phase noise model implemented here is described in Subsection 5.1.2. The propagation modelling is briefly described in Subsection 5.1.3 and the dispersion profiles for the fibres modelled here are shown. Important numerical considerations are made in Subsection 5.1.4.

5.1.1 Previous numerical modelling

Kobtsev and Smirnov used the *one photon per mode* approach [111]. This method has previously been used to model SCG using picosecond pulses [61] and consists of phenomenologically adding one photon with random phase to each frequency bin of the input field (see Appendix A.4). It was shown by Smith in 1972 that this fictitious injection of photons to the input field leads to the same output power at the Raman Stokes wavelength (downshifted from the pump by 13.2 THz) as Raman amplification of spontaneous emission along the fibre length [116]. However, as shown in the following this approach suffers mainly from two drawbacks: (1) There is no inherent spectral linewidth, and (2) the power spectral density at the Raman Stokes wavelength can be significantly underestimated. As mentioned in Subsection 5.1.2 it is reasonable to assume a Lorentzian spectrum for a partially coherent CW field. It is shown in Fig. 5.1 that a Lorentzian spectrum for a CW field with an average power of 10 W, centre wavelength of 1064 nm and a FWHM power spectral width of 30 GHz (~ 0.1 nm) has significantly more spectral power at the Raman Stokes wavelength of 1116 nm, than a CW field containing one photon per mode. The one photon per mode method is therefore unsuited to investigate the influence of the pump laser spectral linewidth and may underestimate the Raman Stokes power spectral density at the input. This is critical when Raman scattering is dominant because the input Raman Stokes power acts as a seed for the exponential gain along the fibre.

Vanholsbeeck *et al.* also made a phenomenological approach by taking

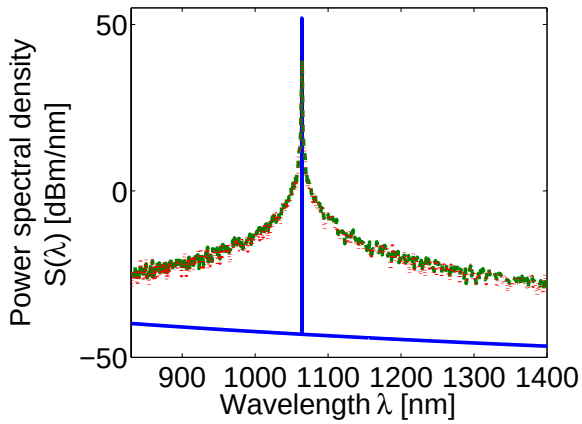

Figure 5.1: Comparison of power spectral density $S(\lambda)$ for two noise models: CW with one photon per mode (blue, solid) and CW with phase noise (resulting in a Lorentzian spectrum) corresponding to FWHM linewidth of 30 GHz (~ 0.1 nm) (green, dashed). Average power of input field is 10 W. Red dotted curve: power spectrum of super-Gaussian pulse with phase noise (30 GHz linewidth), 30 ps width and 10 W peak power [this spectrum is scaled so integrating over the spectrum gives 10 W to allow comparison with the (green, dashed) CW spectrum].

the input spectrum of the field to be $\tilde{A}(\nu) \propto \sqrt{S_\mathrm{m}(\nu)}\exp[i\phi(\nu)]$, where $\phi(\nu)$ is a random spectral phase and $S_\mathrm{m}(\nu)$ is the measured power spectral density of the pump laser to be modelled [112]. This approach *mathematically* assures that the power spectrum of the input field is as desired, $\left|\tilde{A}(\nu)\right|^2 \propto S_\mathrm{m}(\nu)$. But the choice of randomly imposing a spectral phase has no *physical* justification. The strong temporal fluctuations of the input field $A(t)$ obtained by inverse Fourier transform of $\tilde{A}(\nu)$ are therefore not necessarily present in a real partially coherent CW beam, as also stated by the authors in Ref. [112]. Recently, it was pointed out by Barviau *et al.* that modifying the statistics of the spectral phase $\phi(\nu)$ has a significant influence on the spectral evolution along the fibre [114]. One must therefore be careful when using arbitrary statistical properties for the spectral phase.

Cavalcanti *et al.* used a time-independent average field on which noise appears as small fluctuations in amplitude and phase to study the influence of MI on the statistical properties of a partially coherent beam [117].

Mussot *et al.* disregarded amplitude fluctuations and included only phase noise to investigate the spectral broadening mechanism [110]. As shown in Subsection 5.1.2, the phase noise can be directly related to the measurable linewidth of a CW laser. Furthermore, the underlying phase-diffusion model is widely accepted as an appropriate model for lasers operating far above threshold (see e.g. Refs. [110, 117], and references therein). Since this method involves both a physically justified choice of phase noise statistics and includes a finite spectral linewidth, it is physically reasonable and used in the work presented here [4]. This also allows the influence of the spectral linewidth of the CW pump on the SCG to be investigated.

5.1.2 Phase noise model

The input field envelope is modelled here as [110, 117]

$$A(0,t) = \sqrt{P_0}\exp[i\delta\phi(t)], \tag{5.1}$$

where $\delta\phi(t)$ are small fluctuations with zero ensemble average, $\langle\delta\phi\rangle = 0$. This means that for any t, averaging over many statistical realizations (ensembles) of $\delta\phi(t)$ gives a zero average. P_0 is the power of the CW input field. $\delta\phi$ is modelled as a Gaussian random process [118].

In the following, it is determined how to properly relate $\delta\phi$ to a measurable quantity, namely the FWHM power spectral linewidth $\Delta\nu_{\mathrm{FWHM}}$ of the CW input.

The random phase fluctuations can be seen as arising from a random fluctuation ν_{r} of the CW frequency ν_0, so that the instantaneous frequency ν_{i} is [118]

$$\nu_{\mathrm{i}} = \nu_0 + \frac{1}{2\pi}\frac{\mathrm{d}(\delta\phi)}{\mathrm{d}t} = \nu_0 + \nu_{\mathrm{r}}(t). \tag{5.2}$$

It can be assumed in most cases that $\nu_{\mathrm{r}}(t)$ is a zero mean, statistically stationary fluctuation [118]. Here, as in Ref. [117], $\nu_{\mathrm{R}}(t)$ is modelled as Gaussian white noise with zero mean and variance $\sigma^2_{\nu_{\mathrm{r}}}$. The phase fluctuation $\delta\phi(t)$ is then found from [118]

$$\delta\phi(t) = 2\pi\int_{-\infty}^{t}\nu_{\mathrm{r}}(\xi)\mathrm{d}\xi, \tag{5.3}$$

and is a statistically nonstationary random process [118]. It remains to determine the relation between $\sigma^2_{\nu_\mathrm{r}}$ and $\Delta\nu_\mathrm{FWHM}$, which is done in the following.

It can be shown that the so-called structure function $D_{\delta\phi}(\tau) = \langle[\delta\phi(t+\tau) - \delta\phi(t)]^2\rangle$ is given by [118]

$$D_{\delta\phi}(\tau) = 8\pi^2\tau\int_0^\infty \Gamma_{\nu_\mathrm{r}}(\eta)\mathrm{d}\eta, \tag{5.4}$$

where Γ_{ν_r} is the autocorrelation function of $\nu_\mathrm{r}(t)$. Using the Wiener-Khinchin theorem [118]

$$\Gamma_{\nu_\mathrm{r}}(\tau) = \int_{-\infty}^\infty S_{\nu_\mathrm{r}}(\nu)\exp(-i2\pi\nu\tau)\mathrm{d}\nu, \tag{5.5}$$

where $S_{\nu_\mathrm{R}}(\nu)$ is the power spectral density of $\nu_\mathrm{r}(t)$, one obtains for white noise (i.e. S_{ν_r} frequency independent) over a limited bandwidth B:

$$\Gamma_{\nu_\mathrm{r}}(\tau) = S_{\nu_\mathrm{r}}\int_{-B/2}^{B/2}\exp(-i2\pi\nu\tau)\mathrm{d}\nu. \tag{5.6}$$

The bandwidth limit is introduced because the split-step Fourier method implies both a finite time- and frequency-domain in the calculations. Since $\sigma^2_{\nu_\mathrm{r}} = \Gamma_{\nu_\mathrm{r}}(0)$ [118], one has

$$\sigma^2_{\nu_\mathrm{r}} = \Gamma_{\nu_\mathrm{r}}(0) = S_{\nu_\mathrm{r}}\int_{-B/2}^{B/2}\mathrm{d}\nu = S_{\nu_\mathrm{r}}B \Rightarrow S_{\nu_\mathrm{r}} = \frac{\sigma^2_{\nu_\mathrm{r}}}{B}. \tag{5.7}$$

Inserting this in Eqs. (5.4) and (5.6), one obtains

$$D_{\delta\phi}(\tau) = 8\pi^2\tau\frac{\sigma^2_{\nu_\mathrm{r}}}{B}\int_0^\infty\int_{-B/2}^{B/2}\exp(-i2\pi\nu\eta)\,\mathrm{d}\nu\,\mathrm{d}\eta = 4\pi^2\tau\frac{\sigma^2_{\nu_\mathrm{r}}}{B}. \tag{5.8}$$

The structure function $D_{\delta\phi}(\tau)$ is related to $\Delta\nu_\mathrm{FWHM}$ by [117] $D_{\delta\phi}(\tau) = 2\pi\Delta\nu_\mathrm{FWHM}\tau$, which together with Eq. (5.8) finally gives the following relation between $\sigma^2_{\nu_\mathrm{r}}$ and $\Delta\nu_\mathrm{FWHM}$:

$$\sigma^2_{\nu_\mathrm{r}} = \frac{\Delta\nu_\mathrm{FWHM}B}{2\pi}. \tag{5.9}$$

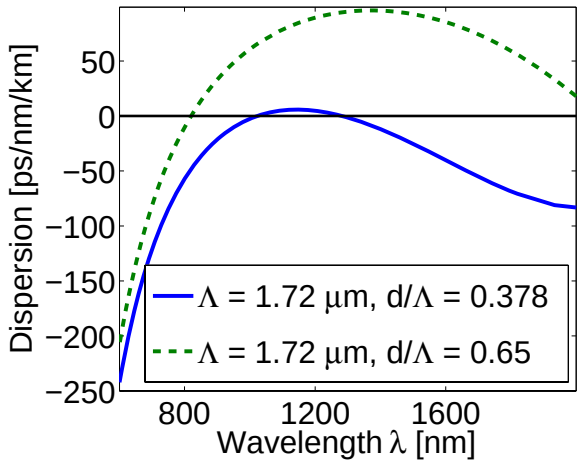

Figure 5.2: Calculated dispersion profiles for fibres considered in this chapter.

In summary, $\nu_\mathrm{r}(t)$ is stochastically sampled as Gaussian white noise for each t, with zero mean and variance $\sigma^2_{\nu_\mathrm{r}}$. Equation (5.3) then gives the phase fluctuation $\delta\phi(t)$, which is inserted in Eq. (5.1) to obtain the input field for the propagation simulation. Due to the assumptions of the statistical properties of the phase noise, the power spectrum of the input field has a Lorentzian line shape [117], with a FWHM given by $\Delta\nu_\mathrm{FWHM}$.

5.1.3 Propagation modelling

The propagation of the CW field in the photonic crystal fibre (PCF) is simulated using Eq. (2.2). The dispersion parameters $\bar{\beta}_m$ are obtained from a polynomial fit to the dispersion profile calculated using fully-vectorial plane-wave expansions [58] and shown in Fig. 5.2. The triangular structured PCF with pitch $\Lambda = 1.72$ μm and relative hole size $d/\Lambda = 0.65$ corresponds to a fibre made by Crystal Fibre A/S. This was also the fibre used in Refs. [106, 107][1]. To investigate the influence of the dispersion profile, a PCF with the relative hole size $d/\Lambda = 0.378$ was also con-

[1]Note that both papers state that $d = 0.65$ μm, but this does not correspond with the reported core size of $d_\mathrm{core} = 2.3$ μm ($d_\mathrm{core} \approx 2\Lambda - d$) and is believed to be a misprint [92].

sidered. $\bar{\beta}_2 = 4.38 \times 10^{-26}$ s^2/m and $\bar{\beta}_2 = 2.03 \times 10^{-27}$ s^2/m for the $d/\Lambda = 0.65$ and the $d/\Lambda = 0.378$ fibre, respectively. The transverse field distribution $F(x, y, \omega)$ of the fundamental mode was also calculated with the fully-vectorial plane-wave expansions. From this $A_{\text{eff}}(\omega)$ was calculated using the more general definition, Eq. (2.36). This resulted in nonlinear parameters of $\gamma(\lambda_0 = 1064 \text{ nm}) = 48.7$ (W km)$^{-1}$ and 24.9 (W km)$^{-1}$ for the $d/\Lambda = 0.65$ and the $d/\Lambda = 0.378$ fibre, respectively.

The propagation Eq. (2.2) was solved using the improved adaptive step size method described in Subsection 2.5.1. The relative change in photon number was less than 5.5% for all results presented in this chapter. An example of the change in photon number along the fibre was shown in Fig. 2.4. Figure 5.3 shows the resulting spectra for the same parameters as in Fig. 2.4 and compares the spectra obtained with a change in photon number of 3.9% and 6.5%, respectively (the latter is only shown for comparison and therefore does not violate the 5.5% limit for presented results). It is seen that despite the different change in photon number, the spectra are practically indistinguishable, except that the red-shifted soliton centred around ~ 1225 nm is red-shifted approx. 8 nm more for the case with larger change in photon number. It can therefore be expected that reducing the photon number further would mostly result in solitons slightly less red-shifted.

5.1.4 Numerical considerations

An ideal CW field has an infinite extent in time, but with the split-step Fourier method one can only model the propagation of an input field with finite temporal width. Furthermore, the method implies that the input field is periodic [13]. This means that pulse energy going out through one side of the time window will reappear from the other side of the time window.

Due to the phase noise, the phase $\delta\phi(0)$ of the input field at one edge of the time window, will differ from the phase $\delta\phi(T_{\max})$ at the other edge of the time window. There will therefore be a large phase discontinuity in the periodic input field (Fig. 5.4, bottom). Unfortunately, this phase discontinuity leads to large intensity fluctuations at the edges of the time window, since phase noise is converted to intensity noise upon propagation in a dispersive medium (see, e.g., Ref. [119]).

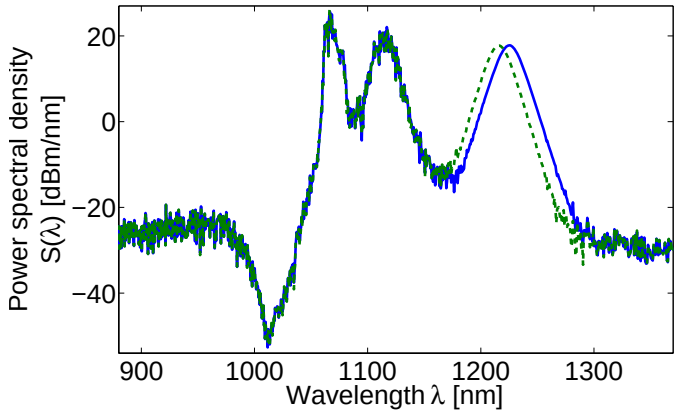

Figure 5.3: Resulting spectra at $z = 80$ m when using either the step size selection criteria $\delta \approx \delta_{\mathrm{G}} = 10^{-6}$ (solid, blue) or $\delta/(h/L) \approx \delta_{\mathrm{Gh}} = 1$ (green, dashed), resulting in a change of photon number of 6.5% or 3.9%, respectively. Parameters: $L = 100$ m, $\Lambda = 1.72$ µm, $d/\Lambda = 0.65$, quasi-CW input with $\lambda_0 = 1064$ nm, $P_0 = 10$ W, $2T_{\mathrm{sG}} = 30$ ps (explained in Subsection 5.1.4) and $\Delta\nu_{\mathrm{FWHM}} = 30$ GHz.

To avoid this problem in the numerical simulations, one can artificially replace the CW field with a broad Gaussian [117] or super-Gaussian [105] pulse. The input field [Eq. (5.1)] is multiplied with a super-Gaussian pulse,

$$A(0,t) = \sqrt{P_0}\exp[i\delta\phi(t)]\exp\left[-\frac{1}{2}\left(\frac{t}{T_{\mathrm{sG}}}\right)^{2m}\right], \tag{5.10}$$

where $m = 10$ is used here, and T_{sG} is the $1/e$ intensity half-width of the super-Gaussian pulse, see Fig. 5.4 (top). It was shown in Fig. 5.1 that multiplication with the super-Gaussian pulse practically does not affect the spectrum of the CW input field (there is almost no difference between the green and the red curves), for the values of T_{sG} used here.

There are now two important deviations of the model from a real CW field: (1) T_{sG} is finite, meaning that due to dispersion some of the pulse energy, e.g. in the form of a soliton with a carrier frequency slightly offset from the centre frequency of the CW field, can move beyond the edges of the super-Gaussian pulse. This soliton will then no longer interact with the remaining super-Gaussian pulse. (2) The time window is finite; as explained

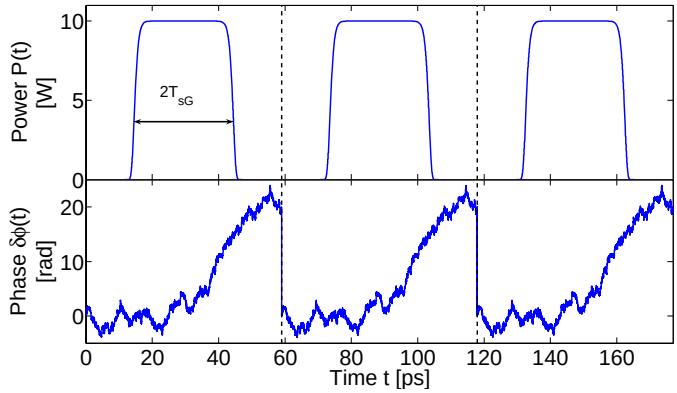

Figure 5.4: An illustration of the modelled periodic super-Gaussian input pulse. *Top:* Power variation in time. *Bottom:* Phase fluctuation in time for one particular ensemble. In this example the width of the time window $T_{\max}$ is 59.0 ps, the width of the super-Gaussian pulse is $2T_{\mathrm{sG}} = 30$ ps, and $\Delta\nu_{\mathrm{FWHM}} = 265$ GHz.

before this means that pulse energy leaving one side of the time window reappears from the other side of the time window, as was also described in Ref. [112].

Instead of an infinite CW field, one is thus actually modelling a CW laser which is turned on and off periodically. Each time the laser is turned on, the phase noise fluctuations are the same as before (see Fig. 5.4). The influence of these deviations decreases as the widths of the super-Gaussian pulse and the time window are increased. In Section 5.3, the effects of these limitations are examined closer.

The power spectra in this chapter are scaled so that $\int S(\lambda)\mathrm{d}\lambda$ gives the average power within the time window [Eq. (A.27)].

It should be noted that an optical spectrum analyser typically has a minimum integration time on the order of milliseconds. One should therefore in principle simulate a quasi-CW pulse with this duration to obtain sufficient statistical information to compare with an experimental measurement. Unfortunately, the calculation time of the numerical simulations based on the fast Fourier transform (FFT) scales with $N_{\mathrm{p}} \log_2(N_{\mathrm{p}})$ (see e.g. [65]), where N_{p} is the number of computational points and is proportional to the width of the time window for a fixed temporal resolution. To decrease calcula-

tion time it is therefore common to simulate several shorter pulses, each only differing by the random initial conditions, and then average over the ensembles [111, 112, 117].

5.2 Collision of solitons

For the cases presented in this chapter it was found that three physical mechanisms are mainly responsible for the spectral broadening. One mechanism is Raman gain, which occurs when some of the power of a strong optical field (the pump) is converted to a longer wavelength (the Raman Stokes wave), as explained in Subsection 2.2.4. A weak optical field propagating at a frequency upshifted from the pump by 13.2 THz (the anti-Raman Stokes wave) is exponentially damped due to energy transfer to the pump.

The second mechanism is MI (Subsection 2.2.3) which causes a CW pump to break up into a periodic pulse train [13]. The pulse train can then evolve into a series of solitons.

The third mechanism is *collision of solitons* [115]. The unperturbed soliton (Subsection 2.2.2) propagates without changing its shape, amplitude or width even after collision with a soliton of different carrier frequency (and therefore different group velocity) [120]. Perturbations such as third-order dispersion (TOD), self-steepening, and delayed Raman response [all included in Eq. (2.2)] lead to, in the case of TOD, emission of radiation during collision [121]. Two solitons colliding in the presence of delayed Raman response transfer energy from the soliton with the highest carrier frequency to the other soliton; this has been shown by both numerical simulations [122] and theoretical analysis [115, 123, 124]. In general, solitons can transfer energy during collisions in non-integrable models; there is some indication that energy is preferentially transferred to the soliton with the largest amplitude [125]. A soliton propagating in a medium with delayed Raman response is downshifted in frequency (red-shift) during propagation due to the SSFS, as described in Subsection 2.2.4. The red-shift is enhanced during collision with another soliton [122]. It is expected that delayed Raman response is the perturbation with the most significant effect on soliton collisions [124, 126].

All of these physical mechanisms are studied in the spectrograms [Eq. (3.2), with $\alpha_{\mathrm{sp}} = 72$ fs] shown in Fig. 5.5. Initially, the quasi-CW pump breaks up into a periodic pulse train after just a few metres of prop-

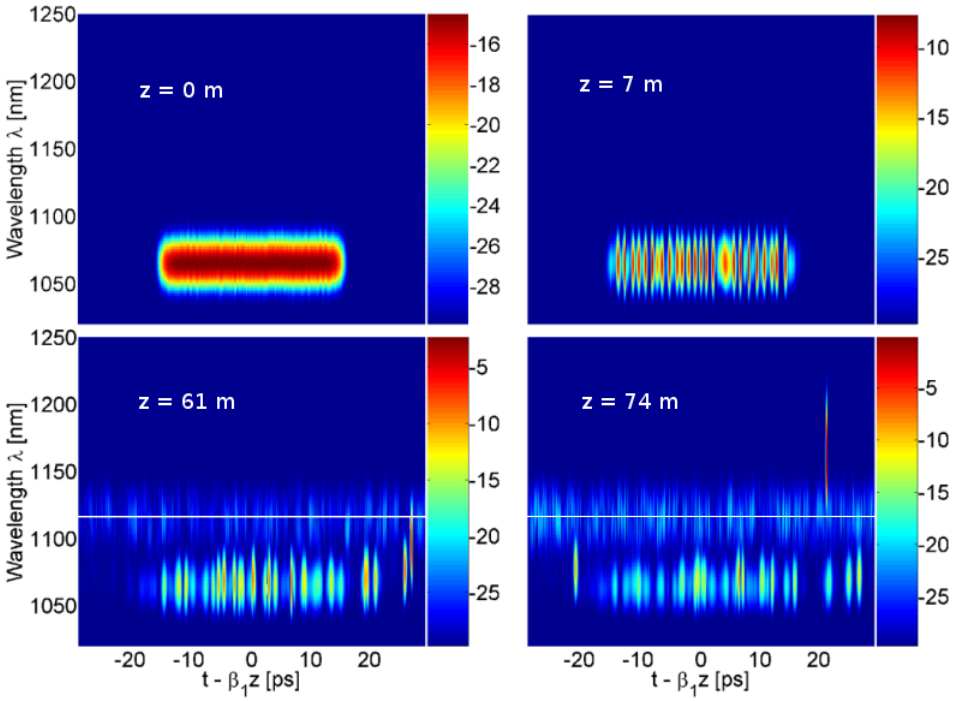

Figure 5.5: Spectrograms for one simulation of propagation in the $d/\Lambda = 0.65$ fibre. Input super-Gaussian pulse width $2T_{\mathrm{sG}} = 30$ ps, $\Delta\nu_{\mathrm{FWHM}} = 30$ GHz, time window $T_{\max} = 59$ ps. Note that the colour scale changes during propagation, as some of the solitons acquire higher peak power. The horizontal white line on the bottom figures indicates the Raman Stokes wavelength at 1116 nm. Animation expected to be available online after publication of Ref. [4].

agation due to MI. To verify that the break up is caused by MI, $\left|\tilde{P}(\nu)\right|^2$ has been plotted in Fig. 5.6 (left), where $\tilde{P}(\nu)$ is the Fourier transform of the pulse power $P(t) = |A(t)|^2$. MI provides maximum gain for oscillations with a frequency given by [13]

$$\nu_{\max} = \sqrt{\frac{\gamma P_0}{2\pi^2 \left|\bar{\beta}_2\right|}}, \tag{5.11}$$

which is indicated in Fig. 5.6 (left) by vertical lines for the two fibres con-

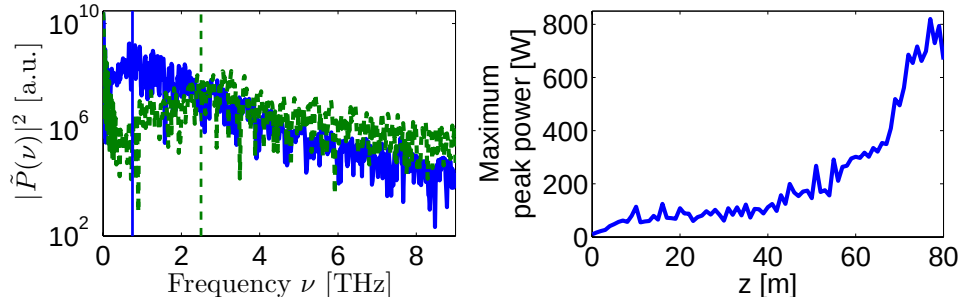

Figure 5.6: *Left:* Frequency spectrum of pulse power $P(t)$ at $z = 9$ m calculated for one simulation for the $d/\Lambda = 0.65$ fibre (blue, solid) and one simulation for the $d/\Lambda = 0.378$ fibre (green, dashed). The vertical lines indicate the frequency with maximum MI gain in the corresponding fibres: $\nu_{\max} = 0.75$ THz and 2.5 THz for the $d/\Lambda = 0.65$ and the $d/\Lambda = 0.378$ fibre, respectively. *Right:* Maximum peak power along the fibre length for the same simulation as shown in Fig. 5.5.

sidered here [Eq. (5.11) can be derived from Eq. (2.25) by neglecting all higher-order dispersion terms and the Raman effect]. It is seen that oscillations at the MI frequency are significant for both fibres and are therefore the main cause of pulse train formation.

As seen from the spectrograms, Fig. 5.5, the periodic pulse train evolves into solitons. The number of solitons can be estimated as the ratio between the super-Gaussian pulse width and the period $T_{\mathrm{MI}} = 1/\nu_{\max}$ of the periodic pulse train: $2T_{\mathrm{sG}}/T_{\mathrm{m}} = 2T_{\mathrm{sG}} \times \nu_{\max} = 30$ ps $\times$ 0.75 THz ≈ 23. This corresponds well with the number of solitons in the top right of Fig. 5.5. The solitons have slightly different group velocities for two reasons. First, the carrier frequency of the CW pump fluctuates in time due to the phase noise. Second, they have slightly different temporal widths, which means that the rate of SSFS is also different. SSFS causes the carrier frequency ν_0 of a soliton to red-shift as it propagates along the fibre, as described in Subsection 2.2.4.

Because of the slightly different group velocities, and perhaps to some degree also by soliton attraction/repulsion [13], the solitons undergo collisions as they propagate. As previously stated, each collision leads to a fractional amount of energy transfer to the most red-shifted soliton. A soli-

ton that gains energy from a collision increases its peak power and decreases its temporal width to maintain its fundamental soliton shape [see Eq. (2.15)] [13]. The decrease in temporal width leads to an increased red-shift rate, which in turn modifies the group velocity. This soliton will then also collide with more solitons. The mechanism is therefore self-amplifying. It is seen in Fig. 5.5 how one particular soliton gradually gains energy and obtains such a short temporal width that it red-shifts significantly faster than the other solitons. Figure 5.6 (right) shows the maximum peak power of the propagated field along the fibre, for the same simulation as in Fig. 5.5. It is known from Fig. 5.5 that the soliton formation from MI is complete after less than ~ 10 m of propagation. It is seen from Fig. 5.6 (right) that the maximum peak power continues to increase along the fibre after a propagation length of $z = 10$ m because of the energy transfer during soliton collisions.

The temporal width of the MI-generated solitons can be estimated from the MI oscillation period $T_{\mathrm{MI}} = 1/\nu_{\max}$. Thus, the duration of the generated solitons is $1/(0.75\ \mathrm{THz}) \approx 1.3$ ps and $1/(2.5\ \mathrm{THz}) \approx 0.4$ ps, in the $d/\Lambda = 0.65$ and the $d/\Lambda = 0.378$ fibre, respectively. Since the red-shift rate for such soliton durations is proportional to T_0^{-4} [Eq. (2.28)], even a small decrease in pulse width could lead to a significant increase in red-shift rate.

To clarify that energy transfer during soliton collisions is necessary for the large observed red-shift, and that the resulting spectrum can not be explained by MI and SSFS alone, the following analysis is performed. The most red-shifted soliton in Fig. 5.5 has shifted to 1161 nm at $z = 74$ m. This corresponds to a shift of $\Delta\nu_0 = -23.5$ THz from the input pump over $\Delta z = 74$ m. An estimate for the red-shift using Eq. (2.28) gives $\Delta\nu_0 \approx -8\left|\bar{\beta}_2\right| T_{\mathrm{R}} \Delta z/(2\pi 15 T_0^4) \approx -3 \times 10^{-4}$ THz, where the soliton width T_0 was approximated by the pulse train period $T_{\mathrm{MI}} = 1.3$ ps. $\beta_2(\lambda)$ changes only slightly from -4.38×10^{-26} s^2/m at $\lambda_0 = 1064$ nm to -6.14×10^{-26} s^2/m at $\lambda = 1161$ nm; $\beta_2(\lambda)$ is therefore approximated by $\beta_2(\lambda_0) = \bar{\beta}_2$. If there is no energy transfer during soliton collisions, the change in T_0 during red-shift can also be neglected. It is thus clear that the solitons generated directly from MI are too temporally long to make a notable red-shift.

To support this conclusion further, Fig. 5.7 shows the red-shift rate $\mathrm{d}\nu_0/\mathrm{d}z$ in the two regimes where Eqs. (2.28–2.29) are valid. The red-shift rate has been scaled by $-1/\left|\beta_2\right|$ for generality. The observed shift of -23.5

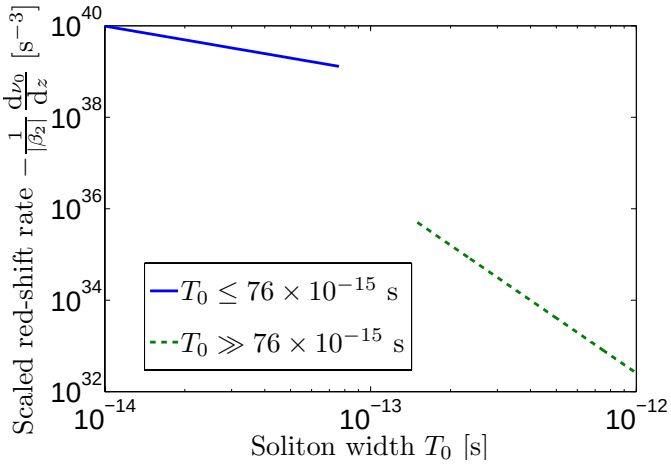

Figure 5.7: Red-shift rate $\mathrm{d}\nu_0/\mathrm{d}z$ scaled by $-1/|\beta_2|$ in the two regimes where analytical expressions are available: $T_0 \lessapprox 76$ fs [Eq. (2.29)] (blue, solid) and $T_0 \gg 76$ fs [Eq. (2.28)] (green, dashed).

THz corresponds to a mean scaled red-shift rate of $(-1/\bar{\beta}_2)\Delta\nu_0/\Delta z \approx 7.3 \times 10^{36}$ s^{-3}. It is seen from Fig. 5.7 that the scaled red-shift rate for a soliton width $T_0 \approx 1$ ps is four orders of magnitude smaller than the observed mean red-shift rate. This shows that even though there is a T_0^{-4} dependence, it is not enough for the MI-generated soliton width to change 'slightly', if the soliton is to make the observed red-shift. The soliton width has to be decreased by an order of magnitude, as seen from Fig. 5.7. This is achieved through the energy transfer during soliton collisions.

It is noted that one can also see soliton formation from MI followed by the emergence of a few quickly red-shifting high-power solitons in the simulations performed in Refs. [111, 112]. Estimates of the red-shift rate for the parameters used in those papers indicate that solitons formed directly from MI could not explain the observed red-shift; nor did the short temporal width of the observed high-power solitons correspond to the MI-oscillation period. It therefore seems that these solitons were also the result of energy transfer during collisions. The authors of Refs. [111, 112] may have overlooked this possibly because they did not consider in detail the formation of the high-power solitons using, e.g., spectrograms.

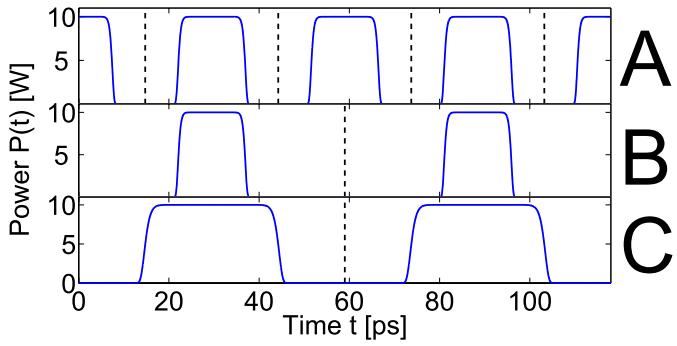

Figure 5.8: Illustration of a super-Gaussian pulse with width $2T_{\mathrm{sG}} = 15$ ps in a time domain of $T_{\max} = 29.5$ ps (top, case A), $2T_{\mathrm{sG}} = 15$ ps and $T_{\max} = 59$ ps (middle, case B), and $2T_{\mathrm{sG}} = 30$ ps and $T_{\max} = 59$ ps (bottom, case C).

5.3 Influence of numerical, pump laser, and fibre parameters

5.3.1 Time window width

First, consider case A illustrated in the top of Fig. 5.8: a super-Gaussian pulse width of 15 ps, and a time window of $T_{\max} = 29.5$ ps. 2^{14} points were used with a time resolution of $\Delta t = 1.8$ fs. This results in a frequency window of $1/\Delta t \approx 556$ THz, and a frequency resolution of $1/T_{\max} \approx 34$ GHz (see Appendix A.3). 10 simulations were performed with different seeds for the random number generator used to simulate the phase noise. As shown in Fig. 5.9 (left), all the resulting spectra have a peak at 1116 nm and a dip at 1013 nm. These features both correspond very well with a frequency shift from the pump by 13.2 THz, which is the peak frequency shift for Raman gain [13]. Thus, Raman gain is the dominant physical mechanism responsible for the resulting spectrum in this case.

Now case B is considered, illustrated in the middle of Fig. 5.8, by doubling the width of the time window to 59 ps, but keeping the width of the input super-Gaussian pulse the same as in case A. Since the time resolution is kept constant, 2^{15} points are now used. This means that the frequency resolution is halved from 34 GHz to 17 GHz. Since the frequency resolution is already high, it can be assumed that this has negligible effect on the re-

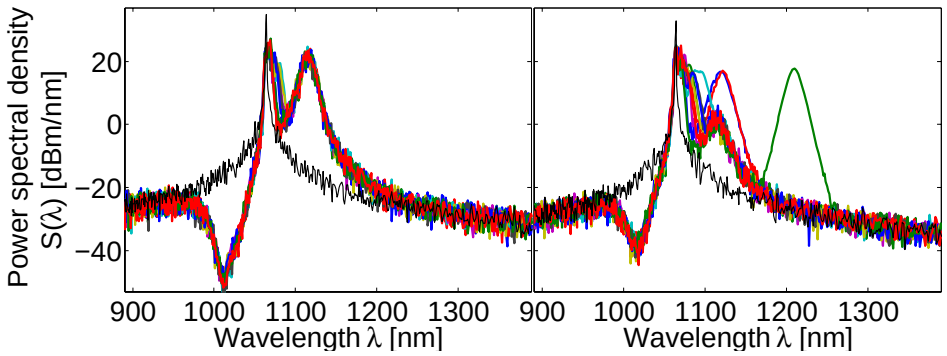

Figure 5.9: Spectra calculated for 10 ensembles differing by the random number seed for the phase noise. $\Lambda = 1.72$ µm, $d/\Lambda = 0.65$, and the fibre length $L = 80$ m. The linewidth is 30 GHz, input super-Gaussian pulse width $2T_{\mathrm{sG}} = 15$ ps. *Left:* 2^{14} points used, $T_{\max} = 29.5$ ps, smoothed over 8 points. *Right:* 2^{15} points used, $T_{\max} = 59$ ps, smoothed over 16 points.

sults. As seen in Fig. 5.9 (right) the peak and the dip resulting from Raman gain are now less prominent, indicating that less energy is transferred via the Raman effect. Also, in 3 of the 10 simulations a red-shifting soliton is seen with a centre wavelength larger than 1100 nm.

The difference in resulting spectra between cases A and B can be explained as follows [4]. The difference in $\beta_1 = 1/v_{\mathrm{g}}$ between the pump (1064 nm) and the Raman Stokes wave (1116.3 nm) was calculated to 4.0 ps/m (for the $d/\Lambda = 0.65$ fibre). This means that pulse energy transferred from the pump to the Raman Stokes wave will separate from the pump in the time domain at a rate of 4.0 ps for each metre of propagation. The Raman Stokes wave is thus spread out over the time window after just a few metres of propagation. This can be seen in the bottom of Fig. 5.5. The transfer of energy from the pump to the Raman Stokes wave requires a temporal overlap. When the time window is increased from case A to case B, the Raman Stokes wave is spread over a larger time domain, thus decreasing the temporal overlap with the pump. The transfer of energy from the Raman anti-Stokes wave to the pump, and from the pump to the Raman Stokes wave therefore becomes less efficient for case B. Since less energy is removed from the pump wavelength there remains more energy in the solitons un-

dergoing collisions. There is therefore a greater probability of a high-energy soliton being formed, with such a short temporal width that it red-shifts far-away from the pump.

Note that a super-Gaussian input pulse with the same width was simulated in cases A and B, and yet the resulting spectra are very different. This important result shows that the choice of time window width requires careful consideration.

5.3.2 Pulse temporal width

To consider case C (bottom of Fig. 5.8) the same time window as in case B is used, but now the width of the super-Gaussian input pulse is doubled to $2T_{\mathrm{sG}} = 30$ ps. The ratio of super-Gaussian pulse width and time window width, $2T_{\mathrm{sG}}/T_{\max}$, is now the same as in case A. From the physical explanation above, the Raman energy transfer from the pump to the Raman Stokes wave should now be as effective as in case A. This is because the temporal overlap between the Raman Stokes wave and the pump is the same in both cases A and C, if it is assumed that the Raman Stokes wave is quickly almost uniformly spread over the entire time window. Indeed, as seen in Fig. 5.10 (left), the Raman anti-Stokes dip and the Raman Stokes peak have practically the same power spectral density as for case A [Fig. 5.9 (left)]. It is also seen in Fig. 5.5 how the Raman Stokes wave is uniformly spread across the time window. In case A the Raman energy transfer from the pump was so severe that no red-shifting solitons were observed. However, the doubling of the super-Gaussian input pulse width, compared to case A, means that a larger number of colliding solitons will be formed from MI. This should result in a greater probability for the formation of a quickly red-shifting soliton. As expected, it is seen in Fig. 5.10 (left) that in 4 out of the 10 ensembles a soliton was observed to red-shift beyond 1100 nm.

5.3.3 Influence of pump spectral linewidth

Again the computational parameters for case C are used ($2T_{\mathrm{sG}} = 30$ ps, $T_{\max} = 59$ ps, 2^{15} points) but a FWHM power spectral linewidth of $\Delta\nu_{\mathrm{FWHM}} = 265$ GHz is simulated. The resulting spectra are seen in Fig. 5.10 (right).

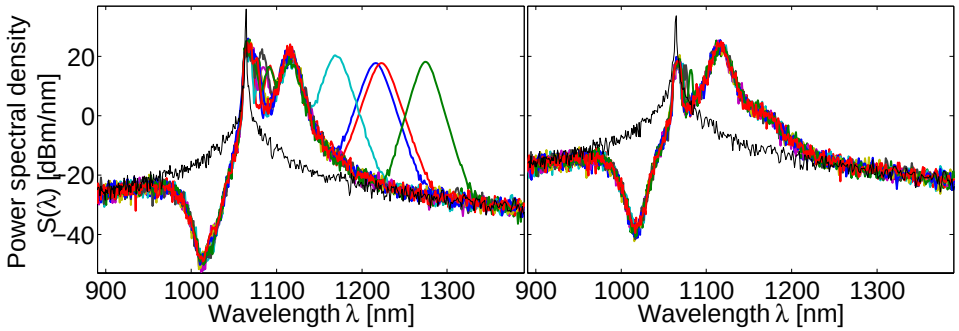

Figure 5.10: Spectra calculated for 10 ensembles differing by the random number seed for the phase noise generation. All spectra are for $\Lambda = 1.72$ µm, $d/\Lambda = 0.65$, and a fibre length of 80 m. 2^{15} points were used, $2T_{\mathrm{sG}} = 30$ ps, $T_{\max} = 59$ ps. *Left:* Spectral linewidth $\Delta\nu_{\mathrm{FWHM}} = 30$ GHz. *Right:* $\Delta\nu_{\mathrm{FWHM}} = 265$ GHz. Smoothed over 16 points. The thin black line indicates the input spectrum for one of the simulations.

The only simulation difference between the left and the right plots in Fig. 5.10 is the spectral linewidth of the quasi-CW input. None of the simulations with 265 GHz linewidth show distinct red-shifting solitons, whereas the simulations with 30 GHz linewidth show a red-shifting soliton in 4 out of 10 simulations.

Two possible explanations for this difference have been suggested [4]. (1) The larger pump linewidth leads to a larger spread in centre frequencies of solitons as they form from the pump. Since the energy transfer between two colliding solitons decreases with increasing separation in carrier frequency [122], this leads to less overall energy transfer during soliton collisions. This could then hinder the buildup of a quickly red-shifting soliton. (2) As the linewidth of the Lorentzian power spectrum is increased, the pump power spectral density $S(\lambda = 1064\ \mathrm{nm})$ is decreased, see Fig. 5.11 (left). At the same time, there is more spectral power $S(\lambda = 1116\ \mathrm{nm})$ available at the Raman Stokes wavelength. The reduction in power spectral density at the pump wavelength could also hinder the buildup of a quickly red-shifting soliton. Figure 5.11 (right) shows the power within a bandwidth of ~ 4 nm centred at the pump wavelength and the Raman Stokes wavelength, respectively, during propagation along the fibre. It is seen that for a linewidth

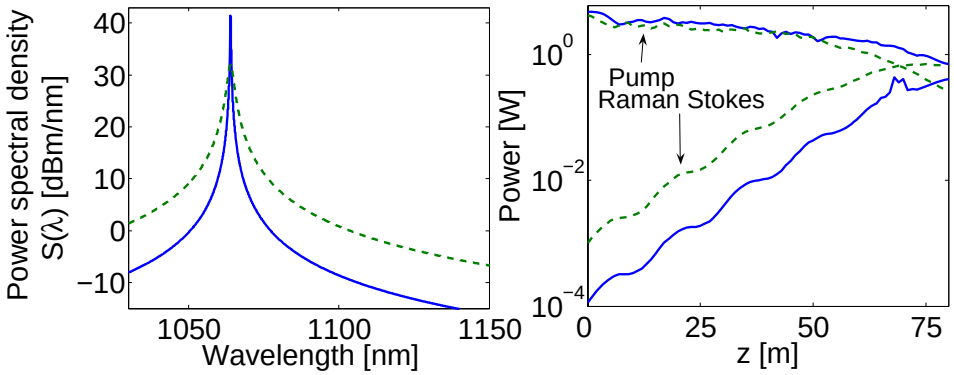

Figure 5.11: *Left:* Lorentzian shaped power spectrum for 30 GHz (solid, blue) and 265 GHz linewidth (dashed, green). *Right:* Power evolution along the fibre at the pump wavelength and the Raman Stokes wavelength of 1116 nm. One simulation for a linewidth of 30 GHz (solid, blue) and one simulation for a 265 GHz linewidth (dashed, green).

of 265 GHz there is slightly less power at the pump wavelength, and significantly more power at the Raman Stokes wavelength, compared to the simulation with a linewidth of 30 GHz.

The relative importance of these two mechanisms in hindering the buildup of a quickly red-shifting soliton has not yet been determined [4].

5.3.4 Influence of fibre dispersion profile

Now consider the fibre with the structural parameters $\Lambda = 1.72$ µm and $d/\Lambda = 0.378$. This fibre has zero-dispersion wavelengths (ZDWs) at ~ 1025 and 1281 nm, as seen from Fig. 5.2. It is also seen that the dispersion at the pump wavelength is ~ 20 times smaller for this fibre, compared to the fibre with $d/\Lambda = 0.65$. The effective area A_{eff} is ~ 2 times larger, and using Eq. (5.11) this results in an MI maximum gain frequency of $\nu_{\max} = 2.5$ THz, as was also indicated in Fig. 5.6 (left). This means that approximately 3 times more solitons should be formed in this fibre than in the fibre with $d/\Lambda = 0.65$. This is also what has been observed in spectrograms. The larger number of solitons leads to a larger number of soliton collisions which in turn increases the probability of the creation of a quickly red-shifting

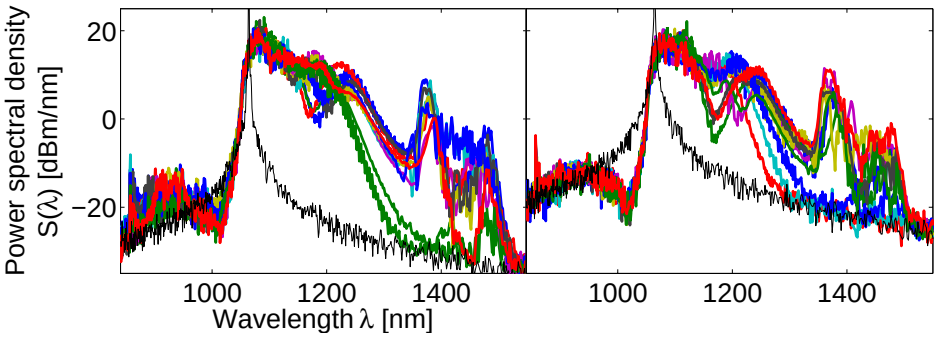

Figure 5.12: Calculated spectra at $z = 64$ m for the $\Lambda = 1.72$ μm, $d/\Lambda = 0.378$ fibre, super-Gaussian input pulse width $2T_{\mathrm{sG}} = 30$ ps, time window $T_{\max} = 59$ ps, 2^{15} points. *Left:* $\Delta\nu_{\mathrm{FWHM}} = 30$ GHz. *Right:* $\Delta\nu_{\mathrm{FWHM}} = 265$ GHz linewidth. 10 ensembles shown in both cases. The thin black line indicates the input spectrum for one of the ensembles.

soliton. Furthermore, the solitons are not only more abundant, but also have a shorter temporal width giving them a larger red-shift rate (Fig. 5.7). The resulting spectra are seen in Fig. 5.12.

It is seen that the larger number of red-shifting solitons results in a relatively smooth spectral broadening on the red side of the pump. The spectrum has achieved the large broadening at a shorter fibre distance ($z = 64$ m) than for the $d/\Lambda = 0.65$ μm fibre. The generation of dispersive waves in the normal dispersion region [1, 56] is also observed at ~ 857 nm and ~ 1376 nm.

The formation of many solitons due to the lower dispersion also means that the input linewidth is less critical than for the $d/\Lambda = 0.65$ fibre. As is seen in Fig. 5.12, the simulations with 30 GHz and 265 GHz linewidth show much more resemblance to each other than the corresponding simulations for the $d/\Lambda = 0.65$ fibre (Fig. 5.10).

5.4 Comparison with experiments

The simulations in Figs. 5.9 (right) and 5.10 (left) showed a quickly red-shifting soliton in only some of the simulations. The solitons also did not undergo the same amount of red-shift. For example, one simulation in

Fig. 5.10 (left) resulted in a soliton at $\sim$ 1170 nm and another simulation had a soliton at $\sim$ 1270 nm. It is shown in Fig. 5.13 how averaging over the ensembles smooths the peaks from individual solitons. Experimental spectra were presented for similar pumping conditions in Refs. [106, 107]. The experimental spectra showed a large pump residual at 1064 nm, a Raman Stokes peak at 1116 nm about 11 dB below the pump residual, and a relatively flat continuum spanning from $\sim$ 1150 to $\sim$ 1350 nm about 14 dB below the pump residual. This is compared with the ensemble average in Fig. 5.13 (right), corresponding to case C, because this should be a better approximation to a real CW input than case A or B. In the simulations the pump residual and Raman Stokes peak are almost at the same spectral power level. This difference between the experiments and the simulations could be caused by the fact that the simulations assume a polarised input pump and only consider propagation in one polarisation axis, whereas the experiments were done with a non-polarised pump laser. Instead of a flat continuum from 1150 nm to 1350 nm the simulations show three distinct peaks in the same wavelength region. This occurs because there is only averaged over 10 ensembles in the work presented here; it is known that the red-shift of each soliton is determined by the random initial conditions, so increasing the number of averaged ensembles would smooth the soliton spectra into a continuum. Ideally, for comparison with the measurement of an optical spectrum analyser with 1 ms integration time, one would need to average over $\sim 10^7$ ensembles, if each ensemble corresponds to a quasi-CW pulse of 30 ps duration. In practice, averaging over as few as 100 ensembles is found to give reasonable agreement with experimental measurements [111, 112].

5.5 Summary and discussion of chapter 5

In recent work it was believed that solitons formed directly from MI could red-shift far away from the CW pump [111, 112]. It was shown here that the solitons require a shorter temporal width to make a significant red-shift, at least in the cases investigated here and in Refs. [111, 112], and that this can be achieved by energy transfer during soliton collisions [4].

It was shown how the time window and pulse width used in the calculations can affect the resulting spectrum and must be chosen carefully.

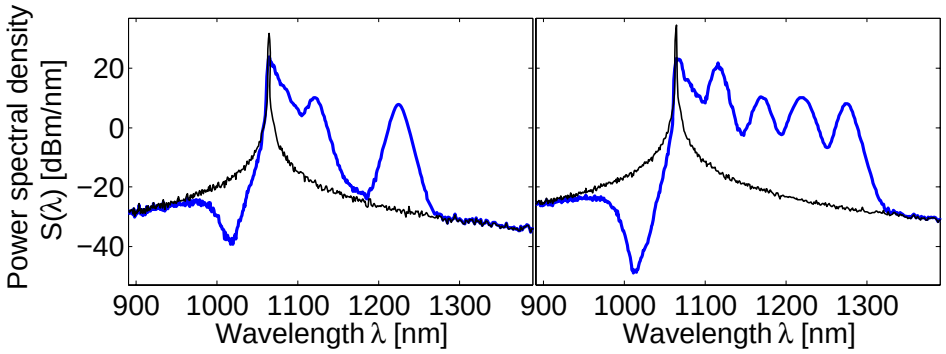

Figure 5.13: *Left:* Ensemble average for the same parameters as in Fig. 5.9 (right). *Right:* Ensemble average for the same parameters as in Fig. 5.10 (left). The averaged input spectrum is indicated as a thin black line.

Both should be chosen as large as computationally practical, but the time window should not be much larger than the pulse width, since this can lead to an underestimation of the Raman gain.

It was also demonstrated that increasing the spectral linewidth of the CW pump laser can hinder the formation of quickly red-shifting solitons. This indicates that narrow linewidth pump lasers should be selected for generating a broader supercontinuum. The number of solitons formed from a quasi-CW pulse and their red-shift rate can be increased by choosing a fibre with lower dispersion at the pump wavelength. This reduces the required fibre length and allows the use of a pump laser with broader linewidth while still obtaining quickly red-shifting solitons.

From the standard textbook theory of modelling pulse propagation (e.g. Ref. [13]) one could be led to assume that higher-order perturbations, such as the delayed Raman response, can be neglected from the propagation Eq. (2.2) if long input pulses are used. However, as shown in this chapter, even when pumping with a quasi-CW pulse, MI can cause the pulse to break up into solitons so short that the delayed Raman response can no longer be neglected. Even if an MI-generated soliton is initially temporally long, it can become much shorter during collisions with other solitons. Neglecting the delayed Raman response would also underestimate the energy transfer between solitons, since the Raman effect is expected to be the main

perturbation causing the energy transfer [124, 126].

Chapter 6

Conclusion

6.1 Summary

Supercontinuum generation (SCG) was investigated in three pumping regimes: femtosecond, picosecond, and continuous-wave (CW) or quasi-CW pumping. In each regime it was demonstrated through numerical modelling how changing the structural parameters of a photonic crystal fibre (PCF), significantly affects the supercontinuum (SC) spectrum.

For femtosecond pumping it was found that self-phase modulation (SPM) dominates the spectral broadening during the first few millimetres of propagation. It was argued that four-wave mixing (FWM) cannot be expected to play a role, because the condition of group-velocity matching required for such short pulses is not fulfilled. Furthermore, SPM alone was shown to be able to provide the observed spectral broadening. For longer fibre lengths, solitons are formed, which red-shift due to soliton self-frequency shift (SSFS). The extent of soliton red-shift is limited by the higher zero-dispersion wavelength (ZDW), as dispersive waves are amplified in the normal dispersion region (NDR) above the ZDW, when the soliton spectrum has shifted to the vicinity of the higher ZDW. The observation of an apparent bright-bright soliton pair was also described. One part of the soliton pair was in the anomalous dispersion region (ADR), while the other part was in the NDR. To the best of the author's knowledge, this was the first time this phenomenon has been observed.

In the low-average power, picosecond pumping investigation of this work,

FWM was found to be the dominant mechanism for spectral broadening. The FWM phase match condition was highly modified by changing the dispersion profile slightly. It was shown that increasing the core size and /or wall thickness of a cobweb PCF modified the dispersion so that the Stokes and anti-Stokes wavelengths shifted further away from the pump wavelength. As long as the dispersion was not made normal at the pump wavelength, the SC spectrum was relatively flat and smooth from the anti-Stokes wavelength to the Stokes wavelength. However, if the core size and/or wall thickness was increased so much that the fibre became normally dispersive at the pump wavelength, the resulting spectrum was shown to contain spectral dips between the pump and the FWM generated peaks. It was also analytically clarified that the Raman effect acts to reduce the FWM gain, and the Stokes and anti-Stokes shift from the pump.

A phase noise model was used to model a CW pump and the influence of the pump spectral linewidth. Recent work explained CW pumped SCG as caused by soliton formation from modulation instability (MI), followed by a red-shift of the solitons. This work showed that, at least for the cases here and in two of the references, the solitons formed from MI are too temporally long to undergo any significant red-shift. Instead, the solitons were found to first exchange energy during collisions, before solitons were formed with sufficiently short temporal width to make a significant red-shift. This showed that higher-order nonlinear effects, such as the Raman delayed response and self-steepening, cannot be neglected even when pumping with long pulses, except for short fibre lengths. The influence of the time window width on numerical modelling of CW pumping was investigated, and it was found that the time window width determines the efficiency of energy transfer to the Raman Stokes wavelength. The number of solitons formed from MI could be increased by choosing a fibre with less anomalous dispersion at the pump wavelength; this also reduced the temporal width of the solitons, thereby increasing the soliton red-shift rate. Finally, it was shown that increasing the spectral linewidth of the CW pump (without increasing the average power) can hinder the formation of red-shifting solitons, and thereby decrease the resulting spectral width.

6.2 Discussion of implications for OCT-sources

SC sources pumped with solid-state femtosecond lasers have provided the broadest spectra for optical coherence tomography (OCT), cf. Fig. 1.3 [27]. If a femtosecond laser is available with a centre wavelength at 800 nm, and one desires an SC centre wavelength at 1300 nm, the present work clarifies that the higher ZDW of the PCF must be located sufficiently above the pump. Otherwise, the red-shift of solitons will be halted as the solitons reach the higher ZDW. To increase the nonlinearity (with the intention of lowering the required pump power) of a triangular structured PCF one can reduce the pitch Λ, as this decreases the core size. However, this also shifts the ZDWs to shorter wavelengths [19]. The condition of placing the higher ZDW far above the pump therefore limits the nonlinearity of the PCF, and thereby also how much the required pump power can be reduced, at least for triangular structured PCFs with silica cores and the broadening mechanisms considered here.

It should be emphasized that the present investigation has focused on dispersion engineering; additional spectral shaping can be achieved through changing the pulse parameters, such as temporal width or peak power [55].

Aguirre *et al.* recently pumped 85 fs pulses at 1064 nm into a PCF with two closely lying ZDWs to generate a double peak spectrum at 800 nm and 1300 nm, and used this for OCT imaging in both wavelength regions [74]. The spectral broadening mechanisms can be assumed similar to those described in Chapter 3. It was demonstrated clearly in Section 3.4 how the spectral width and location of the two peaks can be controlled by tapering the PCF. Referring to the work of Hilligsøe *et al.* [73], Frosz *et al.* [1], and Falk *et al.* [2], the potential use of such dispersion engineering for OCT applications was acknowledged by Aguirre *et al.* [74]:

> (...) it appears that generation of smoother continuum will be realizable with further optimization of such fibers. (...) The paradigm of using theoretical analysis and numerical simulation to custom design photonic crystal fibers that achieve a desired spectral distribution will be extremely powerful for applications such as OCT that are critically dependent on the precise spectral characteristics.

An important issue with solid-state femtosecond ($\lesssim$ 10 fs) laser pumped SCG for OCT is the relatively high price ($\sim$ 160,000 US$), size and complexity of the pump laser. Present lasers are termed "compact", e.g. 90 cm $\times$ 45 cm, due to comparison with earlier femtosecond lasers, but this is still impractical for a portable OCT system. Therefore, solid-state femtosecond pumped SC sources are currently unsuitable for clinical routine diagnostics, but can be used for medical research programs where state-of-the-art resolution is required.

Picosecond pumped SC sources have been demonstrated for OCT, but the pulses were only 1.7 ps long and compressed to $\sim$ 100 fs before being coupled into a highly nonlinear fibre [127]. The broadening mechanisms were presumably similar to those described in Chapter 3. The pump laser was a compact and mechanically stable fibre laser, which could therefore be suitable for a clinical OCT system.

Using pump lasers with longer pulses ($\gtrsim$ 10 ps) could enable the spectral broadening to be dominated by FWM, as described in Chapter 4. The theory described there could then be used to control the spectral width and flatness through dispersion engineering. However, this approach has a disadvantage for OCT. FWM-dominated broadening results in a spectrum centred on the pump wavelength, so a pump laser at 1300 nm is required for OCT in this wavelength region. Since there is typically a large pump residual in the spectrum, it must be reduced by filtering to increase the full width at half-maximum (FWHM) bandwidth. It can be difficult to only reduce the pump residual without affecting the shape of the spectrum. Thus, the usefulness of FWM-dominated broadening for OCT depends on the ability to perform this filtering without degrading the spectral flatness.

A CW fibre laser has numerous practical advantages over a solid-state femtosecond laser: it is compact, mechanically stable, and can be spliced directly to the PCF. With a price of $\sim$ 6,000 US$, CW pumped SC sources seem ideal for clinical OCT applications. The feasibility for use in OCT has already been demonstrated by Hsiung *et al.* [107], although the authors state that excess noise is relatively high. Future work could investigate how the noise can be reduced and how to improve the spectral bandwidth further. The present work indicates that the broadest and flattest SC is obtained using a narrow linewidth pump laser, and a PCF with small anomalous dispersion at the pump wavelength. As with femtosecond pumping, one must

also ensure that the higher ZDW is sufficiently above the pump wavelength.

6.3 Outlook

SCG in PCFs can be expected to provide even broader and smoother spectra in the future, as the development in fibre lasers leads to increasingly larger pump power. Ultimately, the spectral width can be expected to be limited by confinement losses and material absorption in the PCF. The increase in pump power will present difficulties to the numerical modelling, since the computation time will increase along with the pump power. This could lead to a renewed interest in the split-step Fourier method and how to optimize it. The trend in scientific computing towards relying more on parallel computing could become inevitable for future modelling of SCG.

It was demonstrated in Chapter 4 how the spectral width and flatness can be modified through dispersion engineering by changing, e.g., the core size of a PCF. Since the core size is determined during production, it is not possible to later fine tune the spectrum by adjusting the core size. However, it has been both theoretically and experimentally shown for highly dispersive PCFs how the dispersion varies with temperature [128]. Thus, it should in principle be possible to fine tune the SC spectrum by temperature control of the PCF.

As a final example of future prospects in SCG, consider that the silica core in typical index-guiding PCFs has a relatively low nonlinearity. A hollow-core PCF utilizing the photonic band gap effect, on the other hand, can have its core filled with a highly nonlinear medium. This was recently investigated theoretically for the highly nonlinear liquids carbon disulfide and nitrobenzene [129]. The core can also be filled with liquid crystals [130]. Liquid crystals have the exciting advantage that their optical properties can be tuned both by applying an external electric field and/or controlling the temperature. Calculations of the chromatic dispersion at different temperatures were very recently presented and showed that the ZDW could be shifted ~ 10 nm by increasing the temperature from 25°C to 50°C [131]. Liquid crystal-filled cores could therefore possibly also be used for temperature tunable SCG.

Appendix A

Some useful formulas

A.1 Pulse parameters

Gaussian pulse

$$A(T) = \sqrt{P_0} \exp\left(-\frac{T^2}{2T_0^2}\right), \tag{A.1}$$

with pulse energy E given by

$$E = \int_{-\infty}^{\infty} |A(T)|^2 \, \mathrm{d}T = \sqrt{\pi} P_0 T_0 \approx 1.06 P_0 T_{\mathrm{FWHM}}. \tag{A.2}$$

T_0 is the half-width at $1/e$-power, related to the power FWHM by

$$T_{\mathrm{FWHM}} = 2\sqrt{\ln 2} T_0 \approx 1.665 T_0. \tag{A.3}$$

The Fourier transform of a Gaussian pulse is also a Gaussian with a FWHM power spectral width of

$$\Delta\nu_{\mathrm{FWHM}} = \frac{2 \ln 2}{\pi T_{\mathrm{FWHM}}} \approx \frac{0.44}{T_{\mathrm{FWHM}}}, \tag{A.4}$$

$$\Delta\lambda_{\mathrm{FWHM}} \approx \frac{\lambda_0^2}{c} \Delta\nu_{\mathrm{FWHM}} \approx 0.44 \frac{\lambda_0^2}{c T_{\mathrm{FWHM}}}. \tag{A.5}$$

The average power P_{av} is

$$P_{\mathrm{av}} = E f_{\mathrm{rep}} = \sqrt{\pi} P_0 T_0 f_{\mathrm{rep}} \approx 1.06 P_0 T_{\mathrm{FWHM}} f_{\mathrm{rep}}, \tag{A.6}$$

where f_{rep} is the repetition rate.

Hyperbolic-secant pulse

$$A(T) = \sqrt{P_0}\mathrm{sech}\left(\frac{T}{T_0}\right). \tag{A.7}$$

$$T_{\mathrm{FWHM}} = 2\ln\left(1+\sqrt{2}\right)T_0 \approx 1.763T_0. \tag{A.8}$$

$$P_{\mathrm{av}} = 2P_0T_0f_{\mathrm{rep}} \approx 1.13P_0T_{\mathrm{FWHM}}f_{\mathrm{rep}}. \tag{A.9}$$

A.2 Scaling of the electric field

The intensity of an electromagnetic wave $\mathbf{E}(\mathbf{r},t) = \mathbf{E}_0(\mathbf{r},t)\exp[i(\beta_0 z - \omega_0 t)]$ is given by [132]

$$I(\mathbf{r},t) = \frac{n}{2}\sqrt{\frac{\epsilon_0}{\mu_0}}\left|\mathbf{E}_0(\mathbf{r},t)\right|^2, \tag{A.10}$$

where μ_0 is the vacuum permeability. From Eq. (2.1) and the scaling relation $\mathbf{E}_{\mathrm{A}} = \sqrt{\frac{1}{2}\epsilon_0 cn}\mathbf{E}$ one has:

$$\left|\mathbf{E}_0(\mathbf{r},t)\right|^2 = \frac{2}{\epsilon_0 cn}\left|F(x,y)A(z,t)\right|^2 = \frac{2}{\epsilon_0 cn}\left|F(x,y)\right|^2\left|A(z,t)\right|^2. \tag{A.11}$$

The optical power is then found by integrating over the intensity in the xy plane:

$$\begin{aligned} P(z,t) &= \iint I(\mathbf{r},t)\mathrm{d}x\mathrm{d}y \\ &= \frac{n}{2}\sqrt{\frac{\epsilon_0}{\mu_0}}\frac{2}{\epsilon_0 cn}\left|A(z,t)\right|^2\iint\left|F(x,y)\right|^2\mathrm{d}x\mathrm{d}y \\ &= \left|A(z,t)\right|^2\iint\left|F(x,y)\right|^2\mathrm{d}x\mathrm{d}y. \end{aligned} \tag{A.12}$$

From this it is seen that if $F(x,y)$ is normalized so that $\iint\left|F(x,y)\right|^2\mathrm{d}x\mathrm{d}y = 1$, then the optical power can be calculated as

$$P(z,t) = \left|A(z,t)\right|^2. \tag{A.13}$$

A.3 Split-step Fourier method

The temporal resolution Δt, number of computational points N_p, time window width T_max, frequency window width B, and frequency resolution $\Delta\nu$ are related by (see any standard textbook on discrete Fourier transforms, e.g. Ref. [65])

$$T_\mathrm{max} = (N_\mathrm{p} - 1)\,\Delta t, \tag{A.14}$$

$$\Delta\nu = \frac{1}{N_\mathrm{p}\Delta t} \approx \frac{1}{T_\mathrm{max}}, \tag{A.15}$$

$$B = (N_\mathrm{p} - 1)\,\Delta\nu \approx \frac{1}{\Delta t}. \tag{A.16}$$

The minimum and maximum wavelengths in the calculated spectra are determined by the centre wavelength λ_0 of the simulation and the temporal resolution Δt:

$$\lambda_\mathrm{min} = \frac{\lambda_0}{1 + \frac{\lambda_0}{2c\Delta t}}, \qquad \lambda_\mathrm{max} = \frac{\lambda_0}{1 - \frac{\lambda_0}{2c\Delta t}}. \tag{A.17}$$

The power spectral density $S(\omega)$ is defined as [118]

$$S(\omega) = \lim_{T\to\infty} \frac{1}{T} \left| \int_{-T/2}^{T/2} A(t) \exp\left[i\,(\omega - \omega_0)\,t\right] \mathrm{d}t \right|^2 . \tag{A.18}$$

Since the computation of the discrete Fourier transform limits T to the width T_max of the time window,

$$S(\omega) = \frac{1}{T_\mathrm{max}} \left| \tilde{A}(\omega) \right|^2 , \tag{A.19}$$

where $\tilde{A}(\omega)$ is the discrete Fourier transform of the time window.

If $\tilde{A}(\omega)$ is scaled properly so that

$$E = \int_0^{T_\mathrm{max}} |A(t)|^2 \,\mathrm{d}t = \int_{\omega_\mathrm{min}}^{\omega_\mathrm{max}} \left| \tilde{A}(\omega) \right|^2 \mathrm{d}\omega, \tag{A.20}$$

where E is the pulse energy within the time window, then it can be easily seen that Eq. (A.19) should be replaced by

$$S(\omega) = f_{\mathrm{rep}} \left| \tilde{A}(\omega) \right|^2, \tag{A.21}$$

to obtain the scaling

$$\int_{\omega_{\min}}^{\omega_{\max}} S(\omega) \mathrm{d}\omega = P_{\mathrm{av}} = f_{\mathrm{rep}} E, \tag{A.22}$$

where f_{rep} is the pulse repetition frequency.

When plotting the power spectral density on a wavelength scale, $S(\lambda)$, it must be assured that integrating over a wavelength region $[\lambda_1; \lambda_2]$ gives the same power as integrating over the corresponding frequency region $[c/\lambda_2; c/\lambda_1]$:

$$P_{\lambda_1,\lambda_2} = \int_{\lambda_1}^{\lambda_2} S(\lambda) \mathrm{d}\lambda = \int_{c/\lambda_2}^{c/\lambda_1} S(\nu) \mathrm{d}\nu. \tag{A.23}$$

From

$$S(\lambda)\Delta\lambda = S(\nu)[-\Delta\nu] \Rightarrow S(\lambda) = -S(\nu)\frac{\Delta\nu}{\Delta\lambda}, \tag{A.24}$$

and using

$$\frac{\Delta\nu}{\Delta\lambda} \to \frac{\mathrm{d}\nu}{\mathrm{d}\lambda} = -\frac{c}{\lambda^2}, \tag{A.25}$$

one obtains the transformation relation

$$S(\lambda) = \frac{c}{\lambda^2} S(\nu) = \frac{c}{\lambda^2} f_{\mathrm{rep}} \left| \tilde{A}(\nu) \right|^2. \tag{A.26}$$

When modelling a CW or quasi-CW input with periodicity $T_{\max}$, Eq. (A.21) must be replaced by Eq. (A.19), and Eq. (A.26) replaced by

$$S(\lambda) = \frac{c}{\lambda^2 T_{\max}} \left| \tilde{A}(\nu) \right|^2. \tag{A.27}$$

A.4 One photon per mode

As described in Subsection 5.1.1, the one photon per mode approach consists in injecting the energy equivalent to one photon in each frequency bin ([116] and Section 8.1.2 in Ref. [13]) with a random spectral phase [61]. The power of the one photon per mode field is then [13, 116]

$$P_{\mathrm{oppm}} = \int_{\nu_{\min}}^{\nu_{\max}} h\nu \mathrm{d}\nu. \tag{A.28}$$

Since the power spectral density $S_{\mathrm{oppm}}(\nu)$ of the same field is related to the power by

$$P_{\mathrm{oppm}} = \int_{\nu_{\min}}^{\nu_{\max}} S_{\mathrm{oppm}}(\nu)\mathrm{d}\nu, \tag{A.29}$$

one has $S_{\mathrm{oppm}}(\nu) = h\nu$. Using Eq. (A.19),

$$\left|\tilde{A}_{\mathrm{oppm}}(\nu)\right|^2 = T_{\max} h\nu, \tag{A.30}$$

so $\tilde{A}_{\mathrm{oppm}}(\nu_m)$ is calculated for each frequency bin ν_m using

$$\tilde{A}_{\mathrm{oppm}}(\nu_m) = \sqrt{T_{\max} h\nu_m} \times \exp[i\phi(\nu_m)], \tag{A.31}$$

where $\phi(\nu_m)$ is the random spectral phase, sampled stochastically as white noise with uniform probability distribution over the interval $[0; 2\pi]$. $\tilde{A}_{\mathrm{oppm}}(\nu_m)$ is then inverse Fourier transformed to obtain $A_{\mathrm{oppm}}(t_m)$ which is added to the input field.

List of acronyms

ADR	anomalous dispersion region
CARS	coherent anti-Raman Stokes
CW	continuous-wave
EM	electromagnetic
FFT	fast Fourier transform
FFTW	fastest Fourier transform in the West
FWHM	full width at half-maximum
FWM	four-wave mixing, see p. 15 for theory
GVD	group-velocity dispersion
MI	modulation instability, see p. 15 for theory
MPI	message passing interface
NLSE	nonlinear Schrödinger equation
NDR	normal dispersion region
OCT	optical coherence tomography
OPL	Optics and Plasma Research Department
PCF	photonic crystal fibre

RIN	relative intensity noise
SC	supercontinuum
SCG	supercontinuum generation
SPM	self-phase modulation
SSFS	soliton self-frequency shift
TOD	third-order dispersion
X-FROG	cross-correlation frequency-resolved optical gating
XPM	cross-phase modulation
ZDW	zero-dispersion wavelength

Abstracts of publications

Only the abstracts of the journal publications within the scope of this thesis is given here. The complete list of publications published during the Ph. D. project can be seen on p. xv.

[1] M. H. Frosz, P. Falk, and O. Bang, "The role of the second zero-dispersion wavelength in generation of supercontinua and bright-bright soliton-pairs across the zero-dispersion wavelength," Opt. Express **13**(16), 6181–6192 (2005).

Supercontinuum generation with femtosecond pulses in photonic crystal fibers with two zero-dispersion wavelengths (ZDWs) is investigated numerically. The role of the higher ZDW is examined for 5 fiber designs with a nearly constant lower ZDW. It is found that the resulting spectrum is mainly determined by self-phase modulation in the first few mm of fiber, followed by soliton self-frequency shift and amplification of dispersive waves. It is demonstrated how femtosecond soliton pulses can be generated with any desired center wavelength in the 1020–1200 nm range by adjusting the fiber length. Further, the generation of a bright-bright soliton-pair from an initial single red-shifted soliton is found. The soliton-pair has one color in the anomalous dispersion region and the other color in the normal dispersion region, which has not previously been described for bright-bright soliton-pairs.

[2] P. Falk, M. H. Frosz, and O. Bang, "Supercontinuum generation in a photonic crystal fiber with two zero-dispersion wavelengths tapered to normal dispersion at all wavelengths," Opt. Express **13**(19), 7535–7540 (2005).

We numerically study supercontinuum generation in photonic crystal fibers with two zero-dispersion wavelengths, weakly tapered to have normal dispersion at all wavelengths after a certain distance. We pump with 15 fs pulses with milliwatt average power and show that two distinct smooth spectral parts are generated, with improved stability due to the normal dispersion. We characterize the two spectral parts and show how the 3 dB bandwidth, the center wavelength, and the power of the two parts depend on the taper parameters and the pump power.

[3] M. H. Frosz, T. Sørensen, and O. Bang, "Nanoengineering of photonic crystal fibers for supercontinuum spectral shaping," J. Opt. Soc. Am. B **23**(8), 1692–1699 (2006).

Supercontinuum generation using picosecond pulses pumped into cobweb photonic crystal fibers is investigated. Dispersion profiles are calculated for several fiber designs and used to analytically investigate the influence of the fiber structural parameters (core size and wall thickness) on the location of the Stokes and anti-Stokes bands and gain bandwidth. An analysis shows that the Raman effect is responsible for reducing the four-wave mixing gain and a slight reduction in the corresponding frequency shift from the pump, when the frequency shift is much larger than the Raman shift. Using numerical simulations we find that four-wave mixing is the dominant physical mechanism for the pumping scheme considered, and that there is a trade-off between the spectral width and the spectral flatness of the supercontinuum. The balance of this trade-off is determined by nanometer-scale design of the fiber structural parameters. It is also shown that the relatively high loss of the nonlinear fiber does not significantly affect the supercontinuum generation.

[4] M. H. Frosz, O. Bang, and A. Bjarklev, "Soliton collision and Raman gain regimes in continuous-wave pumped supercontinuum generation," Opt. Express **14**(20), 9391–9407 (2006).

We numerically investigate supercontinuum generation using continuous-wave pumping. It is found that energy transfer during collision of solitons plays an important role. The relative influence of

Raman gain on spectral broadening is shown to depend on the width of the calculation time window. Our results indicate that increasing the spectral linewidth of the pump can decrease the supercontinuum spectral width. Using a fiber with smaller dispersion at the pump wavelength reduces the required fiber length by decreasing the temporal width of the solitons formed from modulation instability. This also reduces the sensitivity to the pump spectral linewidth.

Bibliography

[1] M. H. Frosz, P. Falk, and O. Bang, "The role of the second zero-dispersion wavelength in generation of supercontinua and bright-bright soliton-pairs across the zero-dispersion wavelength," Opt. Express **13**(16), 6181–6192 (2005). http://www.opticsexpress.org/abstract.cfm?URI=OPEX-13-16-6181.

[2] P. Falk, M. H. Frosz, and O. Bang, "Supercontinuum generation in a photonic crystal fiber with two zero-dispersion wavelengths tapered to normal dispersion at all wavelengths," Opt. Express **13**(19), 7535–7545 (2005). http://www.opticsexpress.org/abstract.cfm?URI=OPEX-13-19-7535.

[3] M. H. Frosz, T. Sørensen, and O. Bang, "Nanoengineering of photonic crystal fibers for supercontinuum spectral shaping," J. Opt. Soc. Am. B **23**(8), 1692–1699 (2006). http://www.opticsinfobase.org/abstract.cfm?URI=josab-23-8-1692.

[4] M. H. Frosz, O. Bang, and A. Bjarklev, "Soliton collision and Raman gain regimes in continuous-wave pumped supercontinuum generation," Opt. Express **14**(20), 9391–9407 (2006). http://www.opticsinfobase.org/abstract.cfm?URI=oe-14-20-9391.

[5] P. Falk, M. H. Frosz, O. Bang, P. E. Andersen, A. Bjarklev, and L. Thrane, "Supercontinuum generation in a photonic crystal fiber tapered to normal dispersion for all wavelengths," in *17^{th} International Conference on Optical Fibre Sensors, OFS-17*, pp. 318–321 (Proceedings of SPIE, Vol. 5855, Bruges, Belgium, 2005). http://dx.doi.org/10.1117/12.623423.

[6] P. Falk, M. H. Frosz, and O. Bang, "The role of tapering and second zero dispersion wavelength for supercontinuum generation in Photonic Crystal Fibers," Annual meeting of the Danish Optical Society (DOPS), poster presentation, 17$^{\text{th}}$-18$^{\text{th}}$ November, Risø National Laboratory, Denmark (2005).

[7] M. H. Frosz, T. Sørensen, and O. Bang, "Nano-engineering of photonic crystal fibers for supercontinuum generation," in *Photonic Crystals and Fibers*, pp. 1–8 (Proceedings of SPIE, Vol. 5950, SPIE-COO, Warsaw, Poland, 2005). http://dx.doi.org/10.1117/12.621796.

[8] M. H. Frosz, O. Bang, A. Bjarklev, P. E. Andersen, and J. Broeng, "Supercontinuum generation in photonic crystal fibers: The role of the second zero dispersion wavelength," in *Conference on Lasers and Electro-Optics*, pp. 1255–1257 (CLEO, Vol. 2, Baltimore, MD, USA, 2005).

[9] M. H. Frosz, P. Falk, L. T. Pedersen, O. Bang, and A. Bjarklev, "Supercontinuum generation in untapered and tapered photonic crystal fibers with two zero dispersion wavelengths," in *Photonic Crystal Materials and Devices III*, pp. 190–197 (Proceedings of SPIE, Vol. 5733, Photonics West, San Jose, CA, USA, 2005). http://dx.doi.org/10.1117/12.601185.

[10] R. R. Alfano and S. L. Shapiro, "Emission in the region 4000 to 7000 Å via four-photon coupling in glass," Phys. Rev. Lett. **24**(11), 584–587 (1970). http://dx.doi.org/10.1103/PhysRevLett.24.584.

[11] R. R. Alfano and S. L. Shapiro, "Observation of self-phase modulation and small-scale filaments in crystals and glasses," Phys. Rev. Lett. **24**(11), 592–594 (1970). http://dx.doi.org/10.1103/PhysRevLett.24.592.

[12] R. R. Alfano, ed., *The Supercontinuum Laser Source: Fundamentals With Updated References*, 2nd ed. (Springer-Verlag, New York, 2005). ISBN 0-387-24504-9.

[13] G. P. Agrawal, *Nonlinear Fiber Optics*, 3rd ed. (Academic Press, San Diego, CA, USA, 2001).

[14] C. Lin and R. H. Stolen, "New nanosecond continuum for excited-state spectroscopy," Appl. Phys. Lett. **28**(4), 216–218 (1976). http://dx.doi.org/10.1063/1.88702.

[15] F. L. Pedrotti and L. S. Pedrotti, *Introduction to Optics*, 2nd ed. (Prentice Hall, 1993). ISBN 0-13-501545-6.

[16] J. C. Knight, J. Broeng, T. A. Birks, and P. S. Russell, "Photonic Band Gap Guidance in Optical Fibers," Science **282**(5393), 1476–1478 (1998). http://dx.doi.org/10.1126/science.282.5393.1476.

[17] A. Bjarklev, J. Broeng, and A. S. Bjarklev, *Photonic crystal fibres* (Kluwer Academic Publishers, Boston, MA, 2003). ISBN: 140207610X.

[18] F. Benabid, J. C. Knight, G. Antonopoulos, and P. S. Russell, "Stimulated Raman scattering in hydrogen-filled hollow-core photonic crystal fiber," Science **298**(5592), 399–402 (2002). http://dx.doi.org/10.1126/science.1076408.

[19] K. P. Hansen, "Introduction to nonlinear photonic crystal fibers," J. Opt. Fiber Commun. Rep. **2**(3), 226–254 (2005). http://dx.doi.org/10.1007/s10297-004-0021-1.

[20] J. M. Dudley, L. Provino, N. Grossard, H. Maillotte, R. S. Windeler, B. J. Eggleton, and S. Coen, "Supercontinuum generation in air-silica microstructured fibers with nanosecond and femtosecond pulse pumping," J. Opt. Soc. Am. B **19**(4), 765–771 (2002).

[21] N. I. Nikolov, T. Sørensen, O. Bang, and A. Bjarklev, "Improving efficiency of supercontinuum generation in photonic crystal fibers by direct degenerate four-wave mixing," J. Opt. Soc. Am. B **20**(11), 2329–2337 (2003).

[22] K. Mori, T. Morioka, and M. Saruwatari, "Ultrawide spectral range group-velocity dispersion measurement utilizing supercontinuum in an optical fiber pumped by a 1.5 μm compact laser source," IEEE Trans. Instrum. Meas. **44**(3), 712–715 (1995). http://dx.doi.org/10.1109/19.387315.

[23] T. Morioka, K. Uchiyama, S. Kawanishi, S. Suzuki, and M. Saruwatari, "Multiwavelength picosecond pulse source with low jitter and high optical frequency stability based on 200 nm supercontinuum filtering," Electron. Lett. **31**(13), 1064–1066 (1995).

[24] A. Freiberg, J. A. Jackson, S. Lin, and N. W. Woodbury, "Subpicosecond pump-supercontinuum probe spectroscopy of LH2 photosynthetic antenna," J. Phys. Chem. A **102**(23), 4372–4380 (1998).

[25] P. V. Kelkar, F. Coppinger, A. S. Bhusan, and B. Jalali, "Time-domain optical sensing," Electron. Lett. **35**(19), 1661–1662 (1999).

[26] D. J. Jones, S. A. Diddams, J. K. Ranka, A. Stentz, R. S. Windeler, J. L. Hall, and S. T. Cundiff, "Carrier-envelope phase control of femtosecond mode-locked laser and direct optical frequency synthesis," Science **288**(5466), 635–639 (2000). http://dx.doi.org/10.1126/science.288.5466.635.

[27] I. Hartl, X. D. Li, C. Chudoba, R. K. Ghanta, T. H. Ko, J. G. Fujimoto, J. K. Ranka, and R. S. Windeler, "Ultrahigh-resolution optical coherence tomography using continuum generation in an air-silica microstructure optical fiber," Opt. Lett. **26**(9), 608–610 (2001).

[28] D. Huang, E. A. Swanson, C. P. Lin, J. S. Schuman, W. G. Stinson, W. Chang, M. R. Hee, T. Flotte, K. Gregory, C. A. Puliafito, and J. G. Fujumoto, "Optical coherence tomography," Science **254**(5035), 1178–1181 (1991). http://dx.doi.org/10.1126/science.1957169.

[29] E. A. Swanson, D. Huang, M. R. Hee, J. G. Fujimoto, C. P. Lin, and C. A. Puliafito, "High-speed optical coherence domain reflectometry," Opt. Lett. **17**(2), 151–153 (1992). http://www.opticsinfobase.org/abstract.cfm?URI=ol-17-2-151.

[30] A. F. Fercher, W. Drexler, C. K. Hitzenberger, and T. Lasser, "Optical coherence tomography - principles and applications," Reports on Progress in Physics **66**(2), 239–303 (2003). http://stacks.iop.org/0034-4885/66/239.

[31] B. E. Bouma and G. J. Tearney, eds., *Handbook of Optical Coherence Tomography* (Dekker, 2001). ISBN: 0824705580.

[32] Y. Wang, J. S. Nelson, Z. Chen, B. J. Reiser, R. S. Chuck, and R. S. Windeler, "Optimal wavelength for ultrahigh-resolution optical coherence tomography," Opt. Express **11**(12), 1411–1417 (2003). http://www.opticsinfobase.org/abstract.cfm?URI=oe-11-12-1411.

[33] K. J. Blow and D. Wood, "Theoretical description of transient stimulated Raman scattering in optical fibers," IEEE J. Quantum Electron. **25**, 2665–2673 (1989).

[34] P. V. Mamyshev and S. V. Chernikov, "Ultrashort-pulse propagation in optical fibers," Opt. Lett. **15**(19), 1076–1078 (1990).

[35] P. L. François, "Nonlinear propagation of ultrashort pulses in optical fibers: total field formulation in the frequency domain," J. Opt. Soc. Am. B **8**(2), 276–293 (1991). http://www.opticsinfobase.org/abstract.cfm?URI=josab-8-2-276.

[36] J. Lægsgaard, N. A. Mortensen, and A. Bjarklev, "Mode areas and field-energy distribution in honeycomb photonic bandgap fibers," J. Opt. Soc. Am. B **20**(10), 2037–2045 (2003).

[37] R. W. Hellwarth, "Third-order optical susceptibilities of liquids and solids," Prog. Quantum Electron. **5**(1), 2–68 (1977).

[38] P. T. Dinda, G. Millot, and S. Wabnitz, "Polarization switching and suppresion of stimulated Raman scattering in birefringent optical fibers," J. Opt. Soc. Am. B **15**(5), 1433–1441 (1998). http://www.opticsinfobase.org/abstract.cfm?URI=josab-15-5-1433.

[39] N. I. Nikolov, "Distributed nonlinear optical response," Ph.D. thesis, Informatics and Mathematical Modelling, Technical University of Denmark, DTU, Richard Petersens Plads, Building 321, DK-2800 Kgs. Lyngby (2005). Supervised by Prof. Peter Leth Christiansen. http://www2.imm.dtu.dk/pubdb/p.php?3147.

[40] F. Biancalana, D. V. Skryabin, and P. St. J. Russell, "Four-wave mixing instabilities in photonic-crystal and tapered fibers," Phys. Rev. E **68**, 046603 (2003). http://dx.doi.org/10.1103/PhysRevE.68.046603.

[41] V. E. Zakharov and A. B. Shabat, "Exact theory of 2-dimensional self-focusing and one-dimenstional self-modulation of waves in nonlinear media," Sov. Phys. JETP **34**(1), 62 (1972).

[42] W. Shuang-Chun, S. Wen-Hua, Z. Hua, F. Xi-Quan, Q. Lie-Jia, and F. Dian-Yuan, "Influence of Higher-Order Dispersions and Raman Delayed Response on Modulation Instability in Microstructured Fibres," Chinese Phys. Lett. **20**(6), 852–854 (2003). http://dx.doi.org/10.1088/0256-307X/20/6/321.

[43] E. A. Golovchenko and A. N. Pilipetskii, "Unified analysis of four-photon mixing, modulational instability, and stimulated Raman scattering under varioius polarization conditions in fibers," J. Opt. Soc. Am. B **11**(1), 92–101 (1994).

[44] S. Coen, D. A. Wardle, and J. D. Harvey, "Observation of Non-Phase-Matched Parametric Amplification in Resonant Nonlinear Optics," Phys. Rev. Lett. **89**, 273901/1–4 (2002). http://dx.doi.org/10.1103/PhysRevLett.89.273901.

[45] F. Vanholsbeeck, P. Emplit, and S. Coen, "Complete experimental characterization of the influence of parametric four-wave mixing on stimulated Raman gain," Opt. Lett. **28**(20), 1960–1962 (2003). http://www.opticsinfobase.org/abstract.cfm?URI=ol-28-20-1960.

[46] A. V. Yulin, D. V. Skryabin, and P. St. J. Russell, "Four-wave mixing of linear waves and solitons in fibers with higher-order dispersion," Opt. Lett. **29**(20), 2411–2413 (2004). http://www.opticsinfobase.org/abstract.cfm?URI=ol-29-20-2411.

[47] F. M. Mitschke and L. F. Mollenauer, "Discovery of the soliton self-frequency shift," Opt. Lett. **11**(10), 659–661 (1986).

[48] J. P. Gordon, "Theory of the soliton self-frequency shift," Opt. Lett. **11**(10), 662–664 (1986).

[49] J. Herrmann and A. Nazarkin, "Soliton self-frequency shift for pulses with a duration less than the period of molecular oscillations," Opt. Lett. **19**(24), 2065–2067 (1994).

[50] N. Akhmediev and M. Karlsson, "Cherenkov radiation emitted by solitons in optical fibers," Phys. Rev. A **51**(3), 2602–2607 (1995).

[51] A. Efimov, A. J. Taylor, F. G. Omenetto, A. V. Yulin, N. Y. Joly, F. Biancalana, D. V. Skryabin, J. C. Knight, and P. S. J. Russell, "Time-spectrally-resolved ultrafast nonlinear dynamics in small-core photonic crystal fibers: Experiment and modelling," Opt. Express **12**(26), 6498–6507 (2004). http://www.opticsinfobase.org/abstract.cfm?URI=oe-12-26-6498.

[52] G. P. Agrawal, *Fiber-Optic Communication Systems*, 2nd ed. (John Wiley & Sons, Inc., New York, NY, 1997).

[53] P. Petropoulos, T. M. Monro, W. Belardi, K. Furusawa, J. H. Lee, and D. J. Richardson, "2R-regenerative all-optical switch based on a highly nonlinear holey fiber," Opt. Lett. **26**(16), 1233–1235 (2001).

[54] T. A. Birks, W. J. Wadsworth, and P. St. J. Russell, "Supercontinuum generation in tapered fibers," Opt. Lett. **25**(19), 1415–1417 (2000).

[55] A. Apolonski, B. Povazay, A. Unterhuber, W. Drexler, W. J. Wadsworth, J. C. Knight, and P. St. J. Russell, "Spectral shaping of supercontinuum in a cobweb photonic-crystal fiber with sub-20-fs pulses," J. Opt. Soc. Am. B **19**(9), 2165–2170 (2002).

[56] G. Genty, M. Lehtonen, H. Ludvigsen, and M. Kaivola, "Enhanced bandwidth of supercontinuum generated in microstructured fibers," Opt. Express **12**(15), 3471–3480 (2004). http://www.opticsexpress.org/abstract.cfm?URI=OPEX-12-15-3471.

[57] http://www.crystal-fibre.com/products/nonlinear.shtm (2006).

[58] S. G. Johnson and J. D. Joannopoulos, "Block-Iterative Frequency-Domain Methods for Maxwell's Equations in a Planewave Basis," Opt. Express **8**(3), 173–190 (2001). http://www.opticsexpress.org/abstract.cfm?URI=OPEX-8-3-173.

[59] J. Riishede, "Modelling Photonic Crystal Fibres with the Finite Difference Method," Ph.D. thesis, Research Center COM, Technical University of Denmark, Building 345V, DK-2800 Kgs. Lyngby (2005).

[60] C. A. De Francisco, B. V. Borges, and M. A. Romero, "A semivectorial method for the modeling of photonic crystal fibers," Microwave Opt. Technol. Lett. **38**(5), 418–421 (2003). http://dx.doi.org/10.1002/mop.11078.

[61] S. Coen, A. H. L. Chau, R. Leonhardt, J. D. Harvey, J. C. Knight, W. J. Wadsworth, and P. St. J. Russell, "Supercontinuum generation by stimulated Raman scattering and parametric four-wave mixing in photonic crystal fibers," J. Opt. Soc. Am. B **19**(4), 753–764 (2002).

[62] A. Hasegawa and F. Tappert, "Transmission of stationary nonlinear optical pulses in dispersive dielectric fibers. I. Anomalous dispersion," Appl. Phys. Lett. **23**(3), 142–144 (1973). http://dx.doi.org/10.1063/1.1654836.

[63] J. A. Fleck, Jr., J. R. Morris, and M. D. Feit, "Time-Dependent Propagation of High Energy Laser Beams through the Atmosphere," Appl. Phys. **10**(2), 129–160 (1976). http://dx.doi.org/10.1007/BF00896333.

[64] O. V. Sinkin, R. Holzlöhner, J. Zweck, and C. R. Menyuk, "Optimization of the Split-Step Fourier Method in Modeling Optical-Fiber Communications Systems," J. Lightwave Technol. **21**(1), 61–68 (2003). http://dx.doi.org/10.1109/JLT.2003.808628.

[65] W. H. Press, S. A. Teukolsky, W. T. Vetterling, and B. P. Flannery, *Numerical Recipes in C++: The Art of Scientific Computing*, 2nd ed. (Cambridge University Press, Cambridge, 2002). http://www.nr.com.

[66] M. Frigo and S. G. Johnson, "The Design and Implementation of FFTW3," Proceedings of the IEEE **93**(2), 216–231 (2005). Invited paper, Special Issue on Program Generation, Optimization, and Platform Adaptation. Preprint: http://www.fftw.org/fftw-paper-ieee.pdf. Official issue: http://dx.doi.org/10.1109/JPROC.2004.840301.

[67] http://www.fftw.org (2006).

[68] http://mary.risoe.dk, accessible via Risø intranet (2006).

[69] http://www.gbar.dtu.dk (2006).

[70] P. D. Rasmussen, COM•DTU, Technical University of Denmark, Personal communication (2006).

[71] U. Keller, "Recent developments in compact ultrafast lasers," Nature **424**(6950), 831–838 (2003). http://dx.doi.org/10.1038/nature01938.

[72] J. K. Ranka, R. S. Windeler, and A. J. Stentz, "Visible continuum generation in air-silica microstructure optical fibers with anomalous dispersion at 800 nm," Opt. Lett. **25**(1), 25–27 (2000).

[73] K. M. Hilligsøe, T. V. Andersen, H. N. Paulsen, C. K. Nielsen, K. Mølmer, S. Keiding, R. Kristiansen, K. P. Hansen, and J. J. Larsen, "Supercontinuum generation in a photonic crystal fiber with two zero dispersion wavelengths," Opt. Express **12**(6), 1045–1054 (2004). http://www.opticsexpress.org/abstract.cfm?URI=OPEX-12-6-1045.

[74] A. Aguirre, N. Nisizawa, J. Fujimoto, W. Seitz, M. Lederer, and D. Kopf, "Continuum generation in a novel photonic crystal fiber for ultrahigh resolution optical coherence tomography at 800 nm and 1300 nm," Opt. Express **14**(3), 1145–1160 (2006). http://www.opticsinfobase.org/abstract.cfm?URI=oe-14-3-1145.

[75] M. L. V. Tse, P. Horak, F. Poletti, N. G. Broderick, J. H. Price, J. R. Hayes, and D. J. Richardson, "Supercontinuum generation at 1.06 μm in holey fibers with dispersion flattened profiles," Opt. Express **14**(10), 4445–4451 (2006). http://www.opticsinfobase.org/abstract.cfm?URI=oe-14-10-4445.

[76] T. V. Andersen, K. M. Hilligsøe, C. K. Nielsen, J. Thøgersen, K. P. Hansen, S. R. Keiding, and J. J. Larsen, "Continuous-wave wavelength conversion in a photonic crystal fiber with two zero-dispersion wavelengths," Opt. Express **12**(17), 4113–4122 (2004). http://www.opticsinfobase.org/abstract.cfm?URI=oe-12-17-4113.

[77] E. B. Treacy, "Measurement and Interpretation of Dynamic Spectrograms of Picosecond Light Pulses," J. Appl. Phys. **42**(10), 3848–3858 (1971). http://dx.doi.org/10.1063/1.1659696.

[78] A. Efimov and A. J. Taylor, "Spectral-temporal dynamics of ultrashort Raman solitons and their role in third-harmonic generation in photonic crystal fibers," Appl. Phys. B **80**(6), 721–725 (2005). http://dx.doi.org/10.1007/s00340-005-1789-2.

[79] Y. Kodama and A. Hasegawa, "Nonlinear pulse propagation in a monomode dielectric guide," IEEE J. Quantum Electron. **QE-23**(5), 510–524 (1987).

[80] J. K. Lucek and K. J. Blow, "Soliton self-frequency shift in telecommunications fiber," Phys. Rev. A **45**(9), 6666–6674 (1992). http://dx.doi.org/10.1103/PhysRevA.45.6666.

[81] G. Genty, M. Lehtonen, and H. Ludvigsen, "Effect of cross-phase modulation on supercontinuum generated in microstructured fibers with sub-30 fs pulses," Opt. Express **12**(19), 4614–4624 (2004). http://www.opticsexpress.org/abstract.cfm?URI=OPEX-12-19-4614.

[82] X. Liu, C. Xu, W. H. Knox, J. K. Chandalia, B. J. Eggleton, S. G. Kosinski, and R. S. Windeler, "Soliton self-frequency shift in a short tapered air-silica microstructure fiber," Opt. Lett. **26**(6), 358–360 (2001).

[83] D. T. Reid, I. G. Cormack, W. J. Wadsworth, J. C. Knight, and P. S. Russell, "Soliton self-frequency shift effects in photonic crystal fibre," J. Mod. Opt. **49**(5–6), 757–767 (2002). http://dx.doi.org/10.1080/09500340110099171.

[84] E. R. Andresen, V. Birkedal, J. Thøgersen, and S. R. Keiding, "Tunable light source for coherent anti-Stokes Raman scattering microspectroscopy based on the soliton self-frequency shift," Opt. Lett. **31**(9), 1328–1330 (2006). http://www.opticsinfobase.org/abstract.cfm?URI=ol-31-9-1328.

[85] C. S. Aparna, S. Kumar, and A. Selvarajan, "Suppression of the soliton frequency shifts by nonlinear pairing of pulses," Opt. Commun. **131**(4–6), 267–273 (1996). http://dx.doi.org/10.1016/0030-4018(96)00350-1.

[86] V. V. Afanasyev, Y. S. Kivshar, V. V. Konotop, and V. N. Serkin, "Dynamics of coupled dark and bright optical solitons," Opt. Lett. **14**(15), 805–807 (1989). http://www.opticsinfobase.org/abstract.cfm?URI=ol-14-15-805.

[87] F. K. Abdullaev, S. A. Darmanyan, S. Bischoff, P. L. Christiansen, and M. P. Sørensen, "Modulational instability in optical fibers near the zero dispersion point," Opt. Commun. **108**(1–3), 60–64 (1994). http://dx.doi.org/10.1016/0030-4018(94)90216-X.

[88] J. D. Harvey, R. Leonhardt, S. Coen, G. K. L. Wong, J. C. Knight, W. J. Wadsworth, and P. S. Russell, "Scalar modulation instability in the normal dispersion regime by use of a photonic crystal fiber," Opt. Lett. **28**(22), 2225–2227 (2003).

[89] D. V. Skryabin, F. Luan, J. C. Knight, and P. S. J. Russell, "Soliton self-frequency shift cancellation in photonic crystal fibers," Science **301**, 1705–1708 (2003).

[90] F. Biancalana, D. V. Skryabin, and A. V. Yulin, "Theory of the soliton self-frequency shift compensation by the resonant radiation in photonic crystal fibers," Phys. Rev. E **70**, 016615 (2004). http://dx.doi.org/10.1103/PhysRevE.70.016615.

[91] O. Bang and W. Królikowski, Personal communication (2006).

[92] K. P. Hansen, Crystal Fibre A/S, Personal communication.

[93] F. Lu, Y. Deng, and W. H. Knox, "Generation of broadband femtosecond visible pulses in dispersion-micromanaged holey fibers," Opt. Lett. **30**(12), 1566–1568 (2005). http://www.opticsinfobase.org/abstract.cfm?URI=ol-30-12-1566.

[94] H. C. Nguyen, B. T. Kuhlmey, E. C. Mägi, M. J. Steel, P. Domachuk, C. L. Smith, and B. J. Eggleton, "Tapered photonic crystal fibres: properties, characterisation and applications," Appl. Phys. B **81**(2–3), 377–387 (2005). http://dx.doi.org/10.1007/s00340-005-1901-7.

[95] S. G. Leon-Saval, T. A. Birks, W. J. Wadsworth, P. St. J. Russell, and M. W. Mason, "Supercontinuum generation in submicron fibre waveguides," Opt. Express **12**(13), 2864–2869 (2004). http://www.opticsinfobase.org/abstract.cfm?URI=oe-12-13-2864 .

[96] T. A. Birks and Y. W. Li, "The Shape of Fiber Tapers," J. Lightwave Technol. **10**(4), 432–438 (1992). http://dx.doi.org/10.1109/50.134196.

[97] S. V. Chernikov and P. V. Mamyshev, "Femtosecond soliton propagation in fibers with slowly decreasing dispersion," J. Opt. Soc. Am. B **8**(8), 1633–1641 (1991). http://www.opticsinfobase.org/abstract.cfm?URI=josab-8-8-1633.

[98] J. M. Schmitt, S. H. Xiang, and K. M. Yung, "Differential absorption imaging with optical coherence tomography," J. Opt. Soc. Am. A **15**(9), 2288–2296 (1998).

[99] J. E. Sharping, M. Fiorentino, A. Coker, P. Kumar, and R. S. Windeler, "Four-wave mixing in microstructure fiber," Opt. Lett. **26**(14), 1048–1050 (2001).

[100] W. J. Wadsworth, N. Joly, J. C. Knight, T. A. Birks, F. Biancalana, and P. St. J. Russell, "Supercontinuum and four-wave mixing with Q-switched pulses in endlessly single-mode photonic crystal fibres," Opt. Express **12**(2), 299–309 (2004). http://www.opticsinfobase.org/abstract.cfm?URI=oe-12-2-299.

[101] K. P. Hansen, J. R. Jensen, C. Jacobsen, H. R. Simonsen, J. Broeng, P. M. W. Skovgaard, A. Petersson, and A. Bjarklev, "Highly nonlinear photonic crystal fiber with zero-dispersion at 1.55 μm," in *Optical Fiber Communication Conference*, pp. FA91–FA93 (Optical Society of America, 2002).

[102] P. L. Baldeck and R. R. Alfano, "Intensity effects on the stimulated four photon spectra generated by picosecond pulses in optical fibers," IEEE J. Lightwave Technol. **5**(12), 1712–1715 (1987).

[103] K. P. Hansen, Crystal Fibre A/S, Personal communication (February 2006).

[104] M. Prabhu, N. S. Kim, and K. Ueda, "Ultra-Broadband CW Supercontinuum Generation Centered at 1483.4 nm from Brillouin/Raman Fiber Laser," Jpn. J. Appl. Phys. **39**, L291–L293 (2000). http://dx.doi.org/10.1143/JJAP.39.L291.

[105] J. W. Nicholson, A. K. Abeeluck, C. Headley, M. F. Yan, and C. G. Jørgensen, "Pulsed and continuous-wave supercontinuum generation in highly nonlinear, dispersion-shifted fibers," Appl. Phys. B **77**, 211–218 (2003). http://dx.doi.org/10.1007/s00340-003-1201-z.

[106] A. V. Avdokhin, S. V. Popov, and J. R. Taylor, "Continuous-wave, high-power, Raman continuum generation in holey fibers," Opt. Lett. **28**(15), 1353–1355 (2003).

[107] P.-L. Hsiung, Y. Chen, T. Ko, J. G. Fujimoto, C. J. S. de Matos, S. V. Popov, J. R. Taylor, and V. P. Gapontsev, "Optical coherence tomography using a continuous-wave, high-power, Raman continuum light source," Opt. Express **12**(22), 5287–5295 (2004). http://www.opticsinfobase.org/abstract.cfm?URI=oe-12-22-5287.

[108] C. J. S. de Matos, S. V. Popov, and J. R. Taylor, "Temporal and noise characteristics of continuous-wave-pumped continuum generation in holey fibers around 1300 nm," Appl. Phys. Lett. **85**(14), 2706–2708 (2004).

[109] J. H. Lee, Y.-G. Han, and S. B. Lee, "Experimental study on seed light source coherence dependence of continuous-wave supercontinuum performance," Opt. Express **14**(8), 3443–3452 (2006). http://www.opticsinfobase.org/abstract.cfm?URI=oe-14-8-3443.

[110] A. Mussot, E. Lantz, H. Maillotte, T. Sylvestre, C. Finot, and S. Pitois, "Spectral broadening of a partially coherent CW laser beam in single-mode optical fibers," Opt. Express **12**(13), 2838–2843 (2004). http://www.opticsexpress.org/abstract.cfm?URI=OPEX-12-13-2838.

[111] S. M. Kobtsev and S. V. Smirnov, "Modelling of high-power supercontinuum generation in highly nonlinear, dispersion shifted fibers at CW pump," Opt. Express **13**(18), 6912–6918 (2005). http://www.opticsexpress.org/abstract.cfm?URI=OPEX-13-18-6912.

[112] F. Vanholsbeeck, S. Martin-Lopez, M. González-Herráez, and S. Coen, "The role of pump incoherence in continuous-wave supercontinuum generation," Opt. Express **13**(17), 6615–6623 (2005). http://www.opticsexpress.org/abstract.cfm?URI=OPEX-13-17-6615.

[113] A. K. Abeeluck and C. Headley, "Continuous-wave pumping in the anomalous- and normal-dispersion regimes of nonlinear fibers for supercontinuum generation," Opt. Lett. **30**(1), 61–63 (2005).

[114] B. Barviau, S. Randoux, and P. Suret, "Spectral broadening of a multimode continous-wave optical field propagating in the normal dispersion regime of a fiber," Opt. Lett. **31**(11), 1696–1698 (2006).

[115] M. N. Islam, G. Sucha, I. Bar-Joseph, M. Wegener, J. P. Gordon, and D. S. Chemla, "Femtosecond distributed soliton spectrum in fibers," J. Opt. Soc. Am. B **6**(6), 1149–1158 (1989). http://www.opticsinfobase.org/abstract.cfm?URI=josab-6-6-1149.

[116] R. G. Smith, "Optical power handling capacity of low loss optical fibers as determined by stimulated Raman and Brillouin scattering," Appl. Opt. **11**(11), 2489–2494 (1972).

[117] S. B. Cavalcanti, G. P. Agrawal, and M. Yu, "Noise amplification in dispersive nonlinear media," Phys. Rev. A **51**(5), 4086–4092 (1995). http://dx.doi.org/10.1103/PhysRevA.51.4086.

[118] J. W. Goodman, *Statistical Optics* (John Wiley & Sons Inc., 2000). ISBN 0471399167.

[119] W. K. Marshall, B. Crosignani, and A. Yariv, "Laser phase noise to intensity noise conversion by lowest-order group-velocity dispersion in optical fiber:exact theory," Opt. Lett. **25**(3), 165–167 (2000). http://www.opticsinfobase.org/abstract.cfm?URI=ol-25-3-165.

[120] H. A. Haus and W. S. Wong, "Solitons in optical communications," Rev. Mod. Phys. **68**(2), 423–444 (1996). http://link.aps.org/abstract/RMP/v68/p423.

[121] A. Peleg, M. Chertkov, and I. Gabitov, "Interchannel interaction of optical solitons," Phys. Rev. E **68**, 026605 (2003). http://link.aps.org/abstract/PRE/v68/e026605.

[122] S. Chi and S. Wen, "Raman cross talk of soliton collision in a lossless fiber," Opt. Lett. **14**(21), 1216–1218 (1989).

[123] B. A. Malomed, "Soliton-collision problem in the nonlinear Schrödinger equation with a nonlinear damping term," Phys. Rev. A **44**(2), 1412–1414 (1991). http://link.aps.org/abstract/PRA/v44/p1412.

[124] Y. Chung and A. Peleg, "Strongly non-Gaussian statistics of optical soliton parameters due to collisions in the presence of delayed Raman response," Nonlinearity **18**(4), 1555–1574 (2005). http://stacks.iop.org/Non/18/1555.

[125] O. Bang and M. Peyrard, "Generation of high-energy localized vibrational modes in nonlinear Klein-Gordon lattices," Phys. Rev. E **53**(4), 4143–4152 (1996). http://link.aps.org/abstract/PRE/v53/p4143.

[126] Y. Kodama and K. Nozaki, "Soliton interaction in optical fibers," Opt. Lett. **12**(12), 1038–1040 (1987).

[127] N. Nishizawa, Y. Chen, P. Hsiung, E. P. Ippen, and J. G. Fujimoto, "Real-time, ultrahigh-resolution, optical coherence tomography with an all-fiber, femtosecond fiber laser continuum at 1.5 μm," Opt. Lett. **29**(24), 2846–2848 (2004). http://www.opticsinfobase.org.globalproxy.cvt.dk/abstract.cfm?URI=ol-29-24-2846.

[128] Y. Jiang, X. Chen, B. Howley, M. Y. Chen, and R. T. Chen, "Effects of temperature fluctuation on highly dispersive photonic crystal fibers," Appl. Phys. Lett. **88**(1), 011108 (p. 1–3) (2006). http://dx.doi.org/10.1063/1.2162684.

[129] R. Zhang, J. Teipel, and H. Giessen, "Theoretical design of a liquid-core photonic crystal fiber for supercontinuum generation," Opt. Express **14**(15), 6800–6812 (2006). http://oe.osa.org/abstract.cfm?id=92249.

[130] T. T. Larsen, A. Bjarklev, D. S. Hermann, and J. Broeng, "Optical devices based on liquid crystal photonic bandgap fibres," Opt. Express **11**(20), 2589–2596 (2003). http://www.opticsinfobase.org/abstract.cfm?URI=oe-11-20-2589.

[131] P. D. Rasmussen, J. Lægsgaard, and O. Bang, "Chromatic dispersion of liquid-crystal infiltrated capillary tubes and photonic crystal fibers," J. Opt. Soc. Am. B **23**(10), 2241–2248 (2006). http://www.opticsinfobase.org/abstract.cfm?URI=josab-23-10-2241.

[132] B. E. A. Saleh and M. C. Teich, *Fundamentals of Photonics* (John Wiley & Sons, Inc., New York, 1991). ISBN 0-471-83965-5.